Near-surface hydrodynamics and transport of polymeric and colloidal soft matter

Joshua D Mcgraw

▶ **To cite this version:**

Joshua D Mcgraw. Near-surface hydrodynamics and transport of polymeric and colloidal soft matter. Soft Condensed Matter [cond-mat.soft]. Université PSL (Paris Sciences & Lettres), 2023. ⟨tel-04314388⟩

HAL Id: tel-04314388

https://hal.science/tel-04314388v1

Submitted on 29 Nov 2023

HAL is a multi-disciplinary open access archive for the deposit and dissemination of scientific research documents, whether they are published or not. The documents may come from teaching and research institutions in France or abroad, or from public or private research centers.

L'archive ouverte pluridisciplinaire **HAL**, est destinée au dépôt et à la diffusion de documents scientifiques de niveau recherche, publiés ou non, émanant des établissements d'enseignement et de recherche français ou étrangers, des laboratoires publics ou privés.

HAL Authorization

PSL UNIVERSITÉ PARIS

HABILITATION À DIRIGER DES RECHERCHES

DE L'UNIVERSITÉ PSL

Présentée à ESPCI–PSL

Near-surface hydrodynamics and transport of polymeric and colloidal soft matter

Présentation des travaux par

Joshua D. McGraw

Le 26 octobre 2023

Discipline

Physique

Composition du jury :

Olivier BÉNICHOU Directeur de Recherche, Sorbonne Université	*Rapporteur*
Anne-Laure BIANCE Directrice de Recherche, Université de Lyon1	*Rapporteur*
Isabelle CANTAT Professeure, Université de Rennes	*Rapporteur*
Annie COLIN Professeure, PSL Research University	*Examinateur*
Alfred J. CROSBY Professor, UMASS–Amherst	*Examinateur*
Eric DUFRESNE Professor, Cornell University	*Examinateur*

ESPCI PARIS | PSL

Contents

List of Figures

Acknowledgements

I would like to take this initial opportunity to warmly thank the earliest readers of this document for their valuable time and expertise: the *rapporteurs* Anne-Laure Biance, Isabelle Cantat and Olivier Benichou; along with the *examinateurs* Al Crosby, Annie Colin and Eric Dufresne. On submission, I sincerely look forward to reading your comments on the manuscript and to discussing with you during and after the upcoming presentation.

It is perhaps true that my research could be described as a biased random walk, the gentle pull leaning towards interesting data, resulting in many fascinating discussions arising from the interrogation of this former data. In this naïve analogy, (i) bias and (ii) interrogation constitute two steps of a loop that has run since my introduction to research. At almost every step the loop is perturbed, and most often for the better, by benevolent agents that I have had a great honour and pleasure to work with. Indeed, research is a collective effort, with each member of a collaboration contributing their unique talents and perspectives to move the boundaries of established knowledge. In this context, I thank first and foremost the PhD and master students, interns and post-docs that have entered my loop, whom I have at least partially advised. I thank them for their efforts and ingenuity. I thank them for their big ideas, the precious and rare large deviations of our domain, and also the smaller ones. Their work was and continues to be done, often, in the face of what could seem uncrossable barriers, but which once surpassed leave us in highly excited states. I thank them for sending me plots; among the noise of daily mail, each new data point is a sincere delight. For the period during which this document is concerned, these people are: Matthias Lessel, Mischa Klos, Sabrina Haefner, Simon Maurer, Antoine Bridet, Jonas Heppe (Saarbrücken); Baptiste Lemaire, Mohammed Aly, Julien Laszlo, Gregoire Le Lay, Alexandre Vilquin, Abir Boudaoud, Gabriel Guyard, Guilhem Mariette, Caroline Kopecz-Muller, Aymène Sadaoui, Rachel Piednoir, Ana Mesic, Finn Box, Clémence Gaunand, Caroline Cramail, Gregoire Clément, Mathieu Oléron, Masoodah Gunny, Samuel Hidalgo-Caballero, Mahammad Alyiev, Manal El Manouzi, Clara Notebaert, Anne Le Floc'h (Paris). Conversely, those that guided my scientific investigations deserve a heartfelt thank you for their patient tutelage and letting me operate largely free of very strong bias: even though less in the scope of this document, I like to thank Kari Dalnoki-Veress (McMaster) who continues to be a great friend and mentor; Karin Jacobs (Saarland) who let me a great freedom and remains an inspiring advisor. After becoming a bit more scientifically independent, I was greatly supported by Lydéric Bocquet, Etienne Rolley, Werner Krauth, and Jean-Marc Berroir (ENS); thanks to Stephen Donaldson for the fun we had building a lab together. I am deeply indebted to Frédéric Restagno and to Elie Raphaël for their guidance and support, while and much more-so since, being recruited as *chargé de recherche*; a similar thanks goes to Patrick Tabeling. My scientific trajectory has been hugely influenced my friend and collaborator Thomas Salez. As of this writing, we have worked together for more than a decade and I am sincerely looking forward to the next one. Oliver Bäumchen is recognised and warmly regarded in a similar spirit. The years we spent, the three of us, forging our independent scientific careers together were very special. I am also very much looking forward to future works with FR, ER, AV, TS and Vincent Bertin, to contin-

uing parallel collaborative adventures with Matthieu Labousse, Yvette Tran, Marco Ribezzi, Kawthar Bouchemal, David Dean, with Marie Le Merrer and Catherine Barentin, along with Anke Lindner and the rest of team *sensorialité*. While perhaps for the moment *partie remise*, I acknowledge with fondness my collaborations with Tak-Shing Chan, Teresa Lopez-Leon, Florestan Ogheard, Stephane Jouenne, Alexis Chennevière, Antoine Nigues and Alessandro Siria, Guillaume Miquelard-Garnier and Cyrille Sollogoub, Kristina Davitt, Marie-Caroline Jullien and with Margaux Kerdraon. The engineers of the technology platform at IPGG deserve a great deal of thanks, their constant support and ingenuity are very much appreciated. I also warmly thank the extremely talented administrators at Gulliver for their tireless efforts on my behalf: Fée Sorrentino, Elisa Silveiro, Jeldy Cubas-Hernandes, and while perhaps straddling the boundary, it is also a great pleasure to thank Justine Laurent. You are the hidden variables, the hidden gems of experimental science. I would like lastly to acknowledge the many lecturers I have had the joy to teach with and learn from since my arrival in Paris. Particularly, these people are David Quéré, Lydéric Bocquet at the ENS ICFP; Patrick Perrin and Kawthar Bouchemal in the PSL SGM including also the tireless program managers Cécile Monteux, Domitille Guiaume, Cécilie Duhamel, Vincent Guipont and Lola Lilensten; Marie-Caroline Jullien, Nicolas Bremond and Olivia du Roure at the IPGG M2 along with Jacques Fattaccioli; finally at ESPCI Hélène Montes and Corinne Soulié-Ziakovic for having me in the polymer tutorats and of course it is a great pleasure to help in the hydrodynamics lab with Mathilde Reyssat and the gang.

Each of the persons mentioned here have contributed uniquely to my modest successes in research, and without them I could not write this document. They are all very very warmly thanked for these first and future passage times.

Chapter 1

Introduction

The goal of this document is to describe and make some connection through the scientific works produced with my involvement, particularly since finishing doctoral studies at the end of 2012. Broadly, these works address the question of *how boundaries affect the transport or mobility of soft condensed matter*. To give a some meaning to what we mean by boundaries in this document, we make a slight distinction. On one hand, we consider the first few molecular layers — be they polymeric macromolecules, the first few fluid layers, or the atoms or monomeric units separating two phases. This interface, even if just a few molecular layers thick, can drastically alter the slip boundary condition [1, 2], which is so important at micro- and nano-scales for determining the structure and dynamics of flow. On the other hand, we can also consider the box that contains the soft matter in question; examples include the hard, "simple" [3] surface of a silicon wafer or glass cover slip, an air medium above a thin polymer film, or the soft walls of a PDMS microchip. Of course, even this modest hard boundary can have major impacts on the transport of, for example, colloidal particles as a result of the no-slip hydrodynamic boundary condition and associated velocity gradients. Diffusion along these gradients gives rise to a nontrivial advection-diffusion coupling that engender the enhanced spreading dynamics called Taylor dispersion [4–6]; furthermore, if this classical no-slip condition is applied on a soft boundary, and even while it is the standard hydrodynamic recipe at macroscopic scales, the resulting hydrodynamic stresses may deform this former and in turn drastically modify the flow and particle transport [7, 8].

In this previous, first paragraph, the three main topics covered in this manuscript have thus been briefly described. These are: (*i*) the hydrodynamic boundary condition and surface mobility of polymeric liquids; (*ii*) Taylor dispersion —that is, the advection-diffusion coupling that leads to enhanced particle spreading dynamics— near interfaces and in pre-asymptotic temporal regimes; (*iii*) the coupling between elasticity and hydrodynamics in micro- and nano-fluidic contexts. Next, we provide a short overview of the main concepts necessary to understand the presented works in Chapters 3, 4 and 5. Especially for the polymer outline, these basic concepts are mainly textbook descriptions of the phenomena at play; a few basic elements of current research appear in the sections on interfacial interactions, diffusion and elastohydrodynamics. The following chapter contains the main ingredients of the experiments performed and the minimal theoretical frameworks used to interpret them.

We then begin to describe the research works, with contextual introductions provided at the beginning of each of the associated chapter sections. A short conclusion chapter makes finally an attempt to link these research topics, especially in the context of my future plans for research. An appendix describing some of the other works that I have not covered in detail is included in the end.

In writing the different chapters, I have made an effort to combine the yin and yang of continuity and self-containment. This means that each chapter and each section is briefly connected to the previous or following ones in a concluding or introductory paragraph. Then, the work to be described is put into context with respect to the specific literature surrounding the topic and finally the specifics of our work are described. The hope, therefore, is that an interested reader should be able to read any section or any number of sections in a self-contained manner, while very motivated readers should have a feeling for the connection between each of the works in reading the document 'from-A-to-Z'. Lastly, in the scientific discussion of the middle chapters, I may have glossed over details of certain calculations, or, some technical rigour of the experimental methods at play may be missing. As each section is describing a previously-published result, the hope is that readers interested in such details will accept to find them in the associated articles, wherein such rigour has been demonstrated to the best of our abilities.

1.1 Basic concepts

Before a detailed discussion of polymer films with thickness on the order of a few tens of nanometers to a few tens of micrometers, we briefly describe some key concepts polymer physics [9–11] describing chain conformations in bulk, in solution and in the presence of ions, their free energies, polymer overlap in solution and entanglement, along with some basic concepts in polymer melt and solution rheology, shear thinning and the glass transition.

In following subsections, we describe other basic concepts including surface tension, electrostatic theory and the slip boundary condition in a short section devoted to surface energetics and surface stress. A brief discussion of diffusion near interfaces follows, also including an overview of the basic concepts of Taylor dispersion; this chapter closes with some elements of elastohydrodynamics that are needed for the final scientific chapter of this manuscript. Readers already familiar with these subjects may skip directly to Chapter 2 or to Chapter 3.

1.1.1 Bulk polymer physics

Polymer chain dimensions: melts, solutions, polyelectrolytes

For the case in which a sample is composed of polymer chains that are much longer than a so-called persistence length [11] of a few to ten monomers for most synthetic polymers, *the conformation of the chains in a melt at equilibrium is that of a Gaussian random walk*. Here, the melt refers to a condensed matter system for which there is no solvent present. Cotton and co-workers [12], as well as many others as reviewed by Fetters and co-workers [13], demonstrated this hypothesis using small-angle neutron scattering experiments. The data, obtained from samples composed of mixtures of

deuterated and hydrogenated chains and over many independent chain lengths, is exceptionally-well described by the Debye function [11]. Such a function considers scattering from random-walking objects with radius of gyration[1] $R_\mathrm{g} = a_\mathrm{m} N^{1/2}/\sqrt{6}$, where a_m is the effective monomer size and N the number of statistically-independent monomers. To give an order of magnitude, the typical monomer size is 1 nm, while N is on the order of 100 to 1000. We thus expect chain sizes in the range of a few, to 100 nm.

Deviations in size from the mean end-to-end distance of the first and last monomers on the chain, $\langle R \rangle = \sqrt{6} R_\mathrm{g}$, can be predicted based on random walk statistics. Such considerations give a Gaussian probability distribution [9–11] for R with typical variance $a_\mathrm{m}^2 N$ up to a numerical prefactor. These probability distributions are important for the physics of polymers as they permit to define the entropy of a polymer chain, and thus its free energy. Considering that the free energy is mainly entropic and due to the enumeration of different random walking configurations for a given chain size, the Gaussian probability density gives a free energy quadratic in the chain size and proportional to kT, the thermal energy. Melt polymer chains are thus entropic Hookean springs. In the standard polymer references cited above, this molecular force law is used to compute the macroscopic bulk modulus for elastomers with strand length N. The result is

$$G \approx \frac{kT}{a_\mathrm{m}^3 N} \ , \tag{1.1}$$

giving moduli of some kPa to an MPa, and orders of magnitude less than the typical moduli of GPa for covalent and ionic solids. The entropic nature of the chain configuration, giving kT for the energy scale and combined with the effectively enlarged length scale due do the fact that $N \gg 1$, is responsible for the softness of rubbery materials.

Introducing a solvent that dissolves the polymer molecules, and considering only a single isolated molecule in dilute solution, Flory [9] hypothesised the essential balance leading to chain conformations in solution. Herein, an excluded volume interaction is added to the configurational one of the previous paragraph. As the density of monomers controls the number of such exclusion interactions, the tendency is to swell the chain whereas the configurational contribution above tends to minimize the chain size. The balance of the two contributions leads to a so-called Flory radius, $R_\mathrm{F} \sim N^\nu$ where the exponent, while an irrational number [14], is given by $\nu = 0.588\cdots \approx 3/5$ for excluded volume interactions.

Besides excluded volume interaction, an aqueous solvent may implicate ions that dissolve off of the polymer chain backbones. As such, ionic polymers, or polyelectrolytes, may swell even more than suggested from the excluded volume interactions of the previous paragraph [15]. For such polyelectrolytes, the Coulomb repulsion renders the excluded volume interaction weak in comparison to the chain stretching [11]. Therefore, balancing the Coulomb repulsion with the configurational entropy of a single chain leads to a linear scaling of the chain size for polyelectrolytes, $R_\mathrm{pe} \sim N^\nu$ with $\nu = 1$, valid until the solution's screening length is equal to the chain size. The

[1] That is, the root-mean-square distance from the center of mass of the chain.

prefactor in this linear relationship depends on the linear charge density of the chain, the Debye (Eq. 1.3) and Bjerrum (Eq. 1.4) lengths [16] and monomer size.

Whether excluded volume or Coulomb interactions serve to swell the chain in solution, distinct chains begin interact with one another at all times above the so-called overlap concentration, ϕ_*, with ϕ the volume fraction of monomers. This overlap concentration, depending on the chain length and dominant swelling mechanism, is defined by the concentration in monomers of the pervaded volume in the dilute case; that is, $\phi_* = a_\mathrm{m}^3 N/R_\mathrm{F}^3$, $\phi_* = a_\mathrm{m}^3 N/R_\mathrm{pe}^3$ for Flory and polyelectrolyte chains, respectively; we thus generally have $\phi_* \sim N^{1-3\nu}$. Well above this concentration, a key length scale is the correlation length, ξ, the typical distance needed to cross another chain. This length is defined as the size of a dilute, swollen chain with monomer number g needed to reproduce the experimentally chosen concentration, thus $\xi \sim g^\nu$ giving $\xi \sim \phi^{-\nu/3\nu-1}$. Since we only encounter one chain below this scale, dilute statistics apply to the correlation segment; meanwhile, the correlation "blobs" —as they are called in the literature— are space filling, which leads to a screening of the swelling mechanisms. In essence, since each blob is identical in a statistical sense, the chain conformation is a random walk. For these semi-dilute random walks, a_m is replaced with ξ and the N with the number of blobs N/g, giving $R \sim \xi(N/g)^{1/2}$ for semidilute chains, both ξ and g dependent on the concentration.

Polymer chain dynamics, entanglement and rheology

Just as in the end of the previous subsection where a distinction between short and long chains in solution was made, there exists an important dynamical distinction between "short" and "long" chains. For the melt, above a polymer-specific *entanglement* molecular weight [13], $M_\mathrm{e} = m_0 N_\mathrm{e}$ with m_0 the molar mass of a monomer, the microscopic topological configuration becomes altered. This "topology" may for example refer to the number of times a polymer chain is forced to "bend" around another one. In the simulation literature on the so-called *primitive path analysis*, this bending idea is made quantitative [17, 18]. More quantitatively predictive for physico-chemical systems, when the polymer chain shares enough of its pervaded volume with enough other chains according to the overlap criterion [13, 19], it can be considered as being entangled. Beyond the entanglement length for a polymer chain, many macroscopic material properties are drastically altered. Two examples include but certainly are not limited to:

- the zero-shear viscosity of a polymer melt, which scales as $\eta_\mathrm{R} \sim N^1$ for short chains, consistent with the Rouse model, whereas empirically we have that $\eta_\mathrm{rep} \sim N^{3.4}$ for long chains. The viscosity thus explodes for chains with $N > N_\mathrm{e}$. The long-chain limit is well-captured by the "reptation" models of Doi and Edwards, and de Gennes, which gives $\eta_\mathrm{rep} \approx \zeta N^3/(a_\mathrm{m} N_\mathrm{e}^2)$, where ζ is a monomer-monomer friction coefficient;

- bulk, oscillatory shear rheology shows a remarkable, and sometimes decades-long plateau in the storage modulus. This plateau modulus, G_N^0, in anology with rubber elasticity is linked to the entanglement molecular weight through $G_\mathrm{N}^0 \approx \frac{kT}{a_\mathrm{m}^3 N_\mathrm{e}}$ in analogy with rubber elasticity. In this naïve but instructive view, entanglements are considered as crosslinks for times less than the so-called reptation time, $\tau_\mathrm{rep} \sim N^3/N_\mathrm{e}$ [10, 11], the latter describing the relaxation

time of an entangled chain in the melt. By contrast, short chains in the melt are described by the Rouse model and relax in a time $\tau_{\mathrm{R}} \sim N^2$.

These two examples are characteristic of melts, the same distinction could be made with respect to semidilute polymer solutions, with N_{e} becoming dependent on the concentration. In this document, we will not encounter such entangled solutions and so we will not describe them further.

While the work presented here does not concern entangled polymer solutions, we will present work implicating semidilute polymer solution rheology in Section 4.1. For this rheology, an important concept is the molecular polymer relaxation time. As we are concerned with short chains in semidilute solution, the Rouse model is appropriate, predicting that the relaxation time is squared in the number of correlation blobs, with a Zimm-like relaxation time for a blob providing the prefactor, thus $\tau_{\mathrm{sd}} \approx N^2\phi^{(2-3\nu)/(3\nu-1)}$. For a semidilute unentangled solution, shear rates satisfying $\dot{\gamma} \sim \tau_{\mathrm{sd}}^{-1}$ define the crossover into non-Newtonian rheology. Specifically, such solutions can be shear thinning [20–24], *i.e.* with a viscosity decreasing with shear rate. Such observations could be explained with an approach exploiting the Pincus blob model, with the main physical ingredient being that polymer relaxation modes with relaxation time larger than the inverse shear rate do not contribute to the dissipation. Therefore, with fewer modes dissipating at high shear rate, the viscosity decreases according to a power law, $\eta \sim \dot{\gamma}^{-1/2}$, as described by Colby *et al.* [21] with the exponent 1/2 deriving from the Rouse dynamics being square in the number of participating monomers.

Lastly, we make a few brief and simplistic comments on the temperature dependence of polymer dynamics. Generally, polymer liquids become slower to relax at lower temperatures. While many systems could be described by an Arrhenius-like behaviour, the segmental dynamics of polymer liquids display a stronger temperature dependence of the Vogel-Fulcher-Tammann type. In VFT dynamics, the temperature in the Arrhenius law shifted by a finite amount, giving a divergence at a finite temperature usually associated with the glass-transition temperature, T_{g} [11, 25]. These dynamics are often measured using rheology, *i.e.* by measuring the viscosity, or related quantities [26], as a function of temperature. Complementary measurements of the thermal expansion coefficient or heat capacity as a function of the temperature give evidence for some kind of a phase transition at the same temperature, yet the question of whether this is an thermodynamic transition or a purely dynamical one is open [27]. When polymers are confined, such measurements of the glass transition temperature can be modified and seem to depend on the experiment. These modifications have thus spawned an ongoing, decades-long debate [28, 29] as to the origin of the anomalous T_{g}, to be addressed in Section 3.2.1.

1.1.2 Interfacial energetic interactions and hydrodynamic stresses

We now discuss cases for which complex fluids are contained in flow domains with thickness on the order of the chain size or a few tens of times larger, and perhaps up to 100 times. In this context, several interfacial concepts are key for the following work.

First, surface tension[2], γ, is defined thermodynamically as the energy per unit

[2]We note here a collision of the notations used throughout my work: in the thin-film case, we

area, or dynamically as a force per unit length. As described in many works [16, 30, 31], surface tension arises from a lack of intermolecular interactions that would have been present in the bulk. For the liquids to be considered here, this lack of neighbours at the interface gives rise to an energy cost of order kT per molecular (*i.e.* monomeric) area. Below a scale of a few millimeters [31], surface tension is normally a dominating force (over gravity, *e.g.*). Indeed, the surface tension gives rise to the Laplace pressure [31], *i.e.* the pressure discontinuity encountered on crossing a material interface. This pressure is given by

$$p = \gamma \times 2\mathcal{C} \ , \tag{1.2}$$

where $2\mathcal{C} = \rho_1^{-1} + \rho_2^{-1}$ is twice the interface mean curvature, ρ_i being the principal radii of curvature. Thus, when a sample can be prepared with curvature gradients at the interface, a flow can be observed [32–36]. These capillary-driven flows are especially the subject of the work presented in Chapter 3.

Besides the surface tension, surfaces embedded in a liquid may develop a surface charge if ions leave the surface and dissolve into the solution. In such a case, the Poisson-Boltzmann theory [16, 30] can be applied to show that, approximately, the charge density in the vicinity of the wall decays exponentially from the surface when the surface potential is small compared to kT/e, with e the fundamental charge unit. The Debye length,

$$\ell_{\mathrm{D}} = (2\ell_{\mathrm{B}}c)^{-1/2} \ , \tag{1.3}$$

determines the exponential decay length for the near-surface charge density and potential, with the Bjerrum length

$$\ell_{\mathrm{B}} = \frac{e^2}{4\pi\epsilon kT} \ , \tag{1.4}$$

$$\tag{1.5}$$

being the distance at which two elementary charges in a medium with permittivity ϵ have electrostatic energy equal to kT. Like-charged particles near such a surface thus experience an electrostatic repulsion which for our purposes it suffices to express as

$$U_{\mathrm{el}} = U_0 \exp(-z/\ell_{\mathrm{D}}) \ , \tag{1.6}$$

where U_0 depends particularly on the surface potentials of the particle and the wall and the particle size. Such an electrostatic repulsion helps to build a depletion of particles near the wall through a Boltzmann factor, thus the probability density scales with $\mathcal{P} \sim \exp(-U_{\mathrm{el}}/kT)$. Having described these few potential-derived interactions, we turn now to dissipative interactions between a liquid and the substrate.

Under flow, the hydrodynamic slip boundary condition (BC) at the solid-liquid interface may be non-trivial especially at nanoscales. When the size of a fluid system approaches molecular dimensions, unexpected and intriguing results are often

use γ to represent the surface tension; whereas in Taylor dispersion studies, $\dot{\gamma}$ represents the shear rate. Both are essential and ubiquitous in the relevant studies, and the context should make the distinction clear.

observed. In the polymer physics community, one well known example is the idea that, in the fully liquid state, molecules may slide along a confining solid boundary. This effect, called slip [37–46], was proposed by Navier in the early 19th century. It was not until only a few decades ago, however, that this slip idea has gained traction within the rheology community, starting with the observation of anomalous polymer mobilities in oscillatory shear experiments observed in the late 1980's [47] and in part motivated by the pioneering remarks of de Gennes [3,48]. As described in Chapter 3, the precise value of this BC may have dramatic impacts on the morphology and dynamics of flowing polymer films, especially when flow-domain sizes are below a few hundred nanometres.

Considering a stress balance at an ideal solid-liquid interface, having no specific interaction besides friction, we consider that the stress from the solid on the liquid is proportional to the velocity there. Meanwhile, the stress in the liquid is proportional to the shear rate, which allows us to collectively write

$$\begin{aligned} \sigma_{\rm sl} &= \kappa v_x \quad ; \quad \text{solid-liquid stress (ideal)} \ , \\ \sigma_{\rm ll} &= \eta \partial_z v_x \quad ; \quad \text{liquid-liquid stress} \ . \end{aligned} \tag{1.7}$$

Invoking Newton's third law, we equate these two stresses thus

$$\sigma_{\rm sl} = \sigma_{\rm ll} \ , \tag{1.8}$$

giving the ideal slip length as

$$b_{\rm ideal} = \frac{\eta}{\kappa} \ . \tag{1.9}$$

Normally, we expect that the solid-liquid stress is monomeric in nature, while the viscosity is polymeric. This realisation [3,48] allowed for the hypothesis that polymer molecules sliding on ideal surfaces could attain huge slip lengths, recalling that the viscosity scales with N^3 and N possibly reaching order 10^3 or 10^4.

Here we can separate two related lines of investigation linked to surface-tension-driven flows: experiments designed to investigate the origins or important physical ingredients controlling the slip phenomenon; and, experiments designed to elucidate the importance of the slip boundary condition on the ensuing flow; these problems are addressed in Chapter 3, while certain elements of the polymer and interfacial physics described above appear in each of the chapters.

1.1.3 Near-surface colloidal transport

Colloidal particles are susceptible to the thermal fluctuations of their environment, as often provided by an aqueous bath. The diffusion coefficient of an object is given by the Einstein relation [49]

$$D_0 = \frac{kT}{\zeta} \ , \tag{1.10}$$

where the friction coefficient, ζ, is given by the proportionality between drag force and velocity. For the classical case of an isolated particle in a viscous medium, we have the Stokes drag coefficient [50], $\zeta = 6\pi\eta a$, with radius a typically in the range

of a few nanometers up to a couple of micrometers, and to be distinguished from the subnanometric monomer size, a_m, above.

For a particle near an interface, friction of the liquid in between the particle and the wall is modified as compared to the isolated-particle case. This modification gives a position-dependence to the friction coefficient, $\zeta = \{\zeta_x(z,a), \zeta_z(z,a)\}$ where z is the distance between the particle center and the wall, and the two components denote diffusion parallel and perpendicular to the wall. Computation of the drag coefficients represents an involved, yet known, hydrodynamic calculation that was first done by Brenner [51]. There is no closed form solution, yet both the x- and z-components can be expressed as infinite series [51] and several closed-form asymptotic solutions exist. Indeed, the Reynolds [52] drag force f_d on a particle near a wall in the lubrication limit shows the main features: the dependence is stronger in the vertical direction, scaling with the inverse of the gap, $h = z - a$, between the particle and the wall, and thus diverging. This can be compared to the horizontal drag, scaling with the inverse of the gap plus an offset; the parallel drag force saturates to a finite value. Many workers, especially since the '90's devoted efforts to studying diffusion near a wall [53–57] and it remains an actively investigated topic [58–60]. We will come back to these effects briefly in Chapter 4.

The above considerations were for the case in which the fluid is not in motion, hydrodynamic transport giving a second component of the motion. If the particle suspension is thus transported through a pipe, the advective transport and diffusive motions become coupled. Hydrodynamically, a non-Brownian particle would remain on a single streamline throughout its entire trajectory. Taylor considered, however, the case for which a diffusive chemical species builds a concentration profile, $c(x,r,t)$ in a cylindrical pipe (radial coordinate r) with a parabolic flow profile of mean flow velocity v_0 along the x direction only. The advection-diffusion equation for this problem is thus

$$D_0(\partial_r^2 c + r^{-1}\partial_r c + \partial_x^2 c) = \partial_t c + v_x(r)\partial_x c \ . \tag{1.11}$$

In this problem, a key timescale is the one taken for a particle or molecule to diffuse across the flow domain of size h, given by $\tau_z \approx h^2/D$. When the considered advection time is much larger than τ_z, Taylor argued to develop an effective diffusion equation describing the concentration profile [4], as $\mathcal{D}_x \partial_{x_1}^2 c = \partial_t c$ with x_1 following the mean flow and superficially identical to the static diffusion equation with a constant diffusion coefficient. It should be noted, however, that this simple equation indeed hides a considerable transformation of the original advection-diffusion equation. Indeed, the key result is a dispersion coefficient defined as

$$\mathcal{D}_x = D_0\left(1 + \alpha \mathrm{Pe}^2\right) \ , \tag{1.12}$$

where the Peclet number, $\mathrm{Pe} = hv_0/D_0$, compares advective and diffusive transport, and the coefficient α is dependent on the flow profile and channel geometry. For Poiseuille flow in a cylindrical pipe we get $\alpha = 1/192$, while for the typical shear flows near a wall that will be studied in Chapter 4, the coefficient is $\alpha = 1/30$. Regardless of the flow geometry, Taylor dispersion thus gives rise to diffusive-like spreading that is much more rapid than pure diffusion, enhancements reaching orders of magnitude can be observed as long as the velocity gradients are sufficiently strong.

Shortly after Taylor's analysis of the solute dispersal problem, Aris [4] developed a formal method of moments for the analysis that would allow to go beyond the dispersion coefficient calculation whose result is presented above. Major contributions to the field were also made by Brenner whose text [6] goes well beyond the simple and foundational tracer particle theory of Taylor and Aris in a single pore.

1.1.4 Lubrication and Elastohydrodynamics

In order to induce a fluid to flow, a pressure gradient must be applied. This idea thus implies a pressure field throughout a fluid domain, and thus also acting on the boundaries. In typical works on hydrodynamics [50, 61, 62], these boundaries are normally assumed to be infinitely rigid, passive, and even "stupid" [3]. They thus simply play the role of a container and provide a location to terminate, or at least define according to a rule as in Eq. 1.8, the velocity at the boundary. Mathematically speaking, as hydrodynamic problems are generally governed by differential equations, these boundary conditions are essential, and the no-slip or 'other-slip' conditions are convenient. However, there are many practical situations for which the boundary of a flow domain is significantly perturbed by the pressure field inducing such flow, or wherein the objects suspended in a flow are greatly influenced by the stresses controlling the flow; we will now focus on the first case.

Indeed, as mentioned in the previous section, a spherical particle that approaches a wall at normal incidence forces the fluid to escape in the intervening region. In the lubrication regime for which the fluid gap is much smaller than the particle size, such a squeeze flow provokes an h^{-2} law for the pressure [50]. Sufficiently close to the boundary, therefore, this strong power-law dependence on the pressure must provoke some level of yielding of the surface a result of this hydrodynamic stress. In cases where the boundary is composed of soft matter, with characteristic moduli $G \approx 10 - 100$ kPa, and when the distances approach some micrometers or nanometers, hydrodynamic stresses are sufficient to deform the surface and thus modify the hydrodynamic flow.

The literature on elastohydrodynamics dates from the 19th century in the context of industrial lubrication [52] (*e.g.* gear contacts and friction and wear reduction). In this context, Reynolds considered a thin liquid layer of height h in a long fluid domain wherein the flow is predominantly in a direction perpendicular to the dominating velocity gradient [63], thus $v(x, y, z) \approx v_x(z)$ where we consider invariance in the y-direction and due to the separation of length scales we have $\partial_x v_x \ll \partial_z v_x$. Such an statement allows for the approximation that the pressure field, p is invariant along this gradient, considerably simplifying the governing equations. As described in many places [31, 32, 52, 63], the lubrication approximation thus gives rise to the Reynolds equation when a local Poiseuille flow with no slip is integrated to make a statement of local volume conservation

$$\partial_t h = \frac{1}{12\eta} \partial_x \left(h^3 \partial_x p \right) \ . \tag{1.13}$$

In typical hydrodynamic problems, h is fixed in some way. A simple example is constant height in space and time with a pressure prescribed at the ends of a conduit; in this case the characteristic linear pressure profile results. In other cases,

p is prescribed as a function of h – we will see this in the case of surface-tension-driven flows, and gravity-driven thin-film flows can be given as a further example [63, 64]. In such cases Eq. 1.13 is the only equation to solve.

In other cases, a surface may deform as a result of the pressure, and the surface deformation results itself from the solution of a bulk elasticity problem. In such cases Eq. 1.13 is not sufficient, and an elasticity law needs to be prescribed. The elastic and hydrodynamic equations thus become coupled. In Chapter 5, we will encounter two such problems. In the first [65], we consider a sphere that approaches a soft and porous layer for which a linear elasticity law allows for the prediction of a poroelastic Green's function defining the deformation on convolution with a pressure field. This pressure field is thus is self-consistently solved with the above Reynolds equation in the flow domain. Second, a simpler elasticity law is combined with the Reynolds one for the study of transient deformation in narrow microfluidic channels [66].

Having provided a few basic conceptual ingredients for the work that follows, we will in the next chapter provide an overview of the experimental approaches meant to elucidate the effect of boundaries and interfaces on the interfacial dynamics of soft condensed matter described in Chapters 3, 4 and 5.

Chapter 2

Experimental methods and general interpretations

In this chapter is provided an overview of the different experimental methods we used to probe soft matter at interfaces. Such an overview will include a brief description of the main practical aspect of the technique, along with basic theoretical frameworks needed for quantitative analysis of the data to be presented in the following chapters. The main techniques are stepped-film leveling and thin-film dewetting, along with total internal reflection fluorescence microscopy. While described to a lesser extent as they could be considered less central to the work presented here, microfluidics, atomic force microscopy and X-ray reflectivity were also used. Before entering the details, a brief overview of the different methods is provided in the following paragraphs.

For purely polymeric matter, we used stepped-film leveling[1] and dewetting. These are both thin-film-based techniques, wherein surface and interfacial tensions drive a hydrodynamic flow. Details of the dynamical air-liquid interface as measured using atomic force microscopy, and, for the case of the latter technique, the hole growth dynamics as observed using optical microscopy, provide information on the depth-averaged film mobility. Since boundary conditions pilot the volume debit (*i.e.* the depth-averaged mobility), these aforementioned height profiles can reveal the slip boundary condition, with slip lengths ranging from a few tens of nanometers to a few microns. These techniques were used in conjunction with surface functionalisation using, more often than not, self-assembled monolayers (SAMs), to study the dependence of the substrate/polymer-melt pair on the hydrodynamic boundary condition; while not exhaustive, examples include chain-length and polydispersity of the melt or the underlying substrate, and sub-T_g surface dynamics.

Total internal reflection fluorescence (TIRF) is a microscopy technique based on the creation of an evanescent wave. Using TIRFM, sub-wavelength particles can be imaged in the first few hundred nanometres of an interface when the wavelength of the illumination is chosen to excite fluorophores embedded in the particles. Combined with particle tracking under flow in a microfluidic channel, near-surface transport of colloidal particles in aqueous environments can be assessed. By transport, we refer to the combined advective and diffusive motions, in three dimensions and resolved

[1] While the stepped film technique was mainly developed during the PhD period, several works were completed in the proceeding years and those are discussed here.

to roughly 10 nm in each direction. In particular, quantitative streamwise velocity profiles $v_x(z)$ can be obtained as a function of the distance z from the interface generating evanescence. Similarly, displacement variances in the transverse and streamwise directions are available. These latter variance measurements allow for the assessment of, respectively, purely diffusive motions and Taylor dispersion. TIRFM was used in the group for the study of semi-dilute polymer solution boundary conditions as influenced by the near-surface rheology probed *in-situ*, and colloidal transport at the nanoscale and near interfaces.

These latter polymer-solution and Taylor dispersion studies were accomplished thanks to the use of microfluidics. Herein, conduits with micrometric cross section (*i.e.* typical lengths of 10 to 100 μm, with some exceptions) were produced using soft lithography [67]. Such microchannels were connected to pressure control and volume debit measurement devices.

2.1 Substrate and thin-film sample preparation

As the geometry of the samples used in the thin-film, polymer-melt studies is somewhat specific, in this section we describe the techniques used to prepare them. These samples are mainly the subject of Chapter 3. After briefly describing the substrate modification procedures for promoting slip hydrodynamic boundary conditions, the thin-film sample preparations are presented.

2.1.1 Self-assembled monolayers

A majority of the studies on the slip hydrodynamic boundary condition presented here made use of the highly controlled surface chemistry made possible by self-assembled monolayers. These SAMs have enjoyed widespread use in surface science, as described in several places [68–74], for their relative ease of preparation and reproducability. The molecules of concern here are mainly dodecyltrichlorosilane (DTS) and octadecyltrichlorosilane (OTS), respectively being composed of hydrogen-saturated oligomers of 18 and 12 carbon atoms. On one end, there exists a reactive group containing silicon and three chlorine atoms, these latter which dissociate in solutions prepared to functionalise the surface [71], while on the other a carbon with a triplet of hydrogen, thus saturating the carbon atom. These molecules are illustrated in Figure 2.1(a).

While many recipes exist in the literature for the preparation of OTS and DTS SAMs, the one used here was developed by the Jacobs group, described in detail and compared to others in Ref. [74]. Briefly recounting the procedure, Si wafers with native oxide are piranha etched and repeatedly rinsed with boiling, ultrapure water and then dried with a nitrogen stream. After this cleaning procedure, the wafers are briefly exposed to water vapor provided by boiling milliQ water, the resulting breath figure is allowed to dry momentarily and the wafer is immersed in a solution containing 0.25% by volume silane molecules dispersed in bicyclohexyl along with approximately 0.5% by volume of CCl_4, supposed to inhibit an uncontrolled crosslinking of the silane molecules. After several minutes of incubation, the wafers are rinsed with chloroform and the immersion/rinse is repeated twice, giving rise to

the self-assembled structure illustrated in Figure 2.1(b), as seen in Ref. [75].

The silanisation procedure described above provides reproducible monolayers with atomically smooth surfaces, the roughness being inherited from the underlying substrate. In Figure 2.2(a) is shown a characterisation of a typical OTS SAM by AFM in tapping mode, displaying the sub-nanometric roughness characteristic of Si wafers and the resulting SAMs. In part (b) is shown processed X-ray reflectivity [76] data for OTS, DTS and and intermediate hexadecyltrichlorosilane (HDS). Therein, the electron density profile perpendicular to the substrate is shown, displaying layers corresponding to the underlying Si, the native SiO_x layer, a head group corresponding to the terminal Si function of the silane, and a last layer representing the hydrocarbon tail. The "tail" layers are similar in size of the associated hydrocarbon molecules, D-, H- and O-TS containing 12, 16 and 18 carbon atoms along the tail. Physicochemically, the SAMs are hydrophobic, giving contact angles with water of roughly 110°, and giving estimated surface energies[2] of 25 mN/m [74, 77], consistent with typical surface tension values of liquid dodecane and octadecane [78].

We mention finally that teflon-like coatings have also been applied to substrates in order to render them hydrophobic and, in particular, to provide a slip boundary condition for the polymers under study. Such coatings were prepared by dissolving what we refer to by the trade names "AF1600" or "AF2400". These fluoropolymers have chemical structure poly[4,5-difluoro-2,2-bis(trifluoromethyl)-1,3dioxide-co-tetrafluoroethylene], with different chain lengths giving the different commercial names. These polymers are dissolved in a fluorinated solvent (typically fluorinert FC-72 or similar, from 3M). Dip coating a 1 wt% solution gives a film coating that can be annealed at temperatures above the polymer glass transition to promote adhesion to the cleaned (see above and Ref. [74]) underlying Si wafers. Then, floating of the polymer films proceeds as described in the next section.

2.1.2 Floating thin polymer films for model flow geometries

The preparation of samples described in Chapter 3 is heavily dependent on the use of floating delicate, nanometric films onto and from a water bath; the process is schematized in Figure 2.3. For the polystyrene mainly used here (PS, from Polymer

[2]Notwithstanding the non-equilibrium nature of measuring solid surface energies, in the Jacobs work these were estimated using the Good-Girifalco relation, with quoted advancing/receding contact angle hysteresis of 10°.

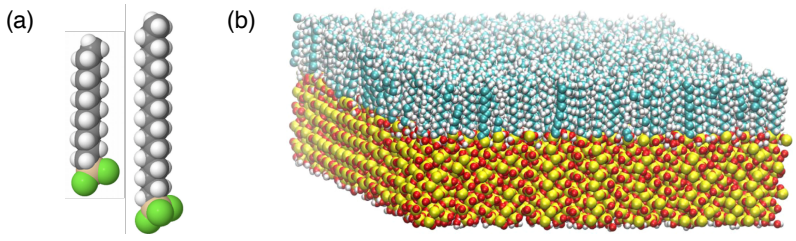

Figure 2.1: (a) Schematic illustrations of DTS (left) and OTS (right) molecules. (b) Illustration of molecular dynamics simulation of a DTS SAM with a coverage density of 4.5 nm^{-2} on 101 β-cristobalite SiO_2 substrate, for details see Ref. [75].

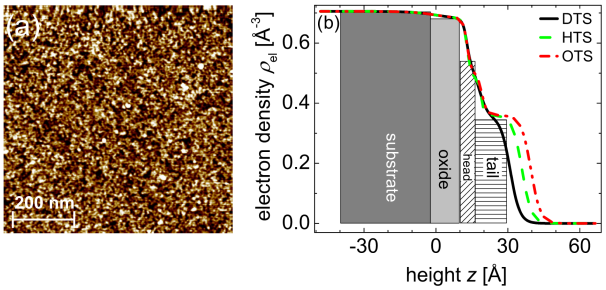

Figure 2.2: (a) AFM of an OTS SAM surface, with the color scale representaing a total vertical range of 1 nm. (b) Electron density as a function of depth normal to the substrate-air interface for the SAMs indicated in the legend. Images from Ref. [74].

Source or Polymer Standards Service and with polydispersity index normally less than 1.1), toluene (chromatography grade) was the most common solvent as it is volatile and a good solvent for the polymer. With concentrations typically of order 10^{-1} to 10^{1} percent by weight of PS in toluene, spin coating solutions [79–81] at 1000 to 4000 rpm onto mica or silicon substrates, films with the targeted thickness can be prepared, see *e.g.* Ref. [80]. These thicknesses were usually of order 100 nm, with a lower limit of around 5 nm and up to a micrometer or two.

Getting such thin films onto a water bath, Figure 2.3(a), is normally achieved using mica ("HI-grade" from Ted Pella Inc.) as a sacrificial substrate. After spin coating onto freshly cleaved mica, the film is scored using a scalpel into square sections of *ca.* 8 mm on a side, and the film is gently dipped onto the surface of an ultra-clean water bath (18 MΩ cm, from a MilliQ source) using fine-tipped, self-closing tweezers (Ted Pella Inc.). As mica is hydrophilic and the film is hydrophobic, this latter

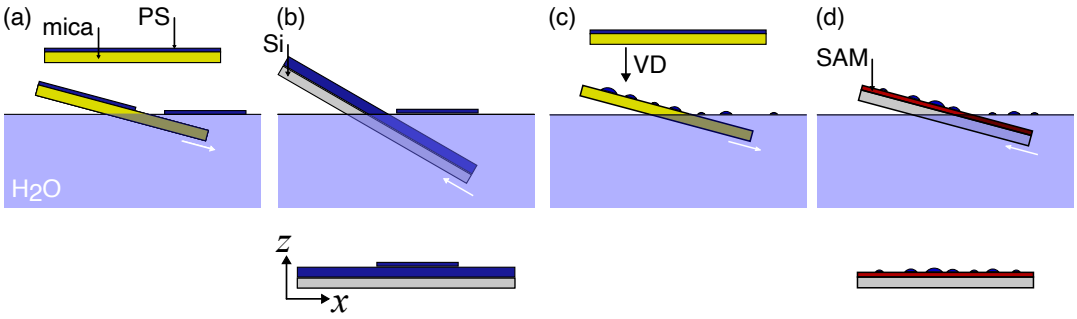

Figure 2.3: Schematics of film and sessile droplet preparation. (a) A thin PS film is floated from mica onto the surface of a clean water bath. (b) The previous film is picked up with a thin film of PS spin coated onto a Si wafer. The bottom part shows the resulting stepped film. For dewetting experiments, the Si film is instead decorated with a SAM or other hydrophobic layer, as in (d), this former layer which does not liquefy at the elevated temperatures used for dewetting. (c) To prepare droplets as in [43], vapor-saturated atmospheres lead to dewetting (VD) of the PS film on mica, with a low (*i.e.*, roughly 10°) contact angle; such droplets can then be floated onto a SAM.

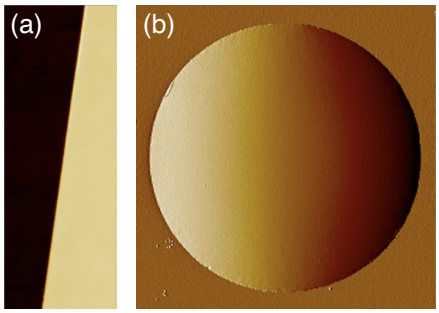

Figure 2.4: As-prepared (a) stepped film (b) and sessile droplet as measured by AFM. The image widths are respectively 6 μm and 10 μm; the height scale in (a) is 100 nm while in (b) we plot the error signal, related to the derivative of the topography; the contact angle of the droplet is roughly 10°.

delaminates from the mica and floats on the water surface being pulled taught by surface tension; the elevated glass transition temperature of PS approximately 100 °C for sufficiently long PS ensures that the films do not evolve significantly during the floating manipulations done under ambient conditions. This floating technique is ubiquitous in the thin film polymer literature, while many papers could be cited, a few examples include [82–86]; we note also that, in addition to mica, any hydrophilic substrate can be used [87–90].

Once a film is on the water bath, it can be picked up using a desired substrate. Here, these substrates are silicon wafers that have previously been prepared with either an underlying polymer film (for stepped-films) or a hydrophobic layer such as a SAM or a fluorinated polymer (for dewetting). This procedure is shown in Figure 2.3(b). A variant of this floating procedure is to first expose the films on mica to atmosphere saturated with a good solvent vapor [91,92]; the films absorb the solvent, become liquid and dewet, leaving behind a collection of spherical caps on the substrate, each with a contact angle controlled by the substrate, vapor phase composition and polymer [92,93]. This vapor dewetting (VD) is shown in Figure 2.3(c), and was used in particular for the droplet dewetting work of Ref. [43] described in Section 3.2.2, having followed our droplet spreading study [94] wherein the underlying substrate was coated with a PS layer.

The final samples are shown in the bottom row of Figure 2.3(b) and (d). We note in particular the coordinate axes which are mainly consistent through the works to follow: unless otherwise noted, the dominant flow direction is taken to be along the x-axis, while the substrate-normal direction is taken along the z-axis. Representative AFM images of as-prepared samples, a stepped film (a) and a sessile droplet (b), are shown in Figure 2.4.

2.2 Stepped-film leveling

Capillary forces tend to make a liquid surface smooth. According to the imposed boundary conditions and geometry, the equilibrium state [31] may be a spherical domain for a freely suspended droplet, a barrel or clam shell for a droplet deposited

on a fiber, or a flat film for a large enough[3] volume of fluid covering a substrate. In stepped film leveling, this third example is operative. When the surface topography is not flat, surface tension drives a flow that tends toward the equilibrium flat state [32–36]. The stepped-film leveling geometry may be considered as the simplest non-flat geometry for the study and exploitation of capillary driven flow.

In Figure 2.5(a) is schematically shown an as-prepared stepped film, with base height h_1 and step height h_2. Recalling the Laplace law [31], we note that the pressure jump across an interface is proportional to the interface curvature and the surface tension γ. Therefore, the corners at the bottom and top of the stepped film present the film with an unbalanced pressure, from the top to the bottom corners. According to the Stokes law[4], such a pressure gradient drives a flow, giving rise to a characteristic height profile, $h(x,t)$ after a time t. Such a height profile is illustrated in Figure 2.5(b).

In Figure 2.5(c) is shown an optical micrograph, from Ref. [96], of an as-prepared stepped film of PS with $M_w = 65$ kg/mol, referred to as PS(65k). The component films are roughly 100 nm thick such that the grey scale value is an indication of height under illumination with light at 633 nm wavelength, the left side being thinner than the right side and the thicknesses roughly corresponding to minima and maxima of the thin-film reflection interferences [97]. Upon annealing at 180 °C for roughly 10 h, the width of the transition zone between dark and bright is much larger, suggesting that the stepped film has flattened.

Making direct observations of the topography of stepped films, AFM was used in Ref. [95]. The principal experimental observation in a stepped-film leveling experiment are reproduced in Figure 2.6(a). Therein, three stepped films with $h_1 \approx h_2 \approx 100$ nm were annealed at 140 °C for the times indicated. Broadening occurs due to surface tension and is slower for higher molecular weight (*i.e.* for higher viscosity).

Describing the height profiles of Figure 2.6(a) quantitatively can be achieved in the context of the lubrication limit of the Stokes equation, expressing momentum

[3] In making this statement, we assume that surface and intermolecular forces are negligible.

[4] Reynolds numbers are always many orders of magnitude less than 1 in these films, due to the large polymer melt viscosities of 1 kPa s or more, nanometric length scales, with velocities on the order of μm/min.

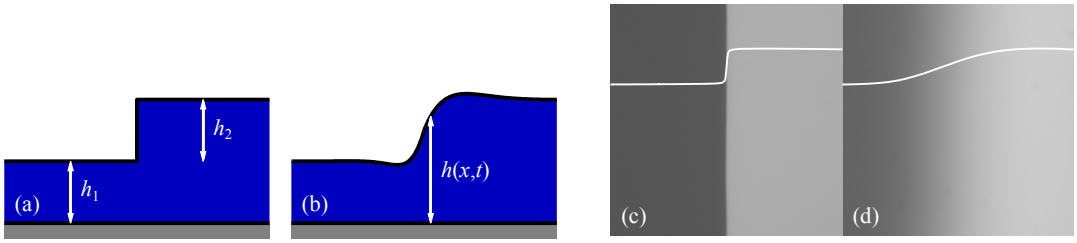

Figure 2.5: (a) A schematic of the stepped-film leveling experiment, showing an underlying silicon wafer (grey) and films (blue) composing the initial step. (b) After annealing the surface develops a height profile; reproduced from from [95]. (c),(d) Optical micrographs of a PS stepped film before and after annealing, reproduced from Ref. [96].

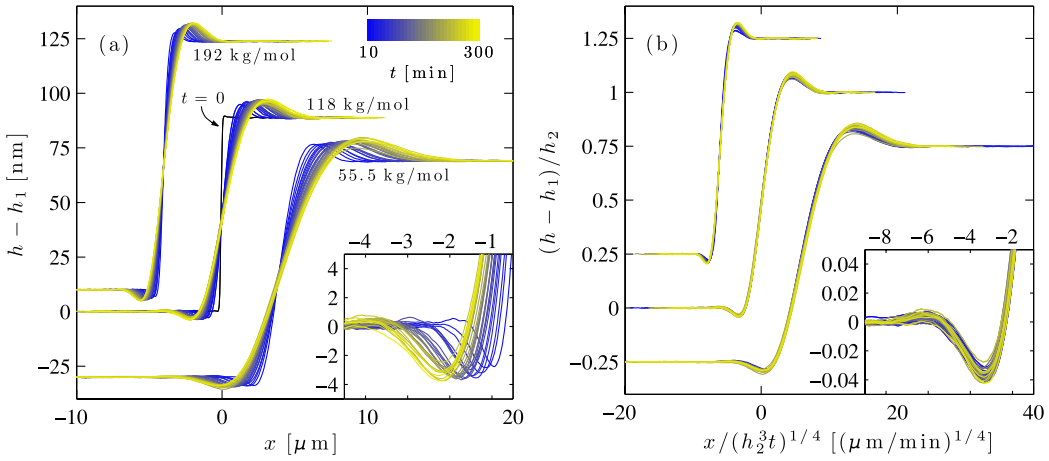

Figure 2.6: (a) AFM height profiles of leveling PS stepped films with identical geometry $h_1 \approx h_2 \approx 100$ nm. (b) Rescaled, self-similar profiles of (a). The insets show a zoom on the 'dip' region of the PS(118k) stepped film. Reproduced from Ref. [95].

conservation in the over-damped case as $0 = -\nabla p + \eta\nabla^2\mathbf{v}$. Invoking a separation of length scales in the horizontal and vertical directions, that is $h_1, h_2 \ll w$, where we take w as the characteristic horizontal distance between extrema of the height profiles[5], it can be shown as has been done in many standard references [32, 50, 63] that the height profile obeys

$$\partial_t h + \frac{\gamma}{3\eta}\partial_x\left(h^3\partial_x^3 h\right) = 0 \qquad ; \qquad \text{no slip}\ , \tag{2.1}$$

expressing a local volume conservation; this expression is referred to as the thin film equation (TFE) in the following. Thus, the term inside the spatial derivative on the right-hand side is a volume flux. The term in h^3 is the film mobility, having integrated a characteristic, quadratic Poiseuille flow under a pressure gradient with no slip at the solid-liquid surface and no stress at the air-liquid interface, and the third derivative in the height represents the Laplace pressure gradient with the local pressure being $p = -\gamma\partial_x^2 h$ in the lubrication limit.

Even while Eq. 2.1 is nonlinear and thus has no known general solution, it can be simply shown that a self-similar solution [98] is admitted by defining $u = x/t^{1/4}$ as could simply be guessed based on the dimensionality of the system. Non-dimensionalising the equation with $H = h/h_2$ $X = x/x_0$ and $T = \gamma h_0^3 t/3\eta x_0^4$, and defining $U = X/T^{1/4}$ gives a single self similar solution to Eq. 2.1 in the variable U, satisfying $h(x,t) = F(U)$. The appropriate rescaling of the raw data of in Figure 2.6(a) is shown in Figure 2.6(b), with a single prefactor, *i.e.* a horizontal stretch, along with the ratio h_1/h_2 completely describing the experimental self similar profiles which are computed numerically [99]. in Figure 2.7 is shown a comparison between

[5]Whereas for a diffusion equation of second order there is typically no local maxima for an initially monotonic profile, the high order of the governing partial differential equation for the free-surface lubrication scenario gives rise to the characteristic "dip" and "bump" that are localized near the transtion zone between h_1 and $h_1 + h_2$.

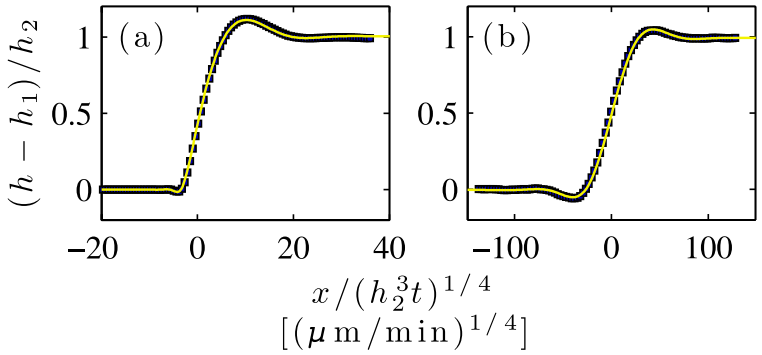

Figure 2.7: (a) AFM height profiles (squares) of PS(15k), leveling stepped films with geometries (a) $\{h_1, h_2\} = \{30, 193\}$ nm and (b) $\{h_1, h_2\} = \{174, 32\}$ nm, each after 10 min of annealing at 140 °C. The lines are numerical resolutions of the governing equation with the corresponding film geometry. Reproduced from Ref. [95].

theory and experiment for two different film geometries and annealed under similar conditions. The computed profiles show good agreement with the experiment, usually to within 1% of the film height, as also described in numerous other configurations [100–103] since our original works [95, 99, 104]. Converting to dimensionless units, we see that, with the film heights measured, comparing experimental to theoretical profiles provides the capillary velocity, γ/η, and since the surface tension hardly varies with the molecular weight, practically, the stepped film is a nanoscale rheometer as it provides the film viscosity. Extracting more sophisticated information related to the surface mobility or boundary conditions, not available to a traditional rheometer due to the large volumes used and the lack of a free surface, as will be discussed in Chapter 3.

2.3 Dewetting and slip

Dewetting is the process whereby a thin liquid film, which may have a thickness anywhere from a few nanometres to a few microns or more, recedes from an underlying surface under the action of surface tension [38, 83, 105–114]. This dewetting is schematically indicated in Figure 2.8(a) and (b). In addition to the surface tension that drives the flow, and when the films are sufficiently thin and with polymer melts wherein the viscosity is many decades higher than for monomeric liquids, viscous dissipation is responsible for limiting the retraction of the film from the substrate. Hydrodynamic slip at the solid-liquid interface may alleviate some friction enhancing the dynamics, as we describe presently.

Practically, we used two different methods for accessing the properties of polymer films through dewetting, which we illustrate using two data sets. First, we track of the dynamics of hole opening using optical microscopy [38, 113–116]. This relatively simple experiment requires a sequence of images, as in Figure 2.8(c), capturing the hole opening. Since the films we observe are thin, the reflection and interference of white light gives them a thickness-dependent color. The case shown in Figure 2.8(c) is for PS films with thickness of approximately 125 nm, resulting in a blue color for

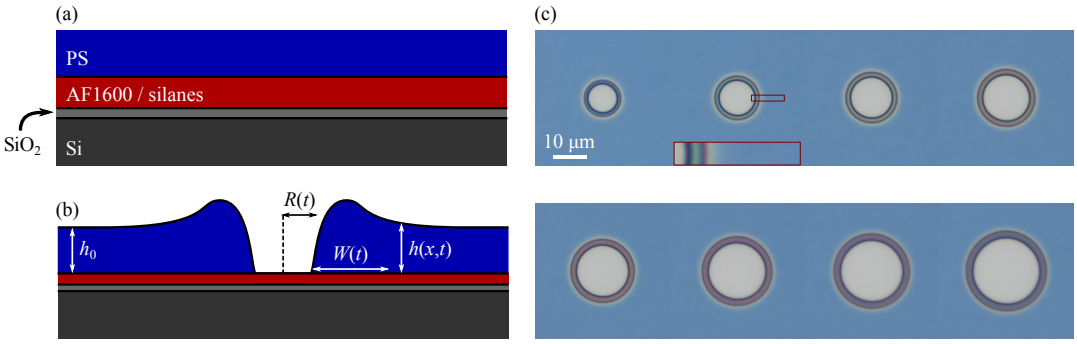

Figure 2.8: (a) A schematic of the thin-film dewetting experimental layer structure, showing an underlying silicon wafer, a thin (*ca.* 2 nm) silicon oxide covering, a hydrophobic layer and a polymer film. (b) Schematic of the dewetting film, showing a single hole with radius R in a film with height h_0. (c) Optical microscopy of hole growth in a PS(10k) film with initial thickness $h_0 = 125$ nm at 110 °C, images taken at 5 min intervals; the inset highlights an optical rim profile, the region typically investigate using AFM as in Figure 2.11. (a) and (b) reproduced from Ref. [42].

the undisturbed film. When the Si substrate is exposed, the white light is mainly reflected, giving a clear indication of the position of the contact line. This contact line can be tracked in time according to a threshold on the intensity and circular fits of the intensity profile giving the radius, R. In Figure 2.9(a) is shown an example of the hole opening dynamics for nearly-identical, unentangled PS(10k) films dewetting from two different substrates [42]. In blue, the undisturbed film thickness was $h_0 = 102$ nm and the underlying substrate was AF1600. In red, we had $h_0 = 93$ nm for a film dewetting from a DTS SAM.

A first remark concerning the data in Figure 2.9: even while the polymer film thicknesses were nearly the same, the dynamics are rather distinct for dewetting from the two substrates. Since the chemistry of the underlying substrate is different, the surface tensions, γ, are distinct and thus the driving force changes. However, the solid-vapor surface tension of AF1600 ($\gamma_{sv} \approx 15$ mN/m) is rather much lower than that of DTS ($\gamma_{sv} \approx 26$ mN/m), we thus expect the driving force to be higher on

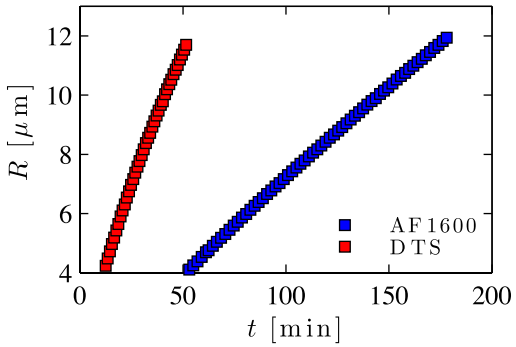

Figure 2.9: Dynamics of hole growth for PS(10k) films dewetting at 110 °C on AF1600- and DTS-coated substrates. See text for film details. Data from Ref. [42].

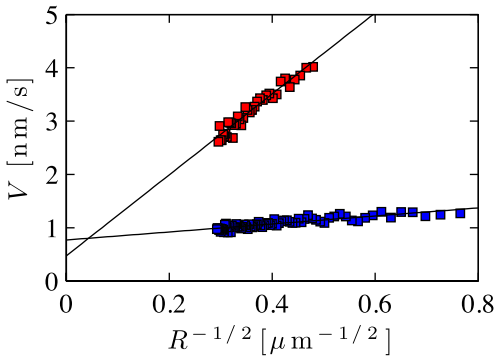

Figure 2.10: Rescaled hole growth dynamics for the films represented in Figure 2.9: contact line velocity, V, as a function of the inverse quare root of the contact line radius. Data from Ref. [42].

the AF1600 substrate even while the dewetting is slower. The discrepancy could be resolved by a differing solid-liquid friction, however, which can be manifested by a slip hydrodynamic boundary condition.

For dewetting without slip, it is well known that the retraction velocity is proportional to the liquid-vapor surface tension and (for small angles) to the cube of the contact angle, θ, at the three-phase contact line [31, 115, 117]. In particular, the dissipation in this situation is assumed to be concentrated near the contact line such that the dissipation rate does not depend on the size of the dewetting rim (*i.e.* the distance between the contact line and the undisturbed film in Figure 2.8), and thus the velocity is constant with hole size:

$$R \approx \frac{\gamma}{\eta}\theta^3 t \qquad \text{no slip} , \tag{2.2}$$

By contrast, for the full-slip case the dissipation should occur throughout the liquid in the rim that can be observed building up in the image sequence of Figure 2.8. For purely viscous dissipation, it is well known then that the velocity is rim-size dependent, with a balance of powers and a self-similarity argument [38, 77, 116, 118] giving that the radius grows with a non-linear temporal power law

$$R \sim t^{2/3} \qquad \text{full slip} , \tag{2.3}$$

In between these two extremal slipping regimes, the dissipations can be combined, as done by Jacobs and coworkers [42, 77, 116, 118]. The resulting dynamics for the radius does not give pure power law dynamics, but can be expressed as

$$\frac{dR}{dt} = V_0 + \frac{K}{\sqrt{R}} \qquad \text{partial slip} , \tag{2.4}$$

where $K \sim b/\sqrt{h_0}$ (see references for prefactors). Written as such, the dynamics of hole growth can be used to give a graphical diagnosis of slip: the intercept gives information on the contact angle, surface tension and viscosity, while a non-zero slope is indicative of a partial slip condition and the film height.

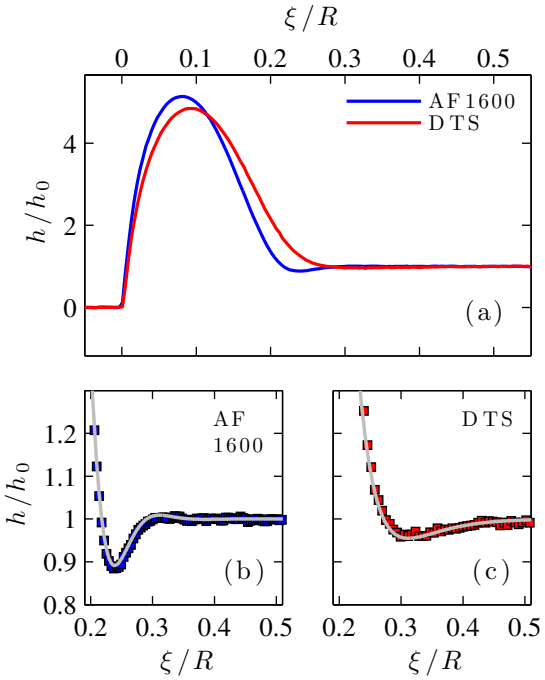

Figure 2.11: (a) Rim profiles associated to the dynamical data shown in Figs. 2.9 and 2.10. (b),(c) Zoom on the rim relaxation toward the undisturbed films for the indicated substrates. Data from Ref. [42].

To this end, in Figure 2.10 we show the data from Figure 2.9 scaled according to Eq. 2.4. The suggested dynamical representation indeed shows straight lines for each data set, with a steeper slope for the DTS data as compared to that of the film dewetting from AF1600. This indeed suggests a larger slip length for the PS-DTS pair at this dewetting temperature.

In order to confirm that the slip length for the PS-DTS pair is larger than that for the PS-AF1600 pair, we come to our second method for assessing slip: analysis of the dewetting rim profiles using AFM. The inset of Figure 2.8(c) shows an optical rim profile. On the far side of the rim, one can observe a slightly yellow band as the rim collected during dewetting, and having conserved the volume of the film within this rim, joins the undisturbed film. In Figure 2.11 we show AFM measurements of this region for the data represented in Figures 2.9 and 2.10, scaled by the undisturbed film height and the contact line radius, R, ξ being the horizontal coordinate with its origin at the contact line; to show how the interface can have an impact on the rim shape, in Figure 2.12 are shown examples in 3D of height profiles taken for two different molecular weights, near to and well above the entanglement molecular weight, on the same substrate. Remarkably, the profiles selected in Figures 2.11 and 2.12 are distinct, in that they do not join the undisturbed film in precisely the same way. Indeed, in the normalised representation, the perturbation of the undisturbed film reaches farther for the DTS substrate than for the AF1600 one, and farther for the higher molecular weight film than for the lower molecular weight one. This is a second indication for larger slip in the PS-DTS pair as can be quantified using the

hydrodynamic analysis as follows.

The details of the interpretation of such rim profiles were described at length by the Jacobs and Wagner groups [39, 42, 77, 120–122]. Briefly, and in a 2D Cartesian geometry of the Stokes equation, the flow is represented using stream functions ψ in a frame translating with the moving contact line under a capillary driving force. The free interface is thus determined by volume conservation (the fluid film does not evaporate), surface tension and the film mobility expressed through the boundary condition and viscous dissipation. In particular, the relaxation of the film into the undisturbed profile is described as a perturbation to the undisturbed state, and can be fit using a superpositions of damped exponentials. The characteristic inverse length scales, k, depend in particular on the slip length and contact line velocity. Quantitatively, this dependence is expressed through the characteristic equation given by

$$\left(1+\frac{h_0}{3b}\right)(h_0k)^3+4Ca\left(1+\frac{h_0}{2b}\right)(h_0k)^2-Ca\frac{h_0}{b}=0\ , \tag{2.5}$$

obtained by the linearization of the Stokes equation for the stream functions. In this characteristic equation the inverse length scales, k, are accessible in the dewetting experiment through the AFM topography measurements and fitting to the profiiles as a superposition of damped exponentials. The capillary number $Ca = \eta V/\gamma$ is accessible from data as in Figure 2.9 and Figure 2.10. The velocity V is taken at the moment when the dewetting was quenched to obtain the AFM height profiles. In practice, it is often difficult to distinguish two such length scales, k; however, the hole opening dynamics can be used to obtain a capillary number once the capillary velocity, γ/η is known (see the previous section on stepped-film leveling, or the intercept of Eq. 2.4). As such, Eq. 2.5 can be solved for the slip length, b. In Ref. [42], for the data shown in Figure 2.11(b) and (c), we obtained $b_{\mathrm{DTS}} = 1500 \pm 200$ nm and $b_{\mathrm{AF1600}} = 50 \pm 40$ nm, consistent with the dynamical data seen in Figures. 2.9 and 2.10.

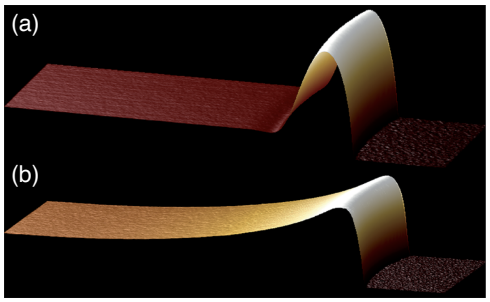

Figure 2.12: Dewetting rims for films with thickness, h_0, of 120 nm and 170 nm on AF2400; in both cases the horizontal extent of the images is 15 μm along the rim profile. For (a) the film was PS(28k) at 120 °C and for (b) PS(490k) at 150 °C. Data from Ref. [119].

2.4 Total internal reflection fluorescence microscopy

Total internal reflection evanescence permits the observation of objects placed within typically the first micrometer of an interface, this latter often between a glass coverslip and some aqueous environment. The Axelrod group pushed the development for its surface sensitivity in imaging biological samples [123, 124], cells *e.g.*, in order to gain better signal to noise ratio. Following those developments, the biological community embraced the technique, recent examples including single-molecule detection for diagnostics [125]. In the '90's, the Prieve group used TIR to study soft condensed matter [126], with the ability to measure quantitatively the intermolecular forces [16] between a colloidal particle and the glass-water interface. With their measurements under mainly equilibrium conditions, van der Waals, electrostatic, gravitational forces as well as randomized thermal forces were revealed.

TIR has thus become an important, nanoscale technique for measuring static surface interactions, especially in soft matter. The push for dynamics accompanied the development of particle tracking velocimetry (PTV) methods for automated tracking of large particle numbers. Respectively, the Breuer group [127, 128] made pioneering efforts and the Yoda [129] group also made early strides in the dynamical direction and, collectively, reported the first indications that monomeric liquid slip could be measured using TIR coupled with PTV.

In our studies, typically-100 nm-diameter, fluorescent polystyrene nanoparticles are observed under evanescent illumination at a glass-water interface. By combining microfluidic flows and particle-tracking velocimetry, the near wall velocity profile and particle displacement statistics are obtained. In the following paragraphs we outline first the optical setup, described in detail in Refs. [46, 130, 131] and in our articles of Refs. [132–134].

TIRFM Optics

The principal relation that allows for TIR microscopy to be quantitative is the exponential dependence of the illumination intensity with distance from the totally-reflecting interface [136]. Indeed, for TIRF, the excitation intensity is given by

$$I(z) = I_o \exp\left(-\frac{z}{\Pi}\right) \ , \tag{2.6}$$

where I_o is the intensity at the glass-water interface, z is the distance from the wall, and Π is the evanescent decay length. This latter is proportional to the illumination wavelength, and is furthermore determined by the indices of refraction of the interface media (here n_{g} and n_{w} being the glass and water indices) and incident angle, θ, of the incoming light. From Ref. [136], we have that

$$\Pi = \frac{\lambda}{4\pi}\left(n_{\mathrm{g}}^2 \sin^2\theta - n_{\mathrm{w}}^2\right)^{-1/2} \ . \tag{2.7}$$

We thus see that an appropriate estimate of the evanescent decay length requires an optical setup that can control, here, the incident angle of a laser beam incident on a glass-water interface. The following paragraphs thus describe our method for achieving such illumination, and an angle measurement technique that we developed.

As of my arrival at Gulliver in 2018, TIRF microscopy had been used by the MMN group of Patrick Tabeling in preceding years (*cf.* Refs. [46, 137]). The layout schematically indicated in Figure 2.13. Briefly, and after passing through a beam expander, the beam is passed through a lens mounted on a translation stage just before the microscope. The beam focus moves across the back focal plane of the objective as schematically shown in Figure 2.14(a), and inspired by the system described in Ref. [130]. Depending on the position X_M of the entrance indicated in this latter figure, the exit angle can be controlled [138] according to the transfer function of the objective. Such angle control is necessary to predict the evanescent decay length, Eq. 2.7.

Typically, this exit angle is measured by projecting the beam through a spherical lens and measuring its position along a horizonal plane above the microscope [46, 131]. This measurement is a macroscopic one, typically done 1 m or more from the objective. Gabriel Guyard, however, developed [135] a method to measure the incident angle through the microscopic translation of the spot along the image plane. This micrometric horizontal translation (δx_μ) is a result of similar translations in

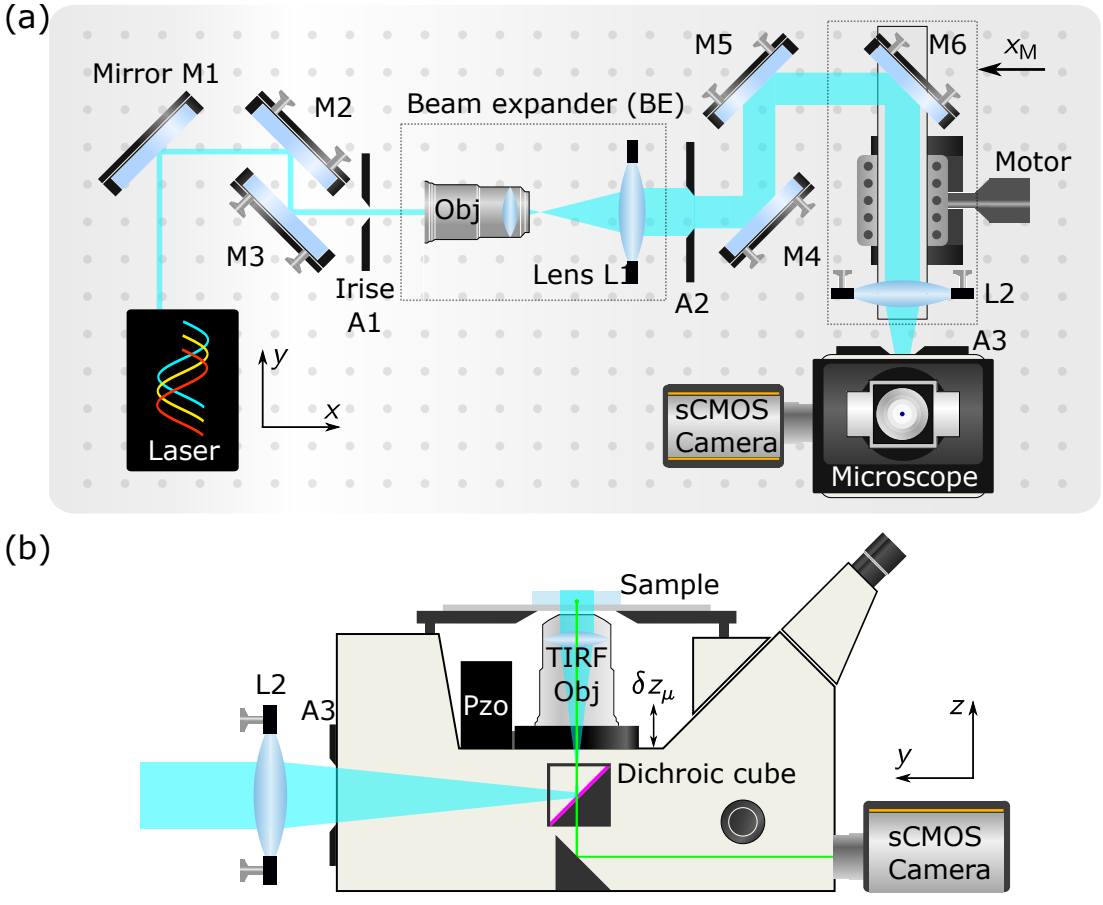

Figure 2.13: (a) Top-view and (b) side-view schematics of the optical setup used for preparation of a total internal reflection condition, giving rise to an evanescent wave inside a microfluidic channel atop a microscope. From Ref. [135].

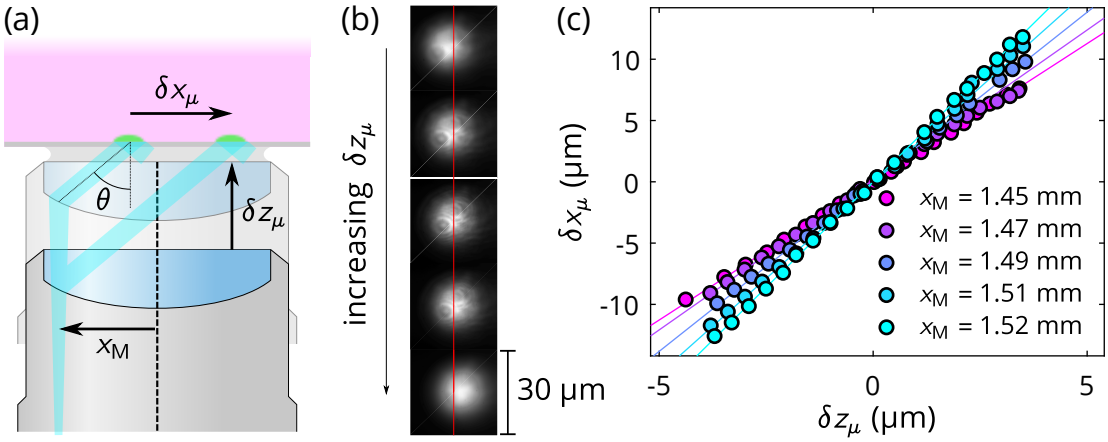

Figure 2.14: (a) Illustration of the microscopic, objective-translation method for measuring the angle of a laser beam exiting a microscope objective. Adapted from Ref. [132], and appearing in Ref. [135]. (b) Raw images showing the laser fluorescence spot translation with objective repositioning. (c) Horizontal fluorescence spot displacement as a function of objective displacement, for various positions, X_M, of the lens focussing the laser beam to the back focal plane of the objective.

the vertical direction of the objective (δz_f), controlled by a piezoelectric objective mount, as indicated in Figure 2.14(a). In Figure 2.14(b) is shown the translation of the fluorescence spot as the piezo is moved in the vertical z-direction for the microscopic angle measurement. In part (c) is plotted the position of the laser spot in the image plane as a function of the vertical objective displacement. The slope of the data in (c) allows for the determination of the angle, and is consistent with the macroscopic method after appropriate geometric corrections of the latter method are accounted for [132,135]. In Figure 2.14(c), the angles achieved range from 63° to 70°, enabling TIR for a glass-water interface.

2.4.1 Near-surface structure and dynamics from TIRFM particle tracking

With the TIRF microscope set up as described above, it is possible to collect images of particles advected by a pressure-driven flow inside a microfluidic channel, as indicated in Figure 2.15(a). For our purposes, standard channels have dimensions $\{L, w, h\} = \{80 \times 10^3, 180, 20\}$ μm and standard particles are 100 nm, carboxylate-modified latex particles with fluorescence excitation and emission peaks at 505 nm and 515 nm, respectively (Thermo-Fisher, F8803 FluoSpheres); for the particle-tracking experiments these are the objects used unless otherwise noted. Videos of such standard particle tracking experiments, with images taken at 400 Hz (2.5 ms per frame) can be found in the supplementary information of the articles by Vilquin and co-workers [133, 134], in particular at the "HAL" preprint server. The image processing and particle detection shown in Figure 2.15(b) give the x, y particle coordinates in the image plane as the position of the Gaussain maximum (*e.g.* red and blue curves), and the position in z is given by the particle's fluorescence intensity

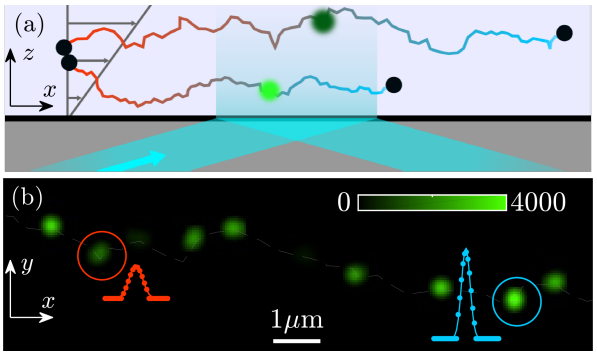

Figure 2.15: (a) Illustrations of the particle tracking experiment, with two example particles and their trajectories shown. (b) A single particle advected by a flow with 12.5 ms increments between superimposed frames. Inset graphs (red and blue) show the intensity profiles for measurement of the particle's distance from the fluid/solid interface.

though the evanescence relation of Eq. 2.6. Typically the evanescent decay length Π is of order 100 nm, and given the intensity of the particle at the wall I_0 and our camera sensitivity, the measurements can be made for 100 nm fluorescent particles as far as approximately 1 μm from the wall. We note that additional considerations related to the objective's finite depth of field and particle polydispersity are described elsewhere [133, 139]. While these considerations preclude a unique identification of an individual particle's altitude, the statistical effect is weak.

As individual particles are tracked, individual trajectories as in Figure 2.15(b) can be constructed. Of course, an individual particle trajectory is statistically insignificant for the particle residence times available in these experiments (roughly 20 ms for the standard particles under 488 nm illumination, giving roughly 10 particle observations). Therefore, an ensemble of particles, typically 10^4 per experimental condition (*e.g.* applied pressure and solute concentration), are observed allowing to access statistical averages. To illustrate, in Figure 2.16 are shown the reconstruction of particle ensemble evolutions for three different imposed pressures (columns) and five different times (rows). To construct such images, each individual, independent particle in a frame is cropped and its trajectory, as in Figure 2.15(b), is placed at a common spatio-temporal origin. From such ensembles, the average displacement is obtained, as is the diffusion and dispersion. Knowing the temporal evolution of particle positions and their heights as in Figure 2.15(b) gives the opportunity to measure the velocity profile of the fluid near the wall. In our experiments, and owing to the geometry of our channels with typically 20 μm height, we measure the linearised part of the velocity profile near the surface as the 1 μm illumination zone is just 5 % of the entire channel height. In Figure 2.17(a) are shown the velocity as a function of the distance from the liquid/solid interface, measured for standard particles in water, with a variation in the pressure at the channel inlet distinguishing the curves. As expected, when the pressure increases, the velocity of a particle at a given height increases; furthermore, for a given pressure, the velocity profile is linear with the

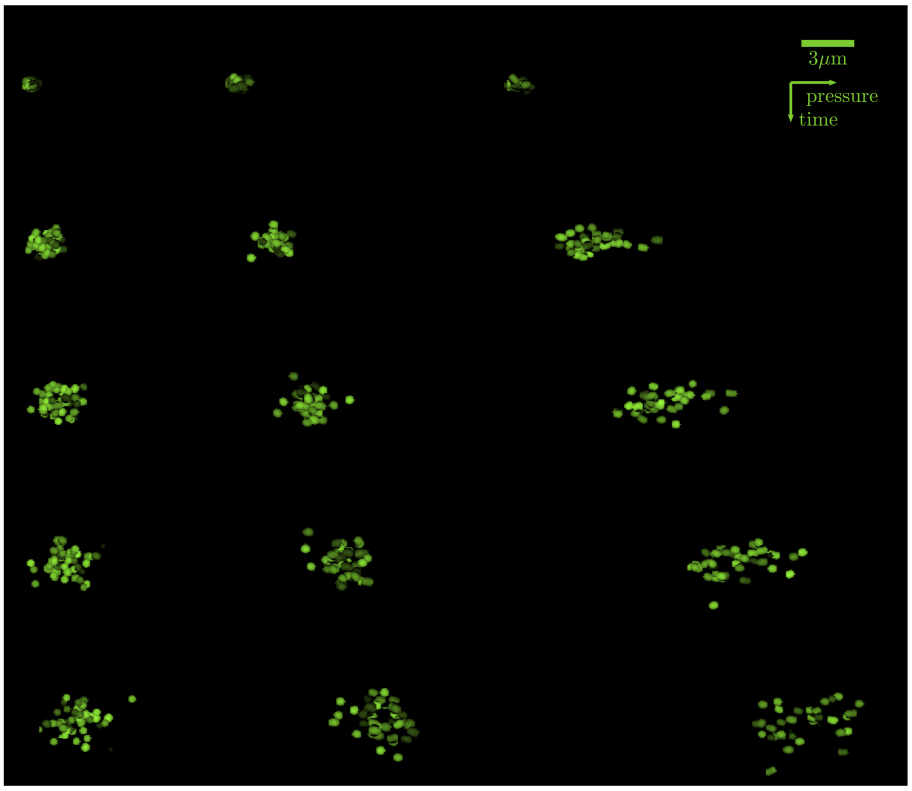

Figure 2.16: Experimentally reconstructed, particle-ensemble trajectories. Each particle in the initial (partial) ensemble of 10^2 particles (top row, after 5 ms) is followed for five different times (following rows, with delay times 22.5, 40, 57.5, 75 ms.). Different columns show different pressures (20, 40, 60 mbar in a standard channel) along with the resulting increased velocity and streamwise dispersion.

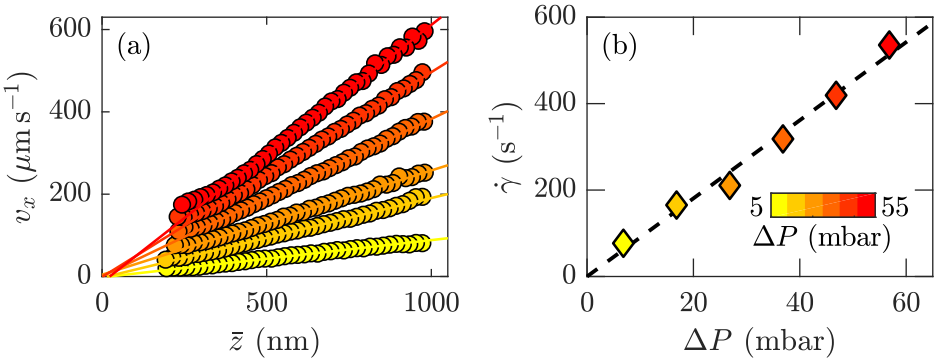

Figure 2.17: (a) Streamwise velocity as a function distance measured by TIRFM velocimetry for 100-nm diameter particles in water, and in a microfluidic channel with dimensions of 20 cm, 180 μm, and 20 μm in length, width and height. (b) Shear rate as a function of pressure drop from the velocity profiles in (a). Reproduced from Ref. [133].

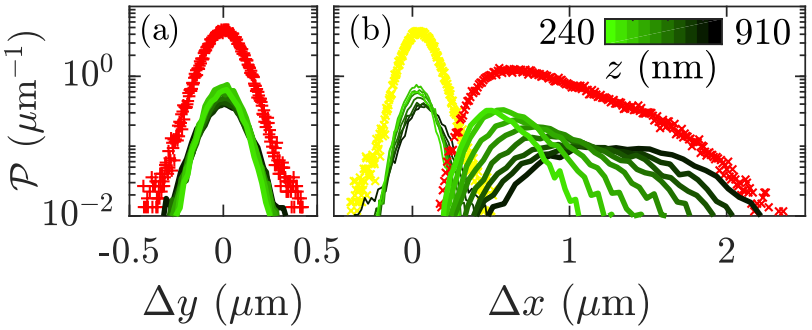

Figure 2.18: Displacement distributions for 100 nm-diameter particles in water for observations made using TIRF microscopy. (a) Displacements perpendicular to the flow direction and parallel to the solid/liquid interface at a pressure of 55 mbar across the flow channel; distributions are identical for other pressures. (b) Similar displacement distributions along the flow, for 5 mbar (yellow) and 55 mbar (red). Each yellow or red distribution is furthermore broken down according to particle altitudes (*i.e.* different particle intensities), represented by the green-black curves; the average particle heights are indicated by the colour bar. Reproduced from Ref. [133].

distance[6]. This linear velocity profile is characterised by the shear rate, $\dot{\gamma}$ (*i.e.* the slope of the velocity profile), shown as a function of pressure in Figure 2.17(b). By analysing the shear rate as a function of pressure, the viscosity of water is recovered within error given the geometry of our channels and the pressure/shear-rate relation. Therefore, the TIRFM microscope is a near-surface rheometer [132] that can be used to assess, *in situ*, the impact of this rheology, for example, on the near-surface transport. The interplay between this rheology and the boundary condition of semi-dilute polymer solutions will be investigated in Chapter 4.

Having covered the possibility to measure velocity profiles, we now describe how using the same image sequences it is possible to measure the second moments of the particle displacements, giving access to diffusive properties of the transport. In Figure 2.18(a) are shown, for two pressure drops across the same microchannel as in Figure 2.17, displacement distributions of Δy transverse to the flow and normal to the solid-liquid interface. These distributions permit a measurement of the diffusion coefficient, $D_y = \sigma^2_{\Delta y}/2\tau$ from the variance of the displacements $\sigma^2_{\Delta y}$ and time delay τ; here a single frame was used giving a delay time of 2.5 ms; the Gaussian widths of the distributions in Figure 2.18(a) are consistent with the Stokes-Einstein prediction for the bulk diffusion coefficient of a colloidal particle with radius a, that is $D_0 = kT/6\pi\eta a$, with η the viscosity of water and kT the thermal energy as described in Ref. [133]; therein, this agreement was shown also for different Newtonian liquids and particles of different size. Similarly, distributions of Δx in the streamwise direction in Figure 2.18(b) can be used to compute the dispersion coefficient $\mathcal{D}_x = \sigma^2_{\Delta x}/2\tau$, *cf.* Eq. 1.12. A marked difference between the high-pressure cases can be noted between the x and y distributions, a result of the advection-diffusion coupling known

[6]Nonlinearities are visible and can be explained by more rigorous analyses in [46, 133, 139, 140] that consider the effects of Brownian motion, the finite depth of field of the microscope objective and particle polydispersity.

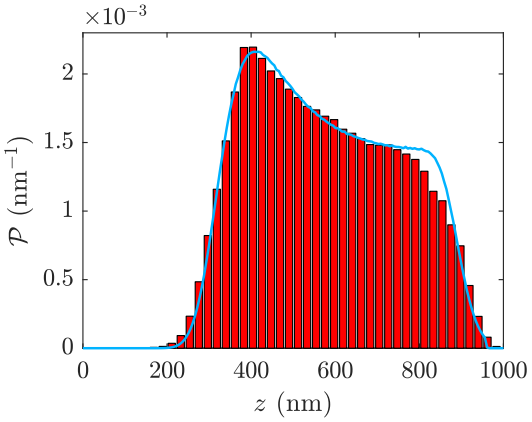

Figure 2.19: Near-wall signal intensity distribution (SID), as a function of the log-intensity, $z = \Pi \log(I_0/I)$ of 100-nm, fluorescent F8803 nanoparticles in ultrapure water; see also Figure 4.7. Reproduced from Ref. [133].

as Taylor dispersion described above and in detail in Chapter 4. We note finally that the global distributions in yellow and red, comprising all particles observed, can be sorted according to their initial altitudes (*i.e.* intensity); the green-black curves in Figure 2.18 demonstrate such a breakdown, allowing to investigate diffusion according to the particle altitudes.

A last type of information that is examined in typical TIRFM experiments in our group is the statistics of particle altitudes relative to the glass-water interface. After Ref. [139], these are called signal intensity distributions (SID) since they are rooted in the intensity of particles; to make connection to the altitudes of Eq. 2.6, we normally consider the log of the intensities. In Figure 2.19, we show an experimental signal intensity distribution (red bars). Near the wall, a depletion zone is a result of the electrostatic interactions between the particle and the glass-water interface; the large-z cutoff is due to the finite camera sensitivity. The blue line is a theoretical description, including the an electrostatic interaction [16] of Eq. 1.6, impacting mainly the near-wall shape of the distribution, along with optical details including the depth of field of the objective of roughly 400 nm and polydispersity. For details we refer to Refs. [46, 139, 140] along with a complete description of our fits in the appendix of Ref. [133]. These observations allow for the determination of near-wall surface-particle interactions, simultaneously to accessing the dynamical velocity profiles and diffusive behaviours. Thus, Figures 2.17 – 2.19 constitute the main experimental basis on which studies of the structure and dynamics of aqueous soft matter can be achieved, as will be discussed especially in Chapter 4. Meanwhile, the leveling and dewetting methods described in the previous Sections 2.2 and 2.3 will be exploited in the next chapter.

Chapter 3

Surface and interface mobility of polymer melts

In this chapter, after having briefly described in Section 1.1 some of the basic ingredients from polymer physics, we describe how stepped-film leveling and dewetting thin polymer films elucidated the importance of the boundaries for the temporal and morphological evolution of thin polymer films. First [141], the dynamical and morphological details of AFM-measured height profiles allowed to distinguish the different slip boundary conditions, suggesting adsorption on substrates previously considered "ideal" under de Gennes' definition [3, 48], described in Section 3.1. Next in Section 3.2, we exploit the morphological discrimination of height profiles to elucidate mobility mechanisms above and below the glass transition. Therein we show in two subsequent subsections that, first, the free-surface mobility dominates film relaxation below the bulk T_g. Second, we consider the effect of a buried interface. For this purpose, the equilibration relaxation pathway, as revealed by the sequence of morphologies of a dewetting microdroplet prepared as described in Figure 2.3(c), is shown to be highly sensitive to the slip hydrodynamic boundary condition of the solid-liquid interface. Noting that a subtle change in the composition of the underlying substrate can promote drastic changes in the boundary condition of a short-chained polymer melt [39,42,77], we turn our attention to the composition of this solid-liquid interface for slip control. Here, two emblematic examples are taken wherein careful preparations of, in turn, the substrate [142] and overlayed polymer film [143] provide insights on how, respectively, the interfacial, solid boundary or polymer chain conformation may affect solid-liquid friction.

3.1 Thin film equilibration dynamics

When a thin film with an arbitrary topography is placed onto a substrate of low surface energy, the equilibrium state is a single droplet with a contact angle given by, notwithstanding the possibility of contact angle hysteresis, the Young condition. Even while this Young's droplet is the equilibrium state, a real experimental system rarely gets there. First, a flat film with thickness beyond a few nanometers is normally metastable [110,112], requiring a nucleation event to prepare a contact line which then dewets. Therefore, the film will, in a first instance, begin to level out according to

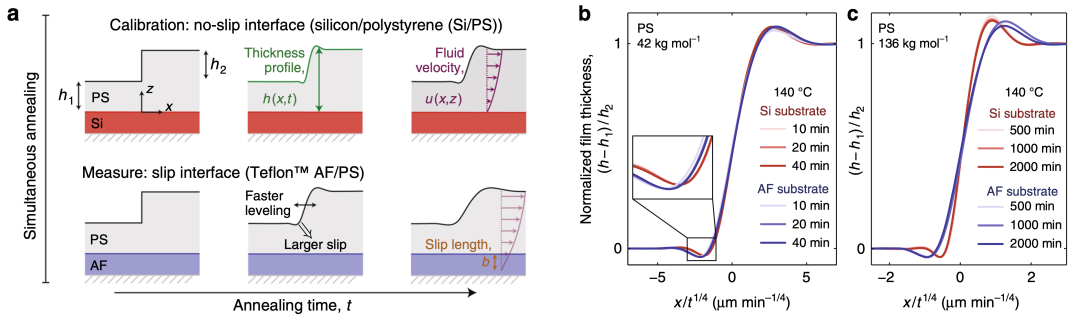

Figure 3.1: (a) Stepped-film leveling for the investigation of the slip boundary condition of thin films. Simultaneous annealing of stepped films on Si and on AF1600, AF2400 or OTS/DTS SAMs were carried out. (b) Self-similar AFM height profiles for stepped films of two different molecular weights on the indicated substrates and for the indicated annealing times. Reproduced from Ref. [141].

the lubrication theory of Eq. 2.1, provided appropriate modifications to the mobility term are introduced. We thus describe such modifications next.

Indeed, beyond viscometry permitted by Eq. 2.1, stepped film experiments are also sensitive to the hydrodynamic boundary condition and for the cases in which the slip length could be considered "weak" under the detailed discussion of slip regimes provided by Münch *et al.* [144], the dominant viscous dissipation arises from shearing[1] in the x-velocity along the z-direction, that is the shear stress σ_{xz}. For the weak-slip cases we consider, the mobility of Eq. 2.1 is modified as

$$h^3 \to h^3 + 3bh^2, \tag{3.1}$$

giving

$$\partial_t h + \frac{\gamma}{3\eta}\partial_x \left[\left(h^3 + 3bh^2\right)\partial_x^3 h\right] = 0 \qquad ; \qquad \text{weak slip} \ . \tag{3.2}$$

Therefore, slip is expected to engender two effects on leveling experiments. First, the interfacial transport promotes faster levelling as the mobility is higher; second, slip modifies the resulting self-similar profile due to the added term of order h^2 in the evolution equation.

In order to make a test of these predicted morphological and dynamical effects, experiments as illustrated in Figure 3.1(a) were carried out. Stepped films were prepared on Si as well as different surface-treated Si wafers described in Section 2.1.1. Simultaneous annealing of the two stepped-film samples, prepared from the same spin coated films, was necessary to control the sensitivity of polymer viscosity on temperature and possible preparation artefacts related to spin coating and rapid solvent evaporation [145–147]. The obtained height profiles for two molecular weights are shown in Figures 3.1(b) and (c). Considering either data set (b) or (c) individually, the differences between the self-similar curves from different substrates should

[1] By contrast, in cases for which the slip length is so large that there is hardly any shear along the film height, this dominant dissipation may change over to a σ_{xx}-type, for example, or a pure shear for the case of bursting films [107] – we will not encounter such cases here for the leveling films.

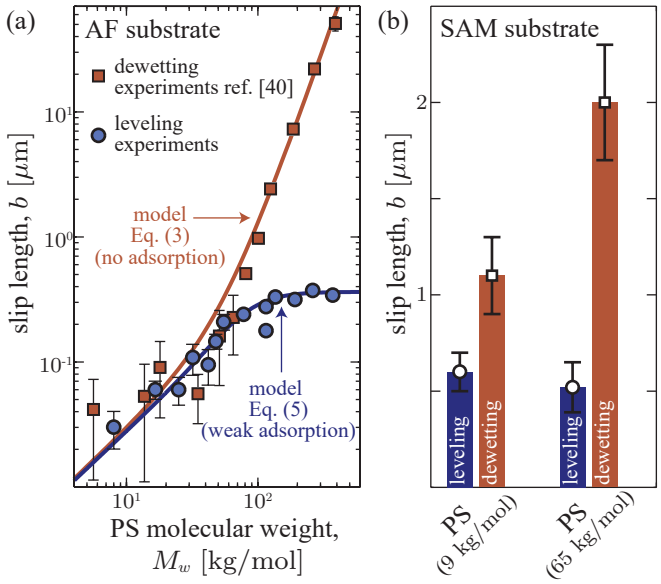

Figure 3.2: (a) Molecular-weight dependence of the slip length from stepped-film leveling films (blue) and dewetting films (data from Ref. [41]) for samples on AF2400. (b) Verification of the slip length disparity for two molecular weights on a mixed OTS-DTS SAM (see Section 3.3.1). Reproduced from Ref. [141].

be induced only by the substrate-polymer interaction, as this was the only change in the experiment. Furthermore, we see that for the lower molecular weight of part (b), the self-similar calibration profiles on Si are different from those on the AF2400 substrate, yet this difference is less significant than for the higher-molecular-weight sample in part (c). Therefore, the substrate effect is stronger for higher molecular weight polymers.

Quantitatively, the analysis of such data sets proceeds as follows: first, the no-slip calibration sample on Si is used to determine the stretch parameter γ/η in front of the spatial derivitaves of Eq. 2.1 and as described in the corresponding Section 2.2. This parameter is then fixed for the analysis of the slipping profile. With $h_0 = h_1 + h_2/2$ measured in the experiment, a library of numerical integrations of Eq. 3.2 was prepared for a number of b/h_0, this being the only remaining dimensionless parameter. Fitting for b/h_0 in this way allows to determine the slip length under several experimental conditions. In Ref. [141], it was found that the slip length was independent of the levelling film geometry (*e.g.* leveling cylindrical holes, stepped perturbations with $h_2 \ll h_1$), and independent of the temperature on the range $120 \leqslant T \leqslant 160$ °C.

In Figure 3.2(a) is shown the molecular-weight dependence of the slip length, b, for leveling stepped films, in blue. A monotonic increase of this slip length with a high-molecular weight plateau is observed. For comparison, slip lengths from the dewetting films of Bäumchen *et al.* [41] are shown in red. A huge disparity, up to two orders of magnitude, between the molecular weight dependence of the slip length is seen between leveling and dewetting experiments is noted for the AF substrates, and confirmed for two test cases on mixed OTS/DTS SAMs in Figure 3.2(b).

Therefore, in the approach to equilibrium, the dynamical path is distinct for the leveling and dewetting processes[2], as revealed by the disparities in the interfacial length scale. The expected chain-length dependence of slip lengths for ideal substrates [3, 48] was discussed in Section 1.1.2, following the molecular chain-length dependence of the polymer viscosity through $b = \eta/\kappa \sim N^\alpha$, with the exponent α being 1 for $N < N_\mathrm{e}$ and 3 for $N > N_\mathrm{e}$. In Ref. [41], and as shown in Figure 3.2(a), this latter chain-length dependence was verified for dewetting, and the substrates can thus be considered as ideal for such experiments.

The disparity of slip lengths between dewetting and leveling experiments was justified by considering the possibility of transiently adsorbed chains on these previously-assumed ideal substrates. Borrowing ideas from the models by Brochard and de Gennes [38, 148] and experiments of Léger [40, 149, 150] for permanently grafted chains, we assumed that adsorbed chains could play the same role as grafted ones from a frictional standpoint. The principal mechanism for the enhanced friction of adsorbed chains is interpenetration of these latter into the melt. Indeed, for such a case, the frictional stress associated to the solid-solid stress of Eq. 1.7 can be written as [148] $\sigma_\mathrm{sl} = (\kappa + \nu a_\mathrm{m} \frac{N}{N_\mathrm{e}} \eta) v_x$ where ν is the density of grafted or adsorbed chains. Equating this stress with the liquid-liquid one of Eq. 1.7 gives

$$b_\mathrm{ads} = \frac{b_\mathrm{ideal}}{1 + b_\mathrm{ideal}/b_*} \ , \tag{3.3}$$

where the presence of b_ideal in the denominator results from the fact that the adsorbed-chain, solid-liquid stress is proportional to the melt viscosity, while this is not the case for the ideal-slip stress balance. This viscosity dependence of the adsorbed-chain stress is the essential condition to give a plateau at high molecular weights. In the context of the Brochard model [148], we noted that $b_* \sim a_\mathrm{m} N_\mathrm{e} \approx 10^2$ nm is independent of the chain length.

In order to rationalise the disparity in slip lengths for the two different experiments, we considered the typical dissipations involved in an activated scenario. Herein, transiently adsorbed chains could be removed from the substrate if the typical dissipation due to shear stresses is larger than kT. Estimating the shear stress gradients from the AFM-measured curvature profiles using $\partial_x p \approx \gamma \Delta(\partial_x^2 h)/\Delta x$, we found that dewetting substrate dissipations are up to two orders of magnitude larger than those in the leveling experiments for the conditions typically measured. Furthermore, these dissipations, $\mathcal{P}_\mathrm{diss}$, straddled the kT boundary, that is $\mathcal{P}_\mathrm{diss,dewet} \approx 10^1 kT$ and $\mathcal{P}_\mathrm{diss,level} \approx 10^{-1} kT$. These considerations are similar to the ones presented by Hénot and coworkers [151,152] for slip in microscale systems wherein adsorption was controlled either with temperature or time.

Our message was therefore that even for nanoscale systems, there is no single slip length but that the typical interfacial stresses should be considered when attempting to predict the boundary condition for such confined, complex fluid systems. This message was echoed in more recent works of the Charlaix group [153,154] wherein viscoelastic polymer solutions were employed and a single slip length was not adequate to describe the ensemble of their data.

[2]Dewetting nevertheless takes place after an inevitable nucleation event. Despite the care in preparation of the films, some impurity is always present and can nucleate a hole even in a film of some hundreds of nanometers thickness.

To close this section, we note finally that the equilibration pathway is indeed dependent on the mobility of the polymer liquids at the surface. On a larger lateral scale than the few microns that are accessed in typical leveling or dewetting experiments, we note that the droplets left behind in a dewetting rim are not randomly distributed, but are left behind in a pattern that depends strongly on the slip length. This idea was mentioned briefly in Ref. [42], and was furthermore explained in detail in the Jacobs group in Refs. [155, 156].

3.2 Morphology is induced by interfacially-mediated dynamics

Having described two thin-film pathways toward equilibrium, we now move to discuss how morphology of an equilibrating polymeric liquid domain can be used to identify specific boundary mobilities. In the first section we focus on the liquid-air interface as investigated using stepped-film leveling, and in the second section we come to the equilibrating droplets that are illustrated in Figure 2.3(c) and (d).

3.2.1 Free-interface: thin-film evolution below the glass transition

In the previous section, it was shown that a change in the mobility term of the thin film equation could engender faster dynamics and a modification to the self-similar height profile. Even while the shapes of the self-similar profiles could be distinguished, it was seen that the modifications to the self-similar profile manifested mainly in a broader shape. In this section, we show how a detailed examination of the self-similar shapes of the height profile measured above and below the glass transition could reveal the dominant mobility mechanism of the film. Whereas well below the glass transition the whole film is glassy and does not flow, as in the top of Figure 3.3A, on approaching the transition from below a flow is confined to the interface (left of the figure) and on crossing T_g, the whole film flows (right) as described by Eq. 2.1. This work is the subject of Ref. [157] and details can be found there.

Since the 1990's [158], a large body of work reviewed in Ref. [28, 29] focussed on the glass transition of thin polymer films. In macroscale systems, the glass transition can be measured using thermodynamic measurements of the heat capacity or of the volumetric expansion coefficient, for example [25]. In Keddie's foundational work [158], the volumetric expansion of a thin film was measured using ellipsometry, wherein it was shown that T_g depends on the film thickness. These glass transitions were thus considered anomalous since the expansion coefficient is supposed to be a thermodynamic quantitiy and thus not dependent on the system size. However, it is also known that T_g is kinetically sensitive, that even a pseudo-thermodynamic measurement such as the expansion coefficient depends on the rate at which the sample is cooled from the liquid state, for example. Such kinetic considerations provided a hint: if the free surface of a polymer film provides an enhanced mobility as for the surface diffusion of metals [159], this layer's T_g could be reduced and the measurement of the expansion coefficient of a whole film may couple the surface and bulk glass transitions. Such an argumentation could partly explain the anomalously low

T_g seen as film thicknesses become smaller than about 50 nm for supported films. The importance of these free surfaces were addressed in particular in Refs. [160,161].

In Ref. [157], two series of experiments were carried out to demonstrate a connection between surface mobility and the glass transition anomaly. First, a series of PS stepped films with molecular weight 3.0 kg/mol and with geometry $h_1 = h_2$ (*cf.* Figure 2.5(a)) were prepared. These were then annealed at different temperatures above and below T_g for various times and their height profiles measured. As in the original stepped film work [96], a profile width, w was defined as the horizontal distance traversed over the step height, h_2, as illustrated in the right of Figure 3.3A; this width akin to that of a diffusing front, for example. The dynamics for $w(t)$ (not shown here) demonstrate a power law in $t^{1/4}$ regardless of the temperature, strongly suggesting a capillary driven flow as in the Eq. 2.1. While we will not detail this aspect here, we note also that the mobility of the leveling samples below T_g is much higher than would be predicted from extrapolation of the VFT law, this latter strictly applicable above the glass transition. This is rather typical for sub-T_g dynamics, and makes a fascinating research topic in its own right as reviewed elsewhere [28, 29].

In order to modify Eq. 2.1 to include a purely surface mobile domain as described in the previous paragraph, we considered the case of a liquid flow confined to a surface region of height h_m, independent of the position. This presents a marked difference to the classical lubrication theory, Eq. 2.1, since the mobility there is strongly height dependent. For the sub-T_g case considered, this simplifies significantly the governing equation since the nonlinearity is completely eliminated due to the constant flow-domain thickness, the capillary driving pressure being unmodified. Therefore, the glassy thin film equation (GTFE) is given by

$$\partial_t h + \frac{h_m^3 \gamma}{3\eta} \partial_x^4 h = 0 \qquad ; \qquad \text{glassy interior, fluid surface} \,, \tag{3.4}$$

which is mathematically identical to the linearized version of Eq. 2.1. Such a linear lubrication problem can be analytically solved, as described in Ref. [104]. The linearised case of Eq. 2.1 is applicable when $h_2 \ll h_1$ and thus when the flow-domain

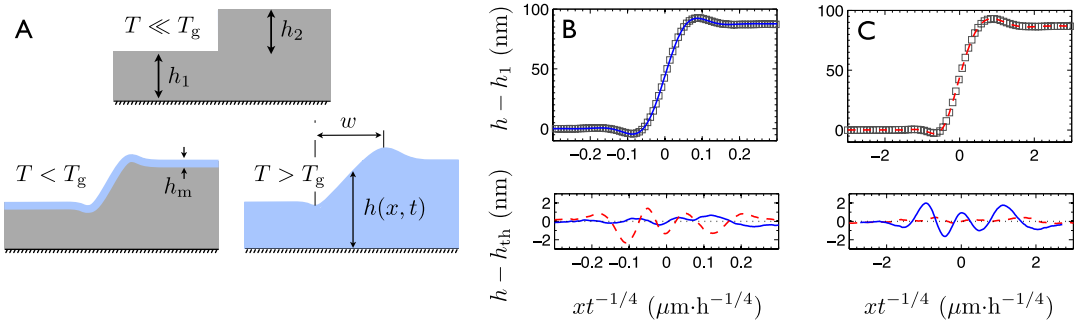

Figure 3.3: A. Schematics of the different temperature regimes for stepped film leveling. B. Self-similar profile of a stepped film leveling below T_g and with $h_1 \approx h_2$, with the red dashed and solid blue lines in the lower panel showing deviations of the height profile, h, from theoretical predictions, h_{th}, based on resolutions of Eqs. 2.1 and 3.4. C. Similar to B but for a film leveling above T_g. Reproduced from Ref. [157].

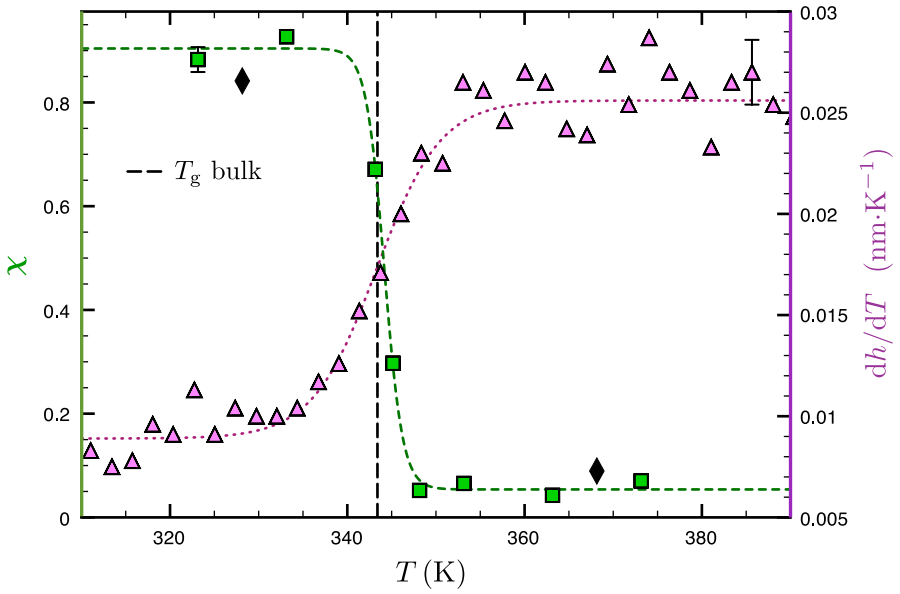

Figure 3.4: A. Schematics of the different temperature regimes for stepped film leveling. B. Self-similar profile of a stepped film leveling below T_g and with $h_1 \approx h_2$, with the red dashed and solid blue lines in the lower panel showing deviations of the height profile, h, from theoretical predictions, h_{th}, based on resolutions of Eqs. 2.1 and 3.4. C. Similar to B but for a film leveling above T_g. Reproduced from Ref. [157].

thickness is almost constant. The mathematical solution to this linear problem gives antisymmetric profiles, when considered around the center point at $h = h_1 + h_2/2$, and in contrast to the solutions to Eq. 2.1, there is only a single self-similar profile since the prefactor in front of the spatial derivative in Eq. 3.4 is absorbed into the time. This aforementioned symmetry is not observed for general profiles above T_g as observed in Figure. 2.7(a); the sample with small h_1/h_2 is far more asymmetric than the corresponding profile in part (b) with $h_1 \gg h_2$.

Considering the self-similar height profiles in Figure 3.3B and C, the former annealed below T_g and the latter above, corresponding numerical integrations were made; the fits are shown with solid blue (Eq. 3.4) and dashed red (Eq. 2.1) lines. In the lower panels are shown the deviations between the experimental data h, and the theoretical prediction h_{exp} for both models. Thus, below T_g the model incorporating a constant-thickness flow domain is appropriate, indicative of a thin mobile layer atop a glassy base, while above the expected lubrication model with full-film flow captures the data.

As the data presented in Figure 3.3B and C represents only two temperatures, a full temperature sweep was made going through the glass transition with films of constant geometry. In order to characterise the profiles with a single parameter, we defined a morphological correlation function, $\chi(T)$, as the integrated difference between a given experimental profile, h_{exp} and the fully-liquid lubrication model h_{tfe}, normalised by the integrated difference between the theoretical predictions for the

glassy-film flow, $h_{\rm gtfe}$, and the fully liquid one $h_{\rm tfe}$. Specifically, we have

$$\chi(T) = \frac{\int dx (h_{\rm exp} - h_{\rm tfe})}{\int dx (h_{\rm gtfe} - h_{\rm tfe})} \ . \tag{3.5}$$

Defined as such, a film obeying Eq. 3.4 has $\chi = 1$ and a film obeying Eq. 2.1 has $\chi = 0$. The temperature dependence of this function is illustrated by the errors (lower panels) in Figure 3.3B and C, where the typical error magnitudes are complementary in the two panels.

In Figure 3.4 is shown $\chi(T)$ for PS(3k) films over a temperature range spanning the bulk $T_{\rm g}$ indicated with a vertical, dashed black line. Remarkably, χ transitions there from a glassy-like value of nearly 1 to a fully liquid value of nearly 0, over a range of a few Kelvin. For comparison, the temperature dependence of the uni-axial, thermal expansion coefficient is shown for an 87 nm thick film of the same polymer as measured using ellipsometry. The sharp transition between χ suggesting surface-flow to χ indicating full-film flow is reasonably well overlapped with the pseudo-thermodynamic measurement of the thermal expansion coefficient. To demonstrate the robustness of the χ measure, the black diamonds show data for a single film, first annealed below $T_{\rm g}$ at *ca.* 327 K, and then annealed above at *ca.* 367 K. Remarkably, the value of χ for this experiment switches from a glassy-like value to a liquid-like one, further confirming the proposed mobility scenario of Figure 3.3A. This thus makes a connection between the surface-dominated dynamics below $T_{\rm g}$ for the leveling experiments, and the supposed free-surface importance in the wider glass transition literature.

We end this section by insisting slightly on the morphological selection of the films above and below the glass transition. To this end, samples were prepared with a geometry $h_1 \ll h_2$, for which we recall in Figure 2.7(a) showed a starkly asymmetric profile. In the left of Figure 3.5 is shown the self-similar leveling profile of such a geometry above $T_{\rm g}$, and the right shows an identical film, but annealed below $T_{\rm g}$ (see

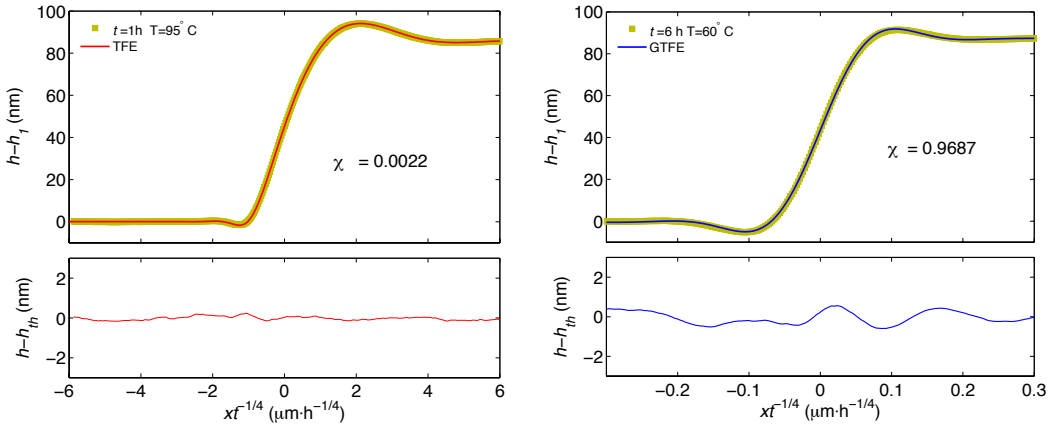

Figure 3.5: [left] Self-similar profile of a stepped film leveling above $T_{\rm g} = 70 \pm 3$ °C (see legend) and with $\{h_1, h_2\} = \{23, 90\}$ nm. The solid line is a fit to the TFE, Eq. 2.1. [right] A film with identical geometry yet annealed below $T_{\rm g}$ and fit using the integration of the GTFE Eq. 3.4. Reproduced from Ref. [157].

figure legends). The shape of the two curves is drastically changed on passing through the glass transition, thus proving furthermore the sensitivity of stepped-film leveling to different mobility mechanisms, the corresponding fits to Eq. 3.4 and Eq. 2.1 indeed show good agreement with the data. The insets to these panels also indicate the values of χ, showing the appropriateness of the chosen models. In the next section we show how slip at the lower interface can drastically modify the morphology of dewetting polymer microdroplets.

3.2.2 Buried interface: dewetting polymer microdroplets

In this section we consider, instead of the free, air-liquid interface of the previous section, the solid-liquid boundary condition and its effects on the free-surface morphology of dewetting sessile droplets. This work is detailed in Ref. [43] with a follow-up study, mainly numerical, in Ref. [162]. While the main focus here is on morphology, we will also comment on the dynamics as they present, at first, a common early-time dynamic and a final equilibration depending on the slip length.

When a sessile droplet is deposited onto a surface, it is generally out of equilibrium in the sense that its contact angle is rarely the one prescribed by Young. This could be the case for example in an ink-jetting process, or if a droplet lands on a completely wetting surface with zero contact angle. In this latter wetting case, the droplet spreads according to Tanner's law [31, 117, 163], combining the Cox-Voinov law for contact line dynamics [164–166], and volume conservation to derive a power law dynamic for the contact line radius [3]following $R(t) \sim t^{1/10}$. The prefactor of this power law, and also the Cox-Voinov expression, contains a logarithmic expression for the ratio of microscopic to macroscopic length scales of the fluid domain. Introducing these length scales is physically relevant since the hydrodynamic models are only relevant between, at least, molecular scale and at most to the fluid domain size. Critically, however, and as pointed out by Huh and Scriven [167], *not* introducing a microscopic scale would lead to a divergence in the predicted dissipation; "not even Herakles could sink a solid if the physical model were entirely valid, which it is not" they remarked. However, at small scales for complete wetting there is always a precursor film [117, 168–171] which can regularise the dissipation; in partial wetting cases, however such a precursor may not be present (especially for hydrophobic films), yet slip can also regularise the dissipation [166, 172–174].

While the slip length is often introduced as the microscopic length scale of a logarithmic correction, it is not always the case the the slip length and system size are so different (as in *e.g.* Section 3.1). Borrowing from the typical Tanner's configuration, we thus used the fabrication procedure of Figure 2.3(c) and (d) to prepare sessile droplets of PS(10k) with an initial contact angle of *ca.* 10° on OTS and DTS SAMs. Since the receding contact angle of PS on such substrates is $62 \pm 3^\circ$ (Supporting Information of Ref. [43]), an approach to equilibrium engendering hydrodynamic flow can be observed above the glass transition.

[3]We note another collision in the notation, where here R is the contact line radius and not the polymer's end-to-end distance. For our purposes in this section, the polymeric nature of the liquid serves only to set the viscosity and so the chain size, only a few nanometers [13], is negligible in front of the other length scales.

In Figure 3.6A are shown 3D renderings of AFM data sets for sessile droplets of PS(10k) dewetting from OTS (top, red substrate) and DTS (bottom, blue substrate). Corresponding sequences of radially-symmetric dewetting profiles, $h(r,t)$, are shown in part B and C of the same figure, the grey profiles indicate the data sets shown in A. As for the case of leveling stepped films with or without slip of Section 3.1, we remark that the change in substrate provokes a change in the dynamics toward equilibrium.

Overall, for the droplet on OTS, the equilibration takes roughly 360 min while that on DTS takes just 100 min. This modification of the dynamics occurs despite the chemical similarity between OTS and DTS as revealed by their similar surface energy (Section 2.1.1), and the similar receding contact angle at steady state as noted in the previous paragraph. Therefore, with the energetics and viscosity of the droplet-substrate pairs nearly equivalent, the change in substrate provokes a variation of the slip boundary condition. This observation is consistent with previous work of the Jacobs group [39,42,77,118], showing an order of magnitude change in the slip length between the two substrates for the hole-growth dewetting described in Section 2.3, and as verified for the substrates used in this study. Indeed, these considerations informed the choice of substrate for the droplet dewetting study. The question of slip disparity on such chemically similar substrates is addressed in the next section.

In the first instances of the droplet's retraction, with the contact line at $r = R(t)$, fluid builds up in a zone nearer to the center of the droplet. This initial contact line displacement scales as a power law in time with $R_0 - R \sim t^\alpha$, where $\alpha \approx 0.5$ is independent of the substrate, with a slip-dependent prefactor. Examining the final approach to equilibrium, we noted an exponential relaxation toward the final radius $R - R_\infty \sim \exp(-t/\tau)$, with the relaxation time dependent on the ratio of slip length to droplet size. Both of these temporal scalings could be rationalised with scaling arguments on the basis of viscous dissipation power balancing capillary driving power. For the early-time power law, recourse to the intermediate slip regime (*i.e.* when $bh^2 \gg h^3$ in Eq. 3.1) of the lubrication model was needed, in particular exploiting a

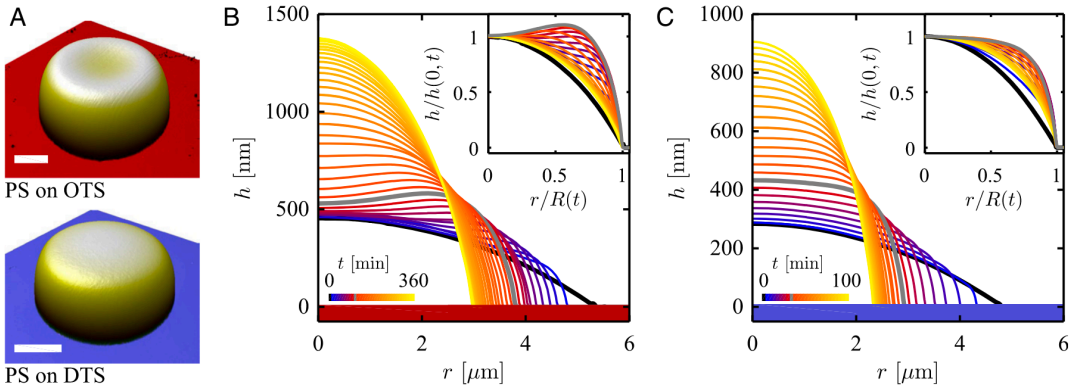

Figure 3.6: A. AFM measurements of microdroplets dewetting from the OTS and DTS SAMs; scale bars are 2 μm. B and C. Sequences of radially-symmetric height profiles for the droplets in A (*cf.* gray profiles) and for the times indicated. Insets show scaled profiles. Reproduced from Ref. [43].

self-similarity of the profiles in the contact line region that was observed experimentally. Furthermore, the slip length dependence of τ has two major asymptotes. The first is a Tanner-like one with $\tau \sim \ln R_0/b$ for vanishing slip lengths. Such a logarithmic dependence crosses over, however to a slip-independent time scale, $\tau \sim \eta R_\infty/\gamma$, reminiscent of suspended droplets relaxing in free space, yet with a contact-angle dependence that is left off here. For details, the reader is referred to Ref. [43].

In addition to the change of dynamics, we note also a remarkable change in the morphology of the dewetting droplets. On the OTS substrate, there is a pronounced local maxima off the $r = 0$ symmetry point, while such a local maxima does not arise in the droplet retracting from the high-slip substrate.

Overall the observations of the last two paragraphs are the main experimental phenomenologies taken from the droplet equilibration sequence of Figure 3.6. To understand these experimental observations, we considered the Stokes equation with a constant Navier slip condition at the substrate $v_r = b\partial_z v$. At the air-liquid interface, Laplace pressure was considered. Stress balance at the air liquid interface is given by $2\eta\partial_n v - p = 2\gamma\mathcal{C}$ where ∂_n denotes the derivative normal to the interface and $\mathcal{C}$ is the interface mean curvature, *i.e.* $2\mathcal{C}$ is the sum of the principal curvatures. Lastly, we included a boundary condition at the contact line radius R imposing the Young angle for all times $t > 0$. We refer to the collection of these ingredients as the Navier-Young model (NYM).

Numerical integrations of the NYM were performed using the boundary element method (BEM) [175]; time was non-dimensionalised by $\gamma/\eta R_0$ and space by R_0. In essence, this method takes advantage of the mathematical structure of the Stokes flow equations to enable a direct calculation of the interface profiles without computing the entire flow field. As only the boundary stresses are necessary, the dimensionality of the computation is effectively reduced by 1, offering a computational advantage; practically, furthermore, we only measure the interface profile. For certain instances the flow field in the entire flow domain can be calculated directly from the boundary

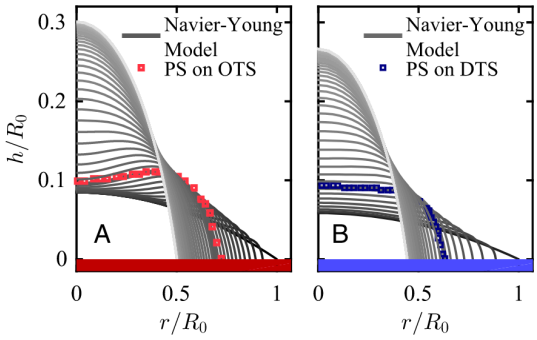

Figure 3.7: A. BEM resolutions of the Navier-Young model for a dewetting microdroplet with slip length $b/R_0 = 0.03$ and dimensionless times from 0 to 14.5. B. BEM resolutions of the Navier-Young model for a dewetting microdroplet with slip length $b/R_0 = 0.47$ and dimensionless times from 0 to 5.2. The grey highlighted experimentals profile from Figure 3.7B and C are shown for comparison. Reproduced from Ref. [43]

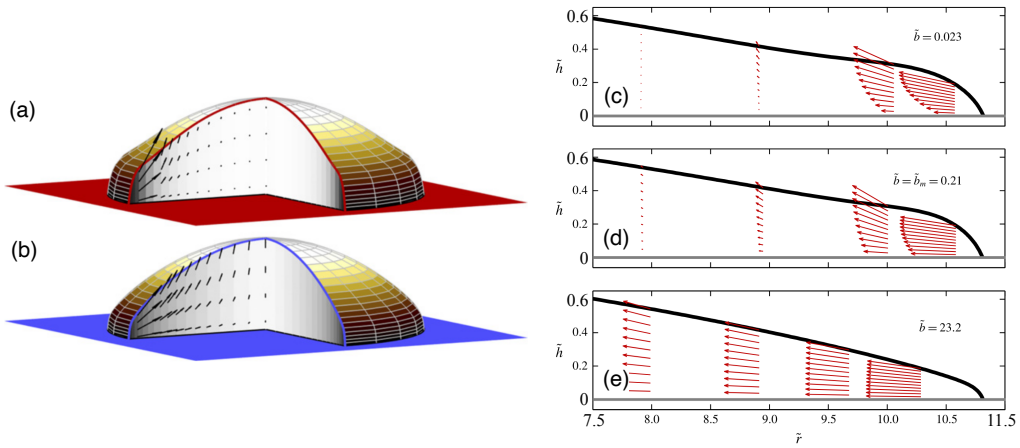

Figure 3.8: (a) and (b) Flow field illustrations from the NYM for the droplets of Figure 3.7. Reproduced from Ref. [43]. (c)–(e) Similar to (a) and (b) but for the dimensionless slip lengths $\tilde{b} = b/h_0$ with h_0 the central height of the droplet at $t = 0$ and for droplets with the contact line at $\tilde{r} = r/h_0 = 11.5$ at in the initial spherical cap state. Reproduced from Ref. [162]

stresses.

In Figure 3.7 are shown sequences of interface profiles, as obtained from the NYM, for two droplets with identical geometry to those in Figure 3.6. Slip lengths were chosen to be commensurate with those measured from dewetting films on OTS and DTS, and the equations were integrated until the droplet profiles reached a steady shape. For comparison, the experimental height profiles corresponding to the 3D renderings of Figure 3.6A are also shown, and correspond well to the computed profiles. The agreement between the experiment and the computations suggests that dewetting sessile droplets provide an alternative method of measuring a slip length of polymer melts on hydrophobic substrates. Besides the practical benefit of providing a slip length measurement, we also use the numerical integrations and analysis of the hydrodynamics to provide insight on the effect of slip of the flow structure within the droplets. Ultimately, this flow structure gives rise to the global shape evolution as indicated by the presence, or not, or a local maxima located between the contact line and axis of symmetry.

In Figure 3.8 is shown a series of flow fields as computed from the NYM. In (a), (b) are shown the droplets of Figure 3.7, while independent droplets with various dimensionless slip lengths are shown in parts (c)–(e). Generally, it can be remarked that in increasing the slip length, the more the flow penetrates toward the center of the droplet. With this flow structure, the redistribution of material toward the center thus prevents large-slip droplets from developing a ridge. Interestingly, however, a vanishing slip can also lead to the absence of a characteristic, non-central maxima. To see how this may be so, we can imagine the case for which after some motion on a non-slipping substrate, the contact line was pinned suddenly. In this pinned case the fluid already accumulated in a zone near the displaced contact line would relax toward the center of the droplet, for small contact angles according to Eq. 2.1, in order to

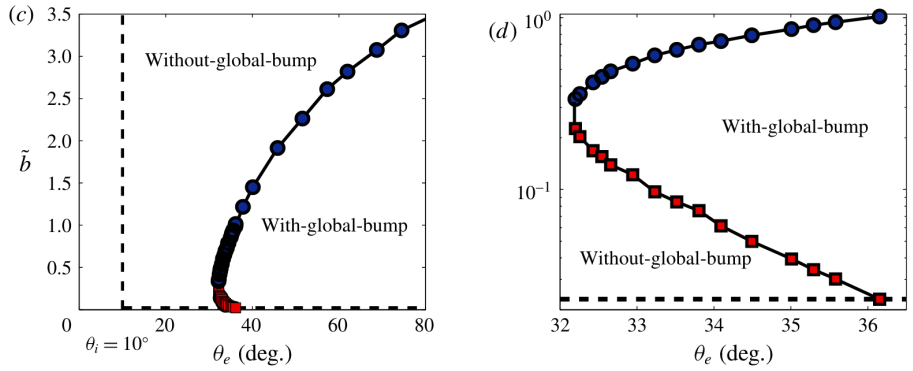

Figure 3.9: Morphological phase diagram for the presence, or not, of a non-central interface profile maxima, and for an initial contact angle of 10°. On the vertical axis, the dimensionless slip length and on the horizontal the equilibrium contact angle. The right side shows a zoom of the left. Reproduced from Ref. [162]

recover a quasistatic spherical cap shape. It happens that if the contact line moves slowly enough, the redistribution is faster than contact line motion. In Figure 3.9, we thus show a morphological phase diagram for which we map the presence or not of a "global bump" (*i.e.* a non-central maxima), as it depends on the equilibrium contact angle, and slip length, and for a constant initial contact angle. For a large enough θ_e, there is always a finite region giving the presence of a non-central maxima, which may help to provide a "visual" indication of the slip regime.

In the previous two subsections, we have thus emphasised the role of interface mobility on the morphology of free-surface, nanoscale flow domains. In the first case, free-surface mobility was able to be elucidated by an examination of the stepped-film leveling method, providing a direct observation for free-surface flow typically confined in the first few nanometers of an otherwise glassy film. In the second, we found that friction at the buried, solid-liquid interface, as typified by the slip length, could have a large impact on the morphology of dewetting microdroplets, and indicative of the extent over which fluid may be mobile in the context of nanoscale flow domains subject to contact line motion.

3.3 Slip is mediated by molecular structure at the solid-liquid interface

In the preceding section, we saw how the choice of substrate could inform the slip hydrodynamic boundary condition, even for an identical liquid and very similar interface energetics. In this section, we review work whose aim was to provide insight as to how these seemingly "identical" substrates could give rise to such an order of magnitude change in the interfacial friction. Indeed, as the liquid is identical, we suppose that the interfacial friction coefficient is modified on a change in the substrate. This section is closed with a discussion concerning the interactions of polymer chains with their interfacial counterparts, either a solid or a vapour. We demonstrate how, for an

identical dewetting substrate, the annealing history of a polymer film and the choice of annealing interface can inform the boundary condition. This interface-mediated slip section gives onto the following chapter wherein semidilute polymer solutions are investigated using TIRFM for assessment of the hydrodynamic boundary condition.

3.3.1 Mixed monolayers promote enhanced sliip

The self-assembled monolayer substrates providing disparate slip conditions of the preceding section differ by only a few atoms. Specifically, the difference between OTS and DTS is "just"[4] a 6-mer of fully-hydrogenated carbon. In Ref. [176], we hypothesised that preparing a smooth transition between pure OTS and pure DTS could give clues as to the molecular origin of the disparity. These mixed SAMs are schematically illustrated in the left column of Figure 3.10.

A series of monolayers was prepared containing a mixture of OTS and DTS, according to the procedure outlined in Section 2.1.1 and detailed in Ref. [74]. Polymer films with thickness *ca.* 160 nm were floated onto such wafers and hole-growth dewetting was examined. In the central column of Figure 3.10 are shown pairs of images for dewetting from each of the three substrates. The initial image (*i*) is taken for a hole of constant radius, and the later one (*ii*) is taken 18 min later. Remarkably, over this time interval, the hole on the mixed SAM with 50% DTS displays the largest change in hole radius. Dewetting is faster on mixed SAMs than on pure OTS or DTS ones, as verified also by a detailed examination of the hole growth kinetics provided in the article [176]. To control that the surface energetics is not responsible, we also measured the contact angles of PS on each of the SAMs and found that for the mixed monolayers there was a small *decrease* of a few degrees in the steady, receding contact angle. If the energetics were dominating the dynamics, this small modification would cause the holes to grow *more slowly* [117].

Thus, if it is not the driving force that is responsible for altered hole growth kinetics on mixed-OTS/DTS SAMs, the slip boundary condition should be responsible. In the right column of Figure 3.10, part (a) therefore, are shown dewetting rim profiles for each of the SAM compositions studied. There it is seen that the OTS rim displays a characteristic dip that is associated with weaker slip as compared to a film with a monotonic profile [39, 77, 121], see also Figures 2.11 and 2.12. The film dewetting from DTS has a slightly non-monotonic profile and the films on the mixed SAMs display monotonic profiles, and rim profiles with larger penetration into the undisturbed portion of the film. All of these observations, as in the previous section on dewetting microdroplets, suggest a maximum in the slip length for a mixed composition. Indeed, in part (b) of the right column in Figure 3.10 is shown the fitted slip lengths, showing a non-monotonic slip-length dependence on the composition. These observations were confirmed in multiple instances of monolayer preparation, with the general trend of observing an order of magnitude change in the slip length between OTS and DTS SAMs, and typically a factor of 5 or 6 between DTS and a 50/50 mix of OTS and DTS.

As for pure OTS or DTS SAMs, the mixed monolayers display under AFM an

[4] It is probably the naïvté of a polymer physicist speaking as, considering the N-large limit, 6 is small.

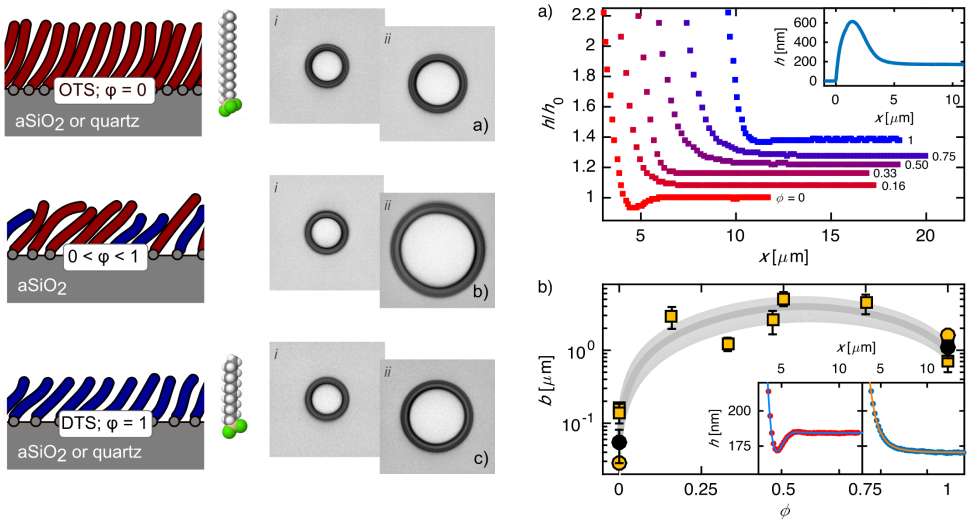

Figure 3.10: [Left column] Schematics of the self-assembled monolayers containing different fractions, ϕ, of DTS (blue), OTS are represented in red. [Center column] Optical micrographs of (*i*) dewetting holes with radius 4.9 μm and (*ii*) after a constant time of 18 min later. Dewetting was for 160 nm, PS(10k) films at 110 °C. [Right column] (a) Corresponding rim profiles as measured by AFM for different compositions ϕ of DTS in the SAM grafted to a Si wafer. The inset shows a full profile. (b) Slip lengths extracted from the rim profiles of (a) using Eq. 2.5; the insets show two fitted rim profiles. Reproduced from Ref. [176].

atomically smooth surface largely free of defects and with a topography similar to the one shown in Figure 2.2(a). As such, a deeper investigation using X-ray reflectivity on the bare substrates was made. While we do not show the raw data here, the derived electron density profiles are shown in Figure 3.11. We first remark that the OTS and DTS profiles and fitting parameters are similar to those measured previously [73,74]. To summarise the previous observations, the OTS and DTS layers make a full coverage of the substrates, with an electron density that approaches that of the crystalline structure of, for example, octadecane in the case of OTS. The OTS monolayers are slightly more packed that the DTS ones, with a chain density of approximately 5 nm^{-2} whereas DTS shows roughly 3.8 nm^{-2} chain coverage[5]. Given such coverage and the length of the chains, it was also noted [73] that, on average, a DTS chain makes an angle of *ca.* 30°, while OTS chains average a 5° inclination.

With respect to the mixed monolayers, we noted that fitting the profiles required the introduction of an extra tail layer (purple in Figure 3.11), which we interpret as the extra 6-mer of OTS that protrudes above the monolayer carpet of DTS. Such a hypothesis was confirmed using molecular dynamics simulations. For these, the yellow curve in the panel for $\phi = 0.5$ in Figure 3.11 shows good agreement with the measurements. In these simulations, it was noted that the terminal CH_3 groups of the DTS tails were always buried below those of the OTS tails. Such observations

[5]Such coverage calculations simply require to integrate the electron density of the head and tail layers, and then to divide by the known number of electrons in the corresponding molecules.

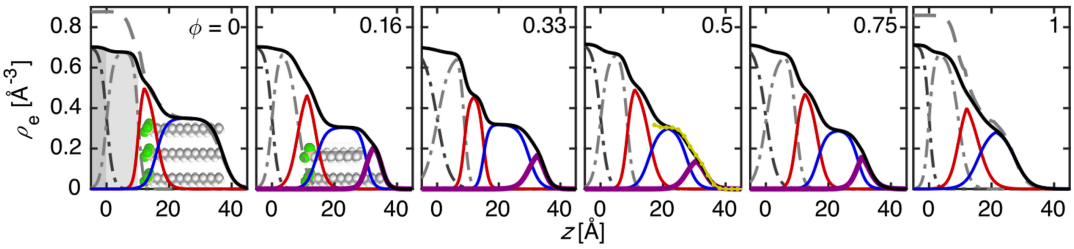

Figure 3.11: X-ray reflectivity-derived electron density profiles perpendicular to the air-SAM interface. From (a) to (e) is shown an increasing concentration of DTS molecules in the silanisation. Solid black lines indicate the full electron density, while also shown are the Si and SiO_x components (dashed-dot lines), head and tail groups (red and blue solid lines), along with protruding OTS 6-mers (purple lines). The yellow dotted line for $\phi = 0.5$ indicates the full electron density predicted from molecular dynamics simulations. Reproduced from Ref. [176].

motivated us to use the experimental protrusion layer (purple lines) to estimate the density of exposed SAM molecules, assuming that such a layer would correspond to the electrons of the protruding 6-mer of OTS in excess of DTS. We found that the mixed layers presented the smallest number of exposed chains (typically 2 or 3 nm^{-2}, see [176] for details).

While we cannot conclude based solely on these results as to the origin of the enhanced slippage on DTS and mixed SAMs as compared to OTS, there are perhaps some clues in the structural data offered by Figure 3.11. Here we suggest several possibilities. First, the average inclination angle being larger on DTS than on OTS suggests a higher exposure of intermediate CH_2 groups compared to the terminal CH_3 groups. Furthermore, it was observed in independent studies [177] that mixed monolayers may present an enhanced probability of gauche states for the grafted molecules. While these changes may be subtle, their effects on the solid-liquid friction could be important. Indeed, we remark that this possibility for atomic/molecular-scale friction modification is bolstered by the parallel observation that using P2VP instead of PS (*i.e.* a substitution of one nitrogen atom in P2VP for one carbon atom in the side-chain phenyl ring of PS), can also reduce the slip drastically on SAMs used here [178]. Thus, the electronic structure of the solid-liquid pair, including interfacial depletion [73, 178], seems to play a dominant role in solid-liquid friction; in the study presently described we made a modification of only the solid. On a more mechanical level, it is also known that elastomer friction depends strongly on the number of linker chains between a given surface and the sliding elastomer [179]. If the polymer melt is even transiently adhered to the substrate through the exposed chains, as in Section 3.1, the reduced number of load-bearing molecules could partially explain the slip disparities. Lastly, we note the possibility of dynamical effects. Although we have no direct evidence, it is possible that the more loosely packed monolayer chains present a higher mobility under shear from the polymer melt, which may manifest in a reduced activated friction.

The results of the previous paragraphs show that the fine molecular structure, even in the last few angstroms of a solid boundary, can produce the drastically de-

creased solid-liquid friction. In the next subsection, we turn to the effects of polymer film preparation protocols on the resulting solid-liquid friction.

3.3.2 Sacrificial mica, solid-liquid friction

In the previous subsection we described how molecular structure of the substrate, at the 'monomeric'[6] and perhaps at the electronic scale, could influence the slip hydrodynamic boundary condition for short-chained polymer melts. In this section we fix the substrate and investigate how changes in the thermal annealing protocol impact the solid-liquid boundary condition, in particular for entangled polymer melts.

As described in Section 1.1.1 and in Refs. [10,11,25], their equilibrium conformations in the melt are random walks. This random walking structure in turn plays a dominant role on the dynamical properties of polymer melts — to give just one example the so-called Rouse time is that taken for a short-chain polymer in the melt to diffuse a distance of order its own size, and scales as $\tau_{\mathrm{R}} \sim N^2$ in part due to the $N^{1/2}$ scaling for the chain size, the other factor of N coming from the inverse porportionality of the diffusion coefficient with N. Therefore, a change in the random-walking structure of a polymer chain typically provokes a dynamical consequence.

The Reiter and Steiner groups [145,146] investigated melt-relaxation phenomena in the context of spin-coated films. During spin coating, rapid solvent evaporation, a glass transition at finite solvent concentration, and evaporation of solvent down to zero concentration leave the chains in highly non-equilibrium configurations. Their works, only two are cited, suggested extremely long times, much longer than the reptation time, to achieve equilibration of the chains. In a complementary work [147], we used annealing on mica and the so-called crazing technique to investigate the equilibration dynamics of spin coated films. We found relaxation times of order the reptation time, yet our substrates, mica, differed from the Reiter and Steiner works, Si, as did the experimental protocol.

Besides spin coating, chains at an interface have perturbed configurations due to the so-called Silberberg principle [180], suggesting that chains at a wall are simply reflected back into the melt. Thus, the intermolecular chain packing is altered near an interface as 'intra'-chain interactions become more prevalent there. Since entanglement depends on packing as described by the Fetters models [13, 19] mentioned in Section 1.1.1, the entanglement density in thin polymer films and at interfaces remains an actively investigated subject [82, 181, 182]. Dynamical consequences of near-wall chain packing were investigated by several groups. In the context of the slip hydrodynamic boundary condition for dewetting films, Bäumchen *et al.* suggested that the slip length could be reduced [84] as compared to the prediction $b = \eta/\kappa$ using the bulk viscosity, following a work by Bodiguel and Fretigny [83] showing reduced viscosity for thin films dewetting from a liquid bath via global retraction. Meanwhile, Schune *et al.* [171] studied kinetics of precursor films of thickness on the order of one nanometer or less, *i.e.* with $h/R \ll 1$ here R denoting the chain size. Remarkably, they showed that bulk-entangled chains of partially-wetting melts could in fact be treated as 2D semi-dilute in a dynamical sense for such extreme confinements.

Although the Silberberg principle is a useful and reasonably predictive one, it

[6] Quotes are used since the substrate molecules in question are not really polymers

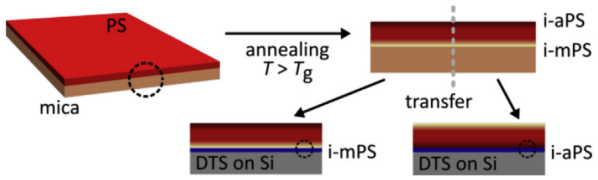

Figure 3.12: Schematic of sample preparation for the formation of interface-specific dewetting. The PS touching a DTS substrate for a dewetting experiment formerly touched either a mica surface (i-mPS) or air (i-aPS). Reproduced from Ref. [143].

is only valid for strictly non-interacting polymer-substrate pairs. Noting the difference between the Si and mica equilibration times, for example, in Ref. [143], we hypothesised that differences in polymer-chain interaction with air and that with the sacrificial mica could be long-lived enough to be observable in a dewetting film. To this end, we modified the floating technique described in Figure 2.3 to arrange for specific interfaces to touch the substrate from which *ca.* 200 nm films were dewetted. In Figure 3.12, we show this protocol, wherein the former PS-air interface (termed i-aPS) or the PS-mica interface (termed i-mPS) touches the dewetting substrate. For the purposes of comparison, films from the same mica substrates were systematically used, as indicated by the grey dashed line at the top-right of Figure 3.12.

In Figure 3.13 we present the main experimental observations of this work. For PS(465k) films that have not been annealed —dashed curves in part (a) at left— the rim profiles do not show any sensitivity to the interface touching DTS, whether i-aPS or i-mPS. Once annealed however, the same films show a dramatic difference in the relaxation to the undisturbed portion of the film when comparing i-aPS and i-mPS dewetting. Under the interpretation provided by Eq. 2.5, the annealed i-mPS interface presents a slip length that is reduced by almost an order of magnitude for the well entangled chains of this figure panel. The slip-disparity effect is thus chain-length dependent. In the right part of the figure, we see that the rim profiles —part (a)— for annealed films on mica become more different as the chain length increases; in part (b) the slip lengths obtained from Eq. 2.5 are shown and reveal a slip length disparity that grows with chain length, with a discernible offset arising between PS(10k) and PS(51k).

Further experiments not shown here using blends of PS(28k) and PS(465k) with varying compositions were also dewetted from AF2400. These experiments showed that blends with higher concentration of long chains displayed larger the slip disparity for annealed i-aPS and i-mPS films. We noted that the onset of the observable slip disparity corresponded with blends of number-averaged molar mass of roughly 50 kg/mol, consistent with the monodisperse samples; the corresponding weight-averaged molar mass was a factor 6 larger for these bidisperse blends. Practically, that the onset correspondence occurs for number-averaged molar mass may be suggestive of the mechanism for slip disparity between i-aPS and i-mPS dewetting films. Chain-end density, for example, is proportional to number-averaged molar mass while the viscosity correlates to the weight average; these are, however, just two examples.

While the molecular origin of the slip disparities displayed in Figure 3.13 was not determined in the context of the presently-described work, several mechanisms could

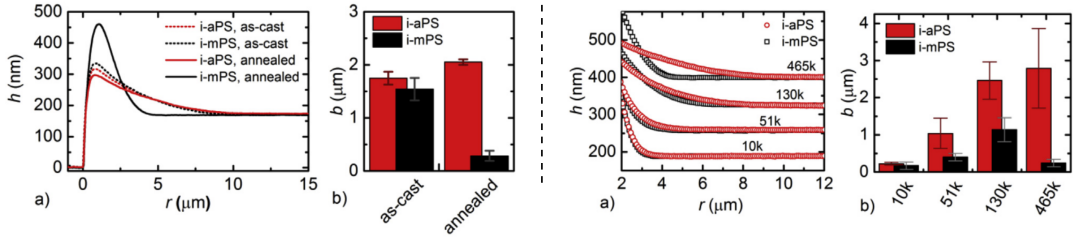

Figure 3.13: [Left] (a) Dewetting rim profiles for films with *ca.* 3μm holes. Dashed lines show as-cast films, and solid lines show annealed films, with red and black curves showing air and mica interfaces in contact with DTS for dewetting. (b) Slip lengths obtained from the rim profiles in part (a), from Eq. 2.5. [Right] (a) Rim profiles for annealed films of indicated molecular weight with i-aPS in red and i-mPS in black. (b) Associated slip lengths from Eq. 2.5. Reproduced from Ref. [143].

in fact be responsible. We recall these speculations here for the purposes of guiding possible future study. First, chain-end segregation is commonly known to occur as an equilibrium structural phenomenon, mainly as a result of the reduced entropic penalty [183] associated with chains at an interface as compared to having main-chain monomers there; effectively, reflecting a chain end does not change the polymer conformation. Neutron reflectivity notably contributed to this topic experimentally, and it was in particular shown by the Russell group [184–186] that air-PS and solid-PS interfaces could display markedly different chain-end segregation arrangements. Besides these chain-end or short-chain effects, interfaces also provoke modified chain ordering as revealed by the entanglement and dynamical studies mentioned above [82–84, 171, 181, 182]; entanglements do seem particularly relevant in the slip-disparity context as it is beyond N_e where the differences can be resolved in the dewetting experiments. Simulations [187, 188] revealed the possibility that densities in the first monomer layer could be as large as two times larger than in the bulk near a solid surface, with oscillatory density profiles and a with possible chain-packing modifications. A marked difference in the density profiles near an air interface that is not oscillatory, but monotonic was revealed in the same studies [187, 188]. The specific dynamical effect of these static packing and segregation phenomena, built from a molecular level description, is currently unknown, yet our results could help to frame such theoretical efforts.

To summarise the previous two subsections, we could note practically that evaluations of the hydrodynamic boundary condition must be done with care in any experiment or process manipulating polymeric liquids at the nanoscale. Fundamentally speaking, the physical hydrodynamic boundary condition can indeed vary over an order of magnitude, or more, even for superficially identical chemistries. Our observations point to the extreme sensitivity of hydrodynamic boundary conditions on the macromolecular level conformations as well as monomeric- and electronic-scale detail of the solid-liquid pair.

Chapter 4

Near-surface colloid transport for semi-dilute solution slippage and nanoscale Taylor dispersion

In the last chapter, we were uniquely concerned with polymer melts. Besides the work presented there, a fairly mature understanding of many of the main features controlling melt-polymer slip were established through the '90's and '00's, significantly from the Orsay groups [40,149,150,189–191] and others [192–194], stemming from the theoretical ideas of de Gennes and Brochard from the late '70's onward [3,38,48,117,148]. Meanwhile, an individual polymer molecule in dilute solution has been treated as a soft object in a hydrodynamic flow near a surface for some time, with a comprehensive review offered by Graham [195] as to the statistical nature of these objects' transport.

Bridging the gap between these two extremes in polymer concentration, slippage of semi-dilute solutions wherein there is considerable chain overlap but for which the solvent largely influences the small-scale structure and dynamics has been investigated to a much lesser extent. Much of the early work in this concentration regime was motivated by the process of enhanced oil recovery [196] and other industrial or fundamental processes [197]. More recent works have investigated polyelectrolyte slippage [153, 154] wherein the charges on polymer chains could promote depletion or absorption at a glass wall [150,197–204]. Such solutions display a highly non-Newtonian rheology, with in particular a strongly shear-thinning behaviour as described in Section 1.1.1 and in Refs. [20–24].

One of the main challenges in measuring slip for such polymer solutions is their relatively small slip lengths, as compared to polymer melts. Furthermore, the techniques used in the previous chapter are not applicable since the thin-film manipulations of Chapter 2 cannot be used for aqueous solutions. One technique developed in Orsay relying on photobleaching [189–191] a melt at room temperature and possible to use for polymer solutions is nevertheless only capable to resolve slip lengths down to one micrometer or more. Therefore this photobleaching technique is only applicable to entangled polymer solutions. Techniques based on force measurement such as colloidal probe AFM or surface forces apparatus, while well-developed from a theoretical standpoint, are nevertheless indirect. For these reasons we emply TIRFM in this

chapter for the investigation of semi-dilute unentangled polymer solution slippage.

As the near-wall structure and bulk rheology of semi-dilute solutions may be non-trivial, in the next section we describe how TIRFM particle tracking can be used to simultaneously measure the near-surface rheology and boundary condition of such flowing solutions; the work is detailed in Ref. [132] and makes up also part of the thesis of G. Guyard [135]. For reasons of continuity with the previous sections, we delay the description and motivation for the latter sections of this chapter, were we present work on near-surface particle transport, comprising diffusive and advective motions, in Newtonian liquids at the nanoscale.

4.1 Semidilute polyelectrolyte near-surface rheology and boundary conditions

In Section 2.4 we described the total internal reflection fluorescence microscope, showing in Figure 2.17(a) velocity profiles measured for 100-nm-diameter fluorescent nanoparticles in water at different imposed pressure across our standard microchannels. Similar profiles from an independent experiment with water are shown in Figure 4.1(a). Each of the profiles is linear as expected for the first micron of a 20 μm channel, where the velocity profile is essentially a simple shear. The shear rate, $\dot{\gamma}$, shown in Figure 2.17(b) varies linearly with the pressure for water, suggesting a Newtonian liquid of viscosity in good agreement with that of water at room temperature. The same is true for other Newtonian liquids, as shown in Figure 4.2(a), where the ratio of viscosities between water and glycerol-water mixtures is shown. To determine the viscosity of the solutions subject to TIRF measurements, we use the ratio of the stress and the measured shear rate, the former which is proportional to the applied pressure through a simple geometrical prefactor equal to $h/2L$. This result for Newtonian viscosities confirms the validity of the angle calibration we presented in the previous section, and suggests that investigating more exotic liquids is

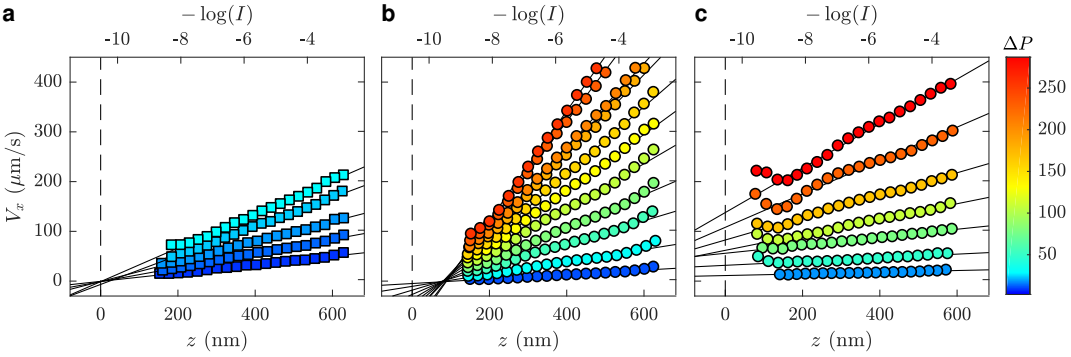

Figure 4.1: Velocity profiles measured by TIRFM velocimetry for 100-nm diameter particles in (a) water, (b) a solution of neutral poly(acrylamide) of molar mass 2 Mg/mol with a concentration of 2 mg/mL in water and (c) a solution of negatively charged poly(acrylamide) with molar mass 817 kg/mol and a concentration of 0.5 mg/mL. Reproduced from Ref. [132].

possible.

In Figure 4.1(b) we show velocity profiles measured using a semi-dilute solution of neutral poly(acryl-amide) (PAM) with molecular weight 2 Mg/mol at a concentration of 2 mg/mL. Similarly, velocity profiles were obtained for the negatively charged PAM of part (c), with molecular weight 817 kg/mol and a concentration of 0.5 mg/mL; such a concentration also gives rise to a semidilute solution. In contrast to the data in Figure 4.1(a) for pure water, we find that the shear rates derived from the (b) and (c) parts are not proportional to the imposed pressure. Such a nonlinear dependence on the pressure demonstrates that these polymer solutions are non-Newtonian. We therefore performed bulk rheology on all our solutions of Figure 4.1 in steady shear (MCR 302, Anton Paar), the water-normalised results being shown in Figure 4.2 as small dots.

Also shown in Figure 4.2 are the TIRFM-derived, water-normalised polymer viscosities. As can be seen in both parts (b) and (c), solutions of neutral and charged PAM are shear thinning if the concentration and shear rate is high enough, with a viscosity that decreases with the shear rate. The TIRF measurements are in quantitative agreement with bulk rheology for all of the concentrations measured and for both polymers, using the same solution in the microfluidic chip as in the rheometer.

Much lower concentrations than are displayed in Figure 4.2(b) were also measured by rheometry, with the characteristic linear dependence on concentration for low concentrations. Such measurements allowed for the measurement notably of the intrinsic viscosity, $[\eta] = \eta_w^{-1} d\eta/dc$, permitting to use the semi-empirical model of Jouenne and Levache [24] to fit simultaneously all data for all concentrations in panel (b) with a single fitting parameter, the relaxation time of a chain in dilute solution. These are shown with the black curves in the panel showing good agreement having taken the Zimm time [11] as 1.2 ± 0.1 ms, as is reasonable for a typically 60 nm coil size in solution for these polymers. The mutual agreement between the model, bulk

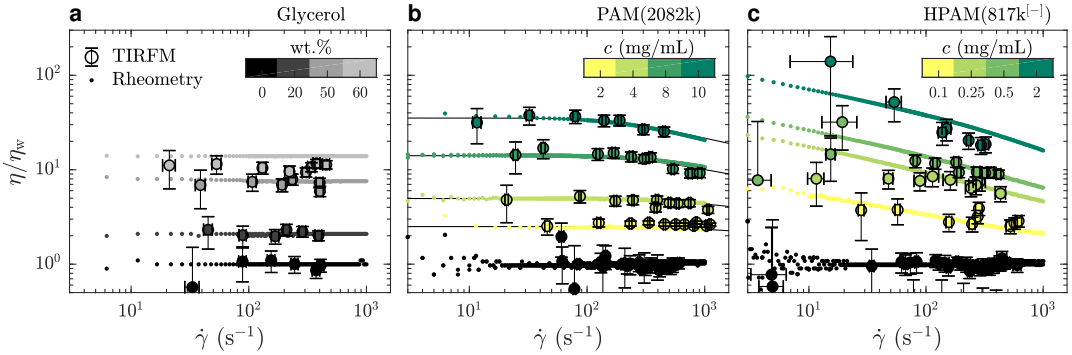

Figure 4.2: Comparison of rheology measurements performed by classical bulk rheology (smaller dots) and TIRF velocimetry (larger circles), all normalised by the viscosity measured in water in the same chip and in sequence: (a) glycerol water mixtures with increasing concentration $0 \leqslant \phi \leqslant 60$ vol% from bottom to top; (b) neutral PAM of 2000 kg/mol; (c) 10 % negatively charged PAM with molecular weight of 817 kg/mol. Colour bars show the concentration for each panel. Reproduced from Ref. [132].

rheometry and TIRFM measurements of panel (b) suggests that rheology in the zone where we see particles, roughly 100 nm to 1 μm from the surface, is bulk-like and can be assessed with fidelity.

Having discussed the rheology of polymer solutions as measured by TIRF, we turn our attention now to the measurement of the hydrodynamic boundary condition. Up to now, we have only considered the slopes shown in the data of Figure 4.1, yet the hydrodynamic boundary condition, as characterised by the intercept of the linear regression of the velocity profiles, represents the principal interest of using the TIRF to study polymer solutions: slip lengths down to a few tens of nanometres become accessible.

In Figure 4.1(a), wherein velocity profiles for water are shown as a function of the particle-wall distance, we also show a vertical dashed line indicating the solid-liquid boundary. Using the same microfluidic chip, we measured the velocity profiles of neutral PAM with molecular weight 2 Mg/mol in Figure 4.1(b). By comparing the common intersection point of the velocity profiles, here we focus on the top x-axis, it is clear that there is an offset in the intensity value at which the velocity profiles extrapolate to zero. We take this as evidence for the existence of an adsorbed layer of polymers, in this case with a thickness of approximately 100 nm. We have repeated such measurements for several concentrations of this 2 Mg/mol polymer, and complemented them with additional measurements for similar neutral PAM with molecular weight 1.28 Mg/mol, all show such an adsorbed layer consistent with the chain size.

Turning our attention to charged polymers, we consider the anionic HPAM, which have the same charge as both the wall and the particles. In Figure 4.1(c), it is clearly seen that the velocity profiles extrapolate to zero at a position well below the glass/water interface, thus there is an apparently positive slip length for such solutions. We have made similar measurements for several other concentrations and all show positive apparent slip, from a few hundred nanometres up to 2 μm, which depend on the concentration and on the pressure applied across the channel.

Since the polymers and wall are both negatively charged, it is expected that a depletion layer of order the correlation length [200,205] would be present, as schematically indicated in the inset of Figure 4.3. The lower layer near the wall is thus enriched with water, and the one in the microchannel a bulk solution of higher viscosity. We thus used [132] a simple two-layer model for the fluid, balancing the stress between the layers and a no-slip condition at the glass-water interface. This consideration allows the determination that the apparent slip length normalised by the correlation length, *i.e.* the depletion layer thickness, should scale linearly with the relative viscosity, $\eta/\eta_{\mathrm{w}} - 1$. This latter viscosity is dependent on the applied pressure across the channel, as measured directly from TIRFM as in Figure 4.2(c). Knowing the charge density on the polymer backbones, we thus used the Dobrynin theory of polyelectrolytes [15] to estimate ξ for each solution, the values varied from 62 nm to 14 nm for the smallest and largest concentrations, respectively. Therefore, in Figure 4.3(a), the normalised slip lengths are plotted as a function of the relative viscosity. The normalised data display a linear scaling over nearly three orders of magnitude in the dimensionless variables, validating the model and suggesting a depletion layer of order the correlation length as hypothesised.

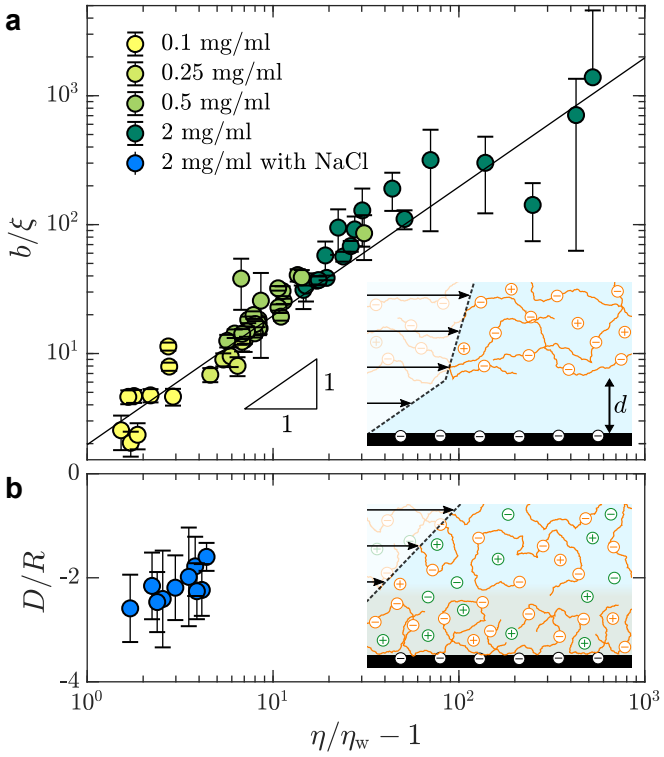

Figure 4.3: Comparison of slip length, b, measurements for a series of polymers with different molecular weights and electrolyte content. For each color grouping, the concentration increases from left to right. Reproduced from Ref. [132].

To test the hypothesis that the two-layer model in Figure 4.3(a) is electrostatically mediated, we performed a complementary set of experiments for which monovalent salt was added with a concentration chosen to screen all of the charges on the polymer backbones. With such a screening, it was expected that the neutral polymer case would be recovered, which is finally seen in Figure 4.3(b), where a 'negative' slip length indicating an adsorbed layer as in Figure 4.1(b) is observed. This layer is of order the estimated chain size in dilute solution, the semi-dilute scaling being a weak function of the concentration.

These experiments show that TIRFM is well-suited to investigate the interfacial dynamics of complex fluids. Indeed, the experiment allows to disentangle the essential ingredients of such interfacial phenomena: the boundary stress along with the interfacial extrapolation length, providing perspectives for the rich phenomenolgy of polymer-surface interactions in a dynamical setting.

4.2 Pre-asymptotic and nanoscale Taylor dispersion

In the last subsection, we investigated the particle motions' mean characteristics, allowing to describe the boundary conditions for semidilute polymer solutions and the corresponding boundary conditions. All of the velocimetry measurements derived from the average translation over a given time interval, typically 2.5 ms corresponding

to one frame of the 400 Hz videos. However, the statistics around these means also presents an opportunity to learn about the diffusive motion of particles near an interface. Here we will focus on Taylor dispersion as described in Section 1.1.3. There, we described the effect for tracer-like particles long after they have explored the entirety of a flow domain's cross section. By tracer particles, we mean purely non-interacting with the confining walls, and when we say 'before', we mean that times are shorter than the Taylor time, τ_z which we recall is proportional to h^2/D_0.

The flow domain common to both investigations is the near-surface region illuminated by an evanescent wave of a TIRFM. One interesting feature of such a setup is that the flow profile is essentially pure shear with velocity $v_x(z) = \dot{\gamma}z$. This profile is the simplest one can give rise to Taylor dispersion, and we thus recast the Peclet number as $\mathrm{Pe} = h^2\dot{\gamma}/D_0$, emphasising the feature of velocity gradients through the shear rate, having replaced U_0 with $\dot{\gamma}$ and dropping the factor 2. We will see that the altitude selectivity of Figure 2.18 was particularly useful for the pre-asymptotic investigation, while the near-surface aspect was essential for the nanoscale dispersion study.

4.2.1 Dispersion before the Taylor time

In a first subsection here, we will describe the pre-asymptotic part of the dispersion. Essentially, we found in Ref. [133] that the approach to the Taylor result depends sensitively on the initial distribution of particles in the flow domain. In particular we consider the simplest initial distribution possible of a delta-like spike containing two particles only as schematically depicted in Figure 2.15(a), where we also recall the coordinate frame for these experiments: x along the flow, z normal to the substrate, and y the invariant direction. In the initial instants these particles begin wandering up and down the velocity gradient and thus explore at each instant a new velocity. With each new velocity that is sampled, a different, differential displacement is made along the flow direction. Two particles with two different velocity sampling histories will thus be advected by a different distance. Once the particles encounter a boundary, they may be reflected and begin to explore 'already-seen' velocities, thus the histories of individual particles begin to resemble one another and the dispersion starts to be identical, independent of the starting point and independent of the details of the particle trajectory. If the two particles instead are placed at initially different positions, we can see again that the advection distances will be different as compared to the first example, and generally it can be seen how the initial distribution can be important in the pre-Taylor temporal domain.

In the period preceding our study, a considerable theoretical literature on the dynamics of Taylor dispersion existed. Here, Chatwin [206] considered the unbounded case, while Barton [207], and the Bruus group [208,209] made important contributions for the channel cases using moment theory [5]. Experimentally, a few works existed for the point-like case [210–212] and particularly focussed on unbounded domains, but the level of experimental maturity in this domain was limited by comparison with that of the theoretical situation. In Ref. [133], we pointed out several domains in which the time and spatial dependence of dispersion could be important, including for drug delivery from a suddenly ruptured vesicle or in nano-confined and flow chemistry where the spatiotemporal concentration profiles must be critical. We thus turn our

attention to measurements of the spatio-temporal dependence of Taylor dispersion.

In Figure 2.18 are shown the probability of displacement (a) transverse to the flow, Δy, and (b) along the flow, Δx at two different pressures for the latter. The distributions are also sorted according to the particle altitudes, *i.e.* the intensity, as indicated by the green-black curves and the corresponding color bar. Such sorting reveals a dependence on the vertical position for the distribution width. For the streamwise displacements, a noted the difference is also observed between the green-black curves associated with, respectively, the yellow (low pressure) and red (high pressure) distributions in panel (b). A much larger width of green-black distributions for the higher pressure at a given altitude is observed. Such widths allow a determination of the local diffusion and dispersion coefficients, which are shown in Figure 4.4(a) and (b) for the y and x directions respectively. In addition to plotting as a function of z (*i.e.* green-black shade for Figure 2.18), the gradation from red to blue denotes increasing delay times, τ, along a given particle trajectory. Spatio-temporal dispersion is thus accessible using TIRFM.

As expected, the diffusion coefficients in y do not depend on the time and are well described by the theory including Brenner's [51] friction coefficient along the flow direction (black line, see also *e.g.* Refs. [59, 60]). In contrast, a marked time dependence is noted for the dispersion coefficients in (b). As shown in Ref. [133], we note that in addition to the measurements done with 100-nm-diameter particles in water presented here, we also performed experiments with water-glycerol mixtures to increase the fluid viscosity and with larger particles. Both of these variations reduce the diffusion coefficient according to Eq. 1.10, and thus increase the Taylor time, allowing to access a broad range of dimensionless times τ/τ_z. Furthermore, sweeping also the pressure drop across the channel, we were able to rigorously test the shear-rate dependence of Taylor dispersion, confirming a quadratic dependence

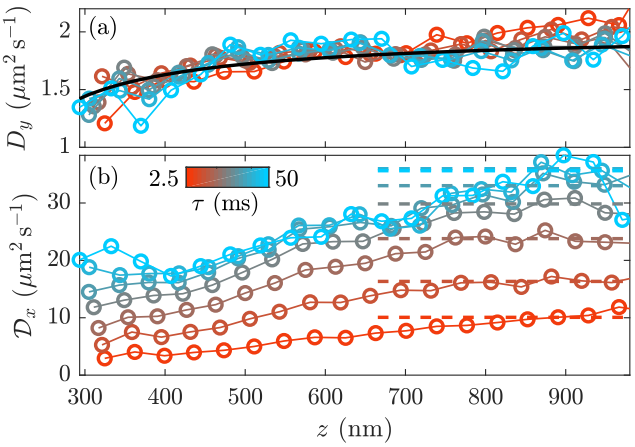

Figure 4.4: Diffusion and dispersion coefficients plotted as a function of distance from the wall for (a) the y direction and (b) the x direction, respectively. In (a), the black line corresponds to the predictions from literature (Brenner, Stokes-Einstein), and for both panels the progression from red to blue indicates the time of travel for a given observed particle. Reproduced from Ref. [133].

on the shear rate [206, 207, 209].

Remarkably, the different accessed viscosities and particle sizes allow for the observation of a reduced temporal dependence for Taylor dispersion. As mentioned previously, nondimensionalisation allowed for the revelation of different master curves when the dispersion is scaled with the Peclet number as suggested by Eq. 1.12; Pe was evaluated *in situ* using the shear rates measured from velocity profiles, diffusion coefficients measured from the displacement statistics along y and the height, h, as read from the SIDs as in Figure 2.19. One example of a master curve is shown in Figure 4.5. The different-colored symbols represent different liquid/particle-size pairs, while the symbols are different imposed pressures and thus shear rates. Different lines represent different theoretical predictions that we shall now describe, while the inset shows the experimental condition accessed, having considered particles in the top half of the evanescent illumination zone.

First, the black dashed line is the prediction of Taylor, having taken h as the extent of the evanescent zone for the calculation of the Peclet number. As this theory assumes long times, it is constant. The black solid line is the prediction of Chatwin [206] for an unbounded flow. Notwithstanding the unboundedness of the theory, one ingredient is the initial distribution which we took as a fraction n of the initial observation zone h, denoting the vertical axis of Figure 4.5 as $\mathcal{F}_{\langle n \rangle}$. We applied the general theory of Chatwin for any initial distribution and any velocity profile to a uniform stepwise distribution in a linear shear flow. It could thus be shown that the master curve should follow

$$\mathcal{F}_{\langle n \rangle} = \frac{n^2}{6}\left(\frac{\tau}{\tau_z}\right) + \frac{4}{3}\left(\frac{\tau}{\tau_z}\right)^2 , \tag{4.1}$$

for times short compared to the Taylor time. The Chatwin theory thus reveals two pre-asymptotic regimes characterised by a short-time linear increase in the dispersion

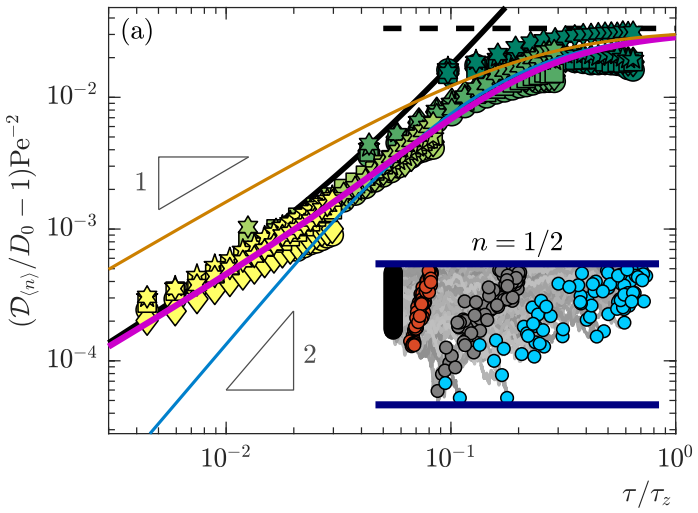

Figure 4.5: Rescaled dispersion for all liquid-particle pairs as a function of reduced time for particles beginning their trajectory in the top half of an observation zone. Reproduced from Ref. [133].

coefficient with a crossover to an intermediate, quadratic time dependence, as shown by the black curve with $n = 1/2$ as accessed in the experiment.

To explain Eq. 4.1 in a naïve sense, we note that when the time to diffuse a distance larger than the initial extent is reached, the initial distribution starts to look like a 'point' and thus the quadratic time dependence is observed. The quadratic is explained by considering the difference squared in the distance travelled along the flow for particles respectively moving up or down: the typical distance travelled vertically is $\sigma_z^2 \sim D_0\tau$ while the distance travelled along x is $\sigma_x^2 \sim (\dot{\gamma}\tau\sigma_z)^2 \sim \dot{\gamma}^2 D_0\tau^3$ and thus $\sigma_x^2/\tau \sim \tau^2$. The linear increase at early times is, in contrast, linked to the ballistic shearing of the initial distribution with $\sigma_x^2 \sim (\dot{\gamma}\tau h)^2$ and thus $\sigma^2/\tau \sim \tau$. The early-time data of Figure 4.5 agrees well with the curve predicted by Chatwin.

In order to predict the crossover into long times considered by Taylor [4], the moment theory [5, 207–209] was used for a closed channel of height h and velocity profile $v_x(z)$. Our implementation of the theory is merely sketched here, with details found in Ref. [133]. We assumed simple reflective boundary conditions for the particles and uniform particle diffusion coefficients, these assumptions to be confronted in the following subsection on nanoscale dispersion. Regardless of the assumptions, the moments are defined as

$$C_p(X,T) = \int_{-\infty}^{\infty} dX\ X^p C(X,Z,T)\ , \tag{4.2}$$

$$M_p(T) = \int_0^1 dZ\ C_p(Z,T)\ , \tag{4.3}$$

where capitals denote dimensionless counterparts of the variables $\{c, x, z, t\}$. Multiplying the advection-diffusion equation and integrating gives rise to the moments. The result is a series of equations for each value of p, larger values dependent on the solutions for smaller values; it is thus a recursive theory with the structure

$$\left(\partial_T - \partial_Z^2\right) C_p(Z,T) = p(p-1)C_{p-2} + p\mathrm{Pe}V(Z)C_{p-1}, \tag{4.4}$$

$$\partial_T M_p(T) = p(p-1)\langle 1, C_{p-2}\rangle + p\mathrm{Pe}\langle V_X(Z), C_{p-1}\rangle, \tag{4.5}$$

where $V_X(Z)$ is the dimensionless velocity profile and the angle brackets in the second equation denote integration along Z of the product of the arguments. The dispersion is thus given by $\mathcal{D}_x/D_0 = (M_2 - M_1^2)/2T$, consistent with Chatwin's definition and our experimental one, and necessitating moments up to second order.

The thick purple line in Figure 4.5 shows the prediction of the moment theory outlined in the previous paragraph assuming particles begin their trajectory in the top half of the observation zone only. The prediction matches the rescaled data over the entire range of accessible times suggesting that the theory provides a good description of the data. The other coloured lines are different realisations of the main theory, changing only the initially-occupied portion of the observation channel. The upper line with initial log-log slope of 1 considers a uniformly filled channel, while the lower line with log-log slope 2 is for a point-like initial distribution. While not shown here, we note that by considering all particles of the data set (yellow or red data in Figure 2.18), we could reproduce the upper line, while selecting a relatively narrow band of intensities the power-law-2 line could be approached, and certainly

violated the $n = 1/2$ prediction. That the initial power law spreading is dominated by the initial condition in such a way is, to us, a remarkable feature of the theory, and points to the need to carefully address the initial spatial distribution of solute for understanding pre-asymptotic Taylor dispersion. Having described this temporal aspect, we will now describe in detail the effects of interactions with the confining boundaries, including electrostatic potentials, anisotropic diffusion, and consumption at the upper boundary, these effects having been neglected in this first part.

4.2.2 Taylor Dispersion in confinement

In the previous section, we ignored interactions of the particle with the glass-water interface, comprising both hydrodynamic ones that influence the diffusion coefficient, and the energetic ones described by Eq. 1.6 that may lead to a depletion of particles near the wall. Furthermore, we made no mention of the fact that the upper boundary of the evanescent zone is an open one. This openness in fact violates the reflectivity condition that was assumed in the previous section, and as we will see can have a rather major effect on the magnitude of nanoscale dispersion. The situation to be described in the following is thus sketched in Figure 4.6.

The transport of microscopic objects in sub-micrometric spaces is ubiquitous particularly in microscopic biology. Here, proteins, cells and other particulate objects are subjected to external flows and diffuse readily due to the colloidal scales at play. Furthermore, such spaces are characterised by complex interfaces which may pilot the interactions of these aforementioned particles. Besides, Taylor dispersion is commonly used to measure the molecular diffusion coefficient of molecules [213–217] for the pharmaceutical industry, and the problem of boundary adsorption [218], for example, was already noted for macroscopic assays, amounting to a few 10's of percent systematic bias on the measured diffusion coefficients. As for the previous section, a considerable historical and emerging theoretical literature [219–223] exists concerning the interaction-dependence of Taylor dispersion with a new particular attention on intermolecular interactions and surface fluctuations. Our study thus marks one of the few experimental forays into the micro- [224] and nano-scale [225] observations of the phenomenon. TIRFM, furthermore, due to its capacity to measure both the probabilistic structure and dynamics at the particle level and in the near-surface region, is particularly relevant as an experimental probe.

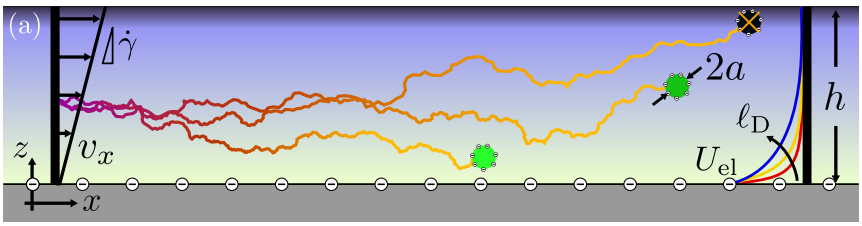

Figure 4.6: Taylor dispersion in a shear flow, subjected to electrostatic interactions due to negative surface charges on the particle of size a and wall. The interaction U_{el} is characterised by a Debye length, ℓ_D, while particles reaching the top wall at $z = h$ are eliminated. Reproduced from Ref. [134].

To control the interactions of a particle and a glass-water interface, we varied the concentration of monovalent salt injected with the particle in our microfluidic channels. Increasing the concentration of salt reduces the Debye length (Eq. 1.3), thus providing an effectively enlarged flow domain. In Figure 4.7 are shown (a) the temporal dependence of the dispersion taken from particle ensembles as in Figure 2.16, but for different salt concentrations; different pressures are normalised in this representation by dividing the reduced dispersion by $\dot{\gamma}^2$ measured *in situ*. In (b) are shown SIDs as they are dependent on the concentration of NaCl (bottom annotations). As the effect of the open boundary was noted above, we also varied its position by adjusting the laser power for all salt concentrations, although this variation is shown only for water. When the laser power is reduced, we note a decrease in the apparent altitude[1] for which particles are no longer seen, consistent with the constant noise floor of the camera. A resulting reduction in the long-time dispersion is also noted in (a) for reduced laser powers. In the following, we will only consider these long times.

In Figure 4.7(a), we note that the largest late-time dispersion is for the largest salt concentration, corresponding to the smallest Debye length and thus largest sampled

[1]A slight mismatch in the notations between the time-dependent study and this one is noted. In this section, z_{app} is proportional to the log of the fluorescence intensity, whereas z was used for this same quantity in the previous study. While not detailed here, the ambiguity arises from polydispersity and optical effects related to the depth of field of the objective, this latter being also a few hundred nanometers. For details see the appendix of Ref. [133].

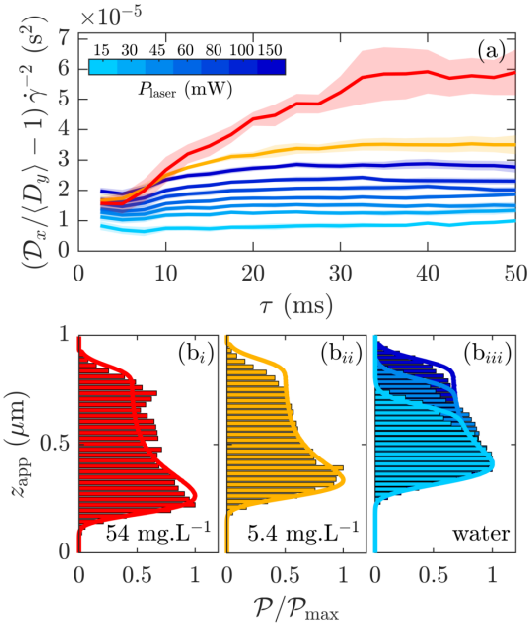

Figure 4.7: (a) Time dependent, shear-rate reduced and normalised dispersion for different salt concentrations as noted in (b), with a common color scheme. Here $\langle D_y\rangle$ is taken as the vertically averaged diffusion coefficient in the y-direction. The inset indicates the laser power. (b) SIDs as in Figure 2.19 for the various salt concentrations. For clarity, only three laser powers are shown in part (*iii*). Reproduced from Ref. [134].

flow domain for the particles. This enlarged particle flow domain for the highest salt concentration is indeed reflected in the reduced, near-wall depletion of part (b). In increasing the salt concentration to 54 mg/L from the ultrapure water typically used, we varied the Debye length from *ca.* 60 nm to roughly 10 nm, as revealed by the fits of the SIDs [139] in Figure 4.7(b). For the 800 nm flow domain, we see that this unique change of 50 nm in the screening length had the effect of a factor 3 change in the dispersion. Thus, as a first quantitative conclusion concerning the data in Figure 4.7, we note that a small change —some 10% on the flow domain size— in the physico-chemical length scales provokes a drastic dynamical change of some hundreds of percent.

To understand the data set of Figure 4.7, we once again used a version of Eq. 1.11 with modifications to include (*i*) z-dependent diffusion coefficients that are distinct in the x- and z-directions [46,51], along with (*ii*) a conservative force in the z-direction arising from the potential of Eq. 1.6. Besides, the reflective boundary condition at the top wall was modified to include (*iii*) the possibility that particles may wander out of the observation zone. Thus, we assumed that a particle leaving the observation zone during a trajectory is consumed, for which we imposed a null-concentration condition at this latter boundary; mathematically, this entails changing the boundary conditions from pure Neumann on both sides to mixed Neumann-Dirichlet conditions on opposite vertical boundaries of the flow domain.

The resulting advection-diffusion problem is rather more complex than the one of the previous section, due to the additional three ingredients described in the previous paragraph. Nevertheless, the methods of moment theory [5, 207–209, 226, 227] were once again used. With the details found in Ref. [134], we note in particular that the zeroth moment satisfies

$$\left(\frac{d}{dt} - \frac{d}{dz}\left(D_z(z)\left[\frac{d}{dz} + \frac{U'_{\mathrm{el}}(z)}{kT}\right]\right)\right) c_0(z,t) = 0 \ , \tag{4.6}$$

which has the structure of an eigenvalue problem of the Sturm-Liouville type which for our case is solved numerically [228]. The eigenvalues λ_k play the role of temporal damping coefficients, and have in particular a smallest, finite value $\lambda_1 > 0$,

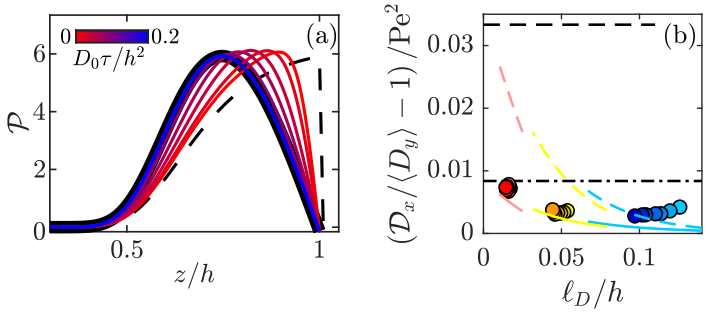

Figure 4.8: (a) Time dependence of the particle probability density as a function of particle position. (b) Reduced dispersion coefficients for the three salt concentrations and all laser powers, as a function of the height-normalised Debye length. The different lines are described in the text and the equations associated are shown in Figure 4.9. Reproduced from Ref. [134].

that sets the long time exponential decay of the concentration field; that is, $c_0 \approx \exp(-\lambda_1 t) f_0(z)$ for times $t \gg \lambda_0^{-1}$. The non-zero eigenvalue expresses the non-conserved particle number, resulting from the open boundary. Otherwise, the early-time behaviours are set by a sum over all of the modes λ_k, each mode set with the temporal decay of the form $\exp(-\lambda_k \tau)$ with details on the solution of the spatial problem found in Ref. [134].

A key insight of the theory is provided in Figure 4.8(a), where the time-dependence of the probability density is shown, corresponding to $\mathcal{P}(z,t) = c_0(z,t)/m_0(t)$. The moment in the denominator is $m_0(t) = \int dz\ c_0(z,t)$ with the integration over the entirety of the observation zone. The initial condition was taken as a Boltzmann-distributed probability density (dashed black line). As the time increases (red to blue), we note that a depletion of particles builds up near the top of the channel ($z/h = 1$) while the depletion due to the electrostatic repulsion near $z = 0$ is constantly present. The former depletion at the top of the channel is a unique consequence of the particle consumption condition. Interestingly, the probability distribution saturates at long times $t \gg \tau_z$ to a quasistatic function that violates the equilibrium Gibbs-Boltzmann distribution; furthermore, this long time distribution is purely physico-chemical as it does not depend on the initial concentration field.

Experimentally, such quasi-steady probability densities were observed by considering particle trajectories, setting $\tau = 0$ for the initial particle observation time. As the delay time increases, $\tau > 0$, a distinct and quasi-steady SID is observed (see Ref. [134]). Essentially, these distributions are the ones observed by considering the particles that remain in the particle clouds shown in Figure 2.16. Crucially, these distributions are distinct from those presented in Figures 2.19 and 4.8(b), these latter considering all particles irrespective of the observation time and thus Boltzmann-like.

In a dynamic sense and on the ensemble level, the channel-top depletion removes progressively the possibility for particles to sample velocities near the top of the observation zone. As the diversity of sampled velocities decreases, the dispersion due to the Taylor mechanism is hindered. We thus expect a reduced Taylor dispersion due to the repulsive and effective adsorption interactions. In order to test the hypothesis, in Figure 4.8(b) we plot (circles) the reduced Taylor dispersion as measured in the experiments with the height of the channel taken as the distance between the glass-water interface and the inflection point of the SIDs shown in Figure 4.7(b). We also computed the expected dispersion based on models that are summarised in Figure 4.9, including progressively more physical ingredients.

We first note a reduction in the dispersion by an order of magnitude in comparing the data to the classical Taylor prediction (black dashed line). Therefore, confinement may have a drastic impact on particle dispersion. A tracer theory (*i.e.* no interactions) including only particle consumption at the upper boundary reduces by a constant factor of approximately 4 the dispersion – this theory notably excludes electrostatics. However, this tracer theory does not differentiate between the different salt concentrations, while the data does distinguish them. Considering only electrostatics does not capture the full decrease in the dispersion, which is finally captured incorporating electrostatics and absorption.

To explain intuitively why the combined effect of both electrostatics and absorption is so large, we may consider the original Taylor scaling of the dispersion with

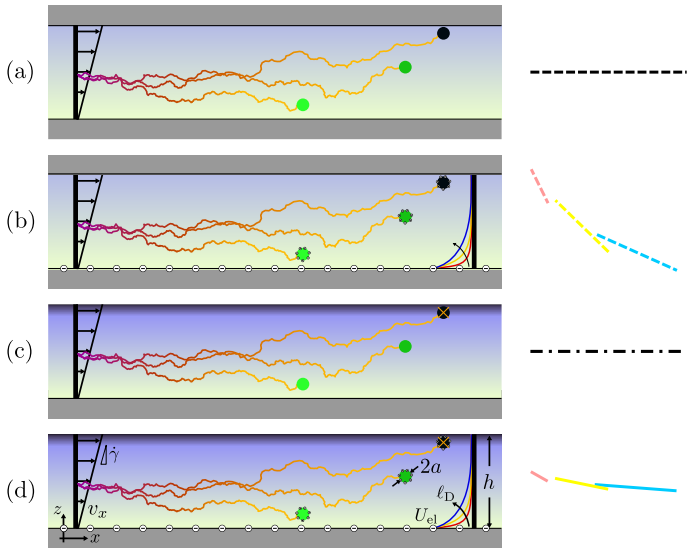

Figure 4.9: Schematic illustration of the models tested in Figure 4.8(b). First, (a) Taylor theory for tracer particles, no interaction, reflective boundaries. (b) Moment theory with bottom-wall, electrostatic interaction only, reflective top wall. (c) Moment theory with absorption at the top wall only, reflective bottom. (d) Moment theory with absorption and electrostatic interactions. Reproduced from Ref. [134].

$\mathcal{D}_x/D_0 \sim \mathrm{Pe}^2 \sim \dot{\gamma}^2 h^4/D_0^2$ for large Pe. In this case, we see that the channel height figures in the scaling with a strong power-law. Therefore, reducing the effective channel height through depletion of both electrostatic and absorptive origin can be expected to give strong dynamical consequence at the nanoscale. This is indeed seen through the factor-10 decrease as compared to the prediction containing no interactions.

While we will return to this work in the context of future projects, this section is closed with a few remarks concerning the choice of channel heights and the aspect of near-wall hindered diffusion. In the previous section [133], we were able to collapse the time-dependent dispersion data onto master curves only through a judicious and systematic choice of the height scale. Thanks to access to the SIDs, the height, h there was chosen as the zone containing an adjustable constant times the standard deviation of the particle altitudes, in practice giving roughly 99% of the observed particles. This global measure of the 'effective' channel size was enough to collapse all the data sets onto the master curves generated. It does not, however, correspond to the distance from the wall to the detection limit, and ignores any effect such as the electrostatic interaction and thus represents an effective channel size. Practically, it is not the case for all experiments that such detailed observations can be made, and sometimes only the entire size of the nanopore, for example, is known from an independent AFM or scanning electron microscopy measurement. Knowledge of the particle/boundary interactions is thus necessary for the correct interpretation of dispersion phenomenon as well as, *e.g.* transit time statistics for particles in nanopores [229].

Lastly, we comment briefly on the effect of hindered diffusion. In Ref. [134] we noted that the reduced dispersion plotted in Figure 4.8(b) is a function in particular of

the ratio a/h and of a/ℓ_{D}, comprising finite size diffusive and electrostatic effects. As our particles are rather small and the typical particle-wall distances are bigger than the particle size, lubrication effects are limited in a global sense. Finally the hindered diffusion, while measurable in the near-surface region as displayed in Figure 4.4, has rather limited effects on the total dispersion within the evanescence zone we accessed.

Concluding this chapter, we note that TIRFM combined with microfludics and particle tracking has proven to be a useful method for studies on soft matter transport at nanoscales and reaching the micrometer. Polyelectrolye solutions, in the semidilute concentration regime develop a nanoscopic depletion layer at glass-water interfaces, provoking apparent slip. The concentration of polymer and electrolyte can be used to tune the boundary condition from no slip upon an adsorbed layer, to tens of nanometers and indeed some microns. In the context of Newtonian fluids, we considered the statistical variance of the particle motions to study Taylor dispersion in pre-asymptotic temporal regimes and in confinement. Concerning the former we found a strong dependence on the initial spatial distribution of the dispersed species. Meanwhile, nanoscale Taylor dispersion is extremely sensitive to interactions with the boundaries, whether arising from equilibrium or non-equilibrium interactions based on particle-surface potentials or effective absorption.

Chapter 5

Elastohydrodynamics of porous media and conduits

In the end of the previous chapter, we downplayed somewhat the importance of hydrodynamic interactions between the particles and the solid-liquid interface at the bottom of our microfluidic chips and for particles of 100 nm diameter not typically approaching less than 100 or 200 nm from the surface. Nevertheless, if the idea of these so-called hydrodynamic interactions has already appeared several times in this manuscript, it is because such interactions will be central in this chapter. In the next section, an elastohydrodynamic problem related to the particle-surface diffusive one is described, wherein we treat the Reynolds' lubrication scenario of a large sphere approaching a surface, this latter being a soft layer that is additionally porous.

Soft and porous materials are present in a large number of contexts, from pharmaceutical applications to nanoscale polymer layers forming an intermediate layer between a liquid and a solid boundary. As an example of the latter context, cartilaginous joints with a fluid-facing polymer coating between bones and synovial liquid exhibit very low friction [230]. Otherwise, eyelid wipers are known to deform due to the hydrodynamic stresses within the tear film between the eye and the lid [231,232]; such a performance is known also to be influenced by a biopolymer brush layer, swollen with solvent, lining both surfaces. At smaller scales still, arteries are lined also with polymeric, hyaluraonic acid brush layers. Such layers are deformable and may exert a normal force on nearby blood cells in flow; in Ref. [233] this lift force was demonstrated using hard colloidal particles under flow, highlighting the importance of brush layers' softness. Such lift forces are not the subject treated here, yet a review on the subject is proposed elsewhere [7].

Besides particle-solid, fluid-mediated interactions, a second section of this chapter deals with the elastohydrodynamics of flow within a flexible-conduit. Such problems are also vital in vascular systems [234, 235], as the arteries transporting blood are deformable under flow and crucially govern oxygen transport throughout the body. Several researchers investigated the deformability of these or other channels, leading to static, non-linear, pressure-versus-flow relations [236–240]. The heart, meanwhile, may exhibit several modes of deformability, providing a scaling law between heart rates and their corresponding geometry across a broad range of animal species [241]. Furthermore, elastohydrodynamic relaxation gives design principles for stop-flow

lithography in microfluidic devices [237], among other applications [242–246]. Considering the basic interest and emerging applications, we thus identified [66] the transient regime following a stepped-pressure perturbation as a relatively unexplored fundamental topic, making up the second section of this chapter.

5.1 Poroelastic hydrodynamics of a slow approaching sphere

In contrast to the other works presented in this manuscript, the work by Caroline Kopecz-Muller [65] is a purely theoretical one. Several experimental results inspired by the calculations and the ideas to be presented in this section have been carried out, yet the interpretation of the data, some of which shall be mentioned in the perspectives of Section 6.2, are yet reaching maturity and thus will not be commented in detail.

The central idea, and the main novelty, of this work is the introduction of a porous component to the solid half of the elastohydrodynamic squeeze-flow framework set out by several other groups [247–252]. In these works, the fluid-immersed sphere approaching an elastic substrate is considered theoretically and experimentally. The materials used were typically silicone elastomers wherein the elastic modulus dominates the lossy one, and thus could be well described by purely elastic theories. However, there are many applications in which soft elastomers are used, the strategy employed to control the softness often being to dilute the crosslinking network, increasing N and thus reducing G in Eq. 1.1. This strategy does gives rise to soft elastomers, yet may implicate the presence of a considerable quantity of uncrosslinked chains [253].

Uncrosslinked chains are free to diffuse through the network and it may be expected that such motion could lead to viscous dissipation in a typical elastohydrodynamic, squeeze-flow experiment. Such dissipation is for example important when droplets move across viscoelastic and/or poroelastic substrates [253–255], making up an important class of problems complementary to the contact line motion problems described in Section 3.2.2 concerning hard substrates. For the poro-viscoelastic case the presence of a contact line induces the formation of a ridge [254,256] whose motion implicates considerable dissipation. For such problems a poroelastic substrate with an impermeable boundary condition between the phases was considered by the Dervaux group [257], prohibiting the exchange of material between the two phases. This latter work largely inspired the following theoretical framework, while the application of the here-developed theory is applied to the squeeze-flow context of, for example, the Charlaix and Frechette groups [247–252].

5.1.1 Point-force response

In the theory of the Dervaux group [257], linear elasticity of a compressible elastic material occupying an axisymmetric half space, with modulus G and Poisson ratio ν as schematically indicated in Figure 5.1(a), is assumed for the poroelastic solid. Herein, the stress includes terms proportional to the strain (*i.e.*, the displacement field gradients) and a chemical potential term. The poroelastic solid is initially swollen with

solvent concentration c_0 and thus chemical potential μ_0. Gradients in the chemical potential, μ, induce a vectorial solvent flux that follows a Darcy law of the form

$$\mathbf{J} = -(k/\eta\Omega^2)\nabla\mu \ , \tag{5.1}$$

with k and Ω being the pore permeability (with dimensions of an area) and the volume of a solvent molecule. Combining the preceding ingredients with continuity equations on the solvent flux and incompressibility of the entire network with Navier's closure condition leads to two coupled equations for the concentration field and chemical potential:

$$\nabla^2\left[(\mu-\mu_0) - G\Omega^2\frac{1-\nu}{1-2\nu}(c-c_0)\right] = 0 \ , \tag{5.2}$$

along with

$$\partial_t c = \mathcal{D}_{\rm pe}\nabla^2 c \ . \tag{5.3}$$

Here, the effective poroelastic diffusion coefficient

$$\mathcal{D}_{\rm pe} = 2\frac{(1-\nu)}{1-2\nu}\frac{Gk}{\eta} \ , \tag{5.4}$$

is of order the molecular diffusion coefficient of the solvent molecules (see the discussion on this point in Ref. [65]). These equations were solved under a point force loading with magnitude F_0 as in Figure 5.1(a), delta distributed in space and following a Heaviside temporal dependence, $F(r,t) = -F_0\delta(\mathrm{r})H(t)$, in the vertical direction. In contrast to the Dervaux work where a no-flux condition was applied with $\partial_z\mu = 0$, the boundary at the poroelastic-solid/liquid interface is permeable in our case. Thus we prescribe the chemical potential, μ_0, of the liquid at the undeformed interface.

The solution method, not detailed here, relies on a transformation of the displacement fields into displacement potentials similar to the ones encountered in solutions for Stokeslet flows or in electromagnetism. The problem, furthermore, is amenable to a simple closed-form solution in reciprocal space, where we take $\{s,q\}$ as the reciprocal variables to $\{r,t\}$, while the vertical direction, z, remains untransformed and we denote w as the deformation of the surface at $z=0$. The solution for the surface deformation in reciprocal space is thus

$$\hat{w}(s,q) = \frac{F_0}{4\pi G s q}\left[1+\Lambda\frac{\mathcal{D}_{\rm pe}s^2}{q}\left(1-\sqrt{1+\frac{q}{\mathcal{D}_{\rm pe}s^2}}\right)\right]^{-1} \ , \tag{5.5}$$

where we defined a compressibility factor

$$\Lambda = \frac{1-2\nu}{1-\nu} \ . \tag{5.6}$$

Examing Eq. 5.5, we see that the response is composed of an incompressible elastic part (when $\nu = 1/2$ and thus $\Lambda = 0$), and a compressible part dependent on space and time as a result of the porosity. This latter porosity allows for solvent motion throughout the elastic matrix as $\mathcal{D}_{\rm pe}\propto k$. The spatio-temporal dependence is

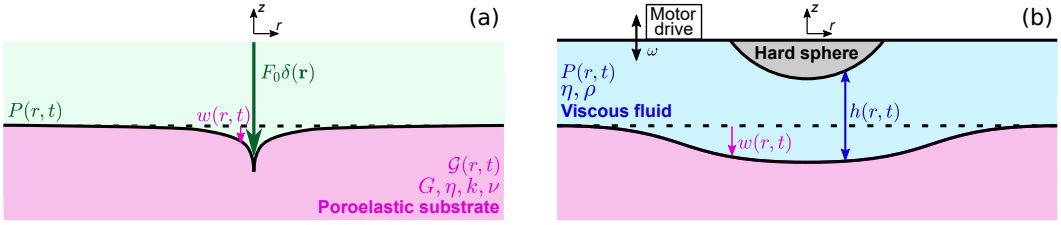

Figure 5.1: (a) Schematic of the poroelastic Green's function, in which a point force is applied to an axisymmetric, poroelastic half space. (b) Poroelastic-hydrodynamic squeeze flow scenario typical of an SFA or colloidal-probe AFM experiment. Reproduced from Ref. [65].

thus diffusive as seen by the typical combination s^2/q and moderated by the effective poroelastic diffusion coefficient, mainly resulting from the diffusive structure of Eq. 5.3.

Interestingly, the time dependence of Eq. 5.5 bridges two asymptotes at the $t = 0^+$ instant and as $t \to \infty$. Right after the imposition of the force, the solvent has not had time to move and the material behaves as an incompressible solid while at long times the solvent has migrated under the action of the force. We thus have in these asymptotic limits

$$w(r,t) = \frac{F_0}{2\pi G r} \times \begin{cases} \frac{1}{2} & \text{if } t = 0^+ \text{ ; incompressible} \\ (1-\nu) & \text{as } t \to \infty \text{ ; compressible} \end{cases} . \tag{5.7}$$

These collected observations concerning Eq. 5.5 are illustrated in Figure 5.2(a). Therein, plots of the deformation are shown as a function of the reciprocal-space radius s for various reciprocal times q; we normalise lengths by $\sqrt{F_0/G}$ and time by $F_0/G\mathcal{D}_{\text{pe}}$. We note that the transition between the incompressible and compressible asymptotes (dashed lines) occurs at a particular position that depends diffusively on the time; such a diffusively-mediated temporal crossover is highlighted in part (b), showing a collapse of all the curves with the appropriate diffusive scaling. We note lastly that in Ref. [65], we made a detailed comparison to the non-permeable theory [257], which also provides diffusive-like dynamics. The main difference is that the permeable theory is slightly faster owing to the solvent exchange with the bath, and the non-permeable version of Figure 5.2(b) shows a slight non-monotonicity due to volume conservation; the solvent moves under the action of the force but it cannot escape. In either case, the principal effect of porosity, therefore, is (*i*) to provide a mechanism for solvent mobility through the elastic network; and (*ii*) to give a diffusive crossover between incompressible and compressible behaviours.

5.1.2 Lubricated poroelastic squeeze flow

As an application of the previous results, we considered the lubrication situation shown in Figure 5.1(b). There, a sphere of radius R is placed at a central height D above the undeformed surface that oscillates with frequency ω and amplitude h_0 in a liquid with viscosity η. For the case in which $R \gg D$, a radially symmetric version

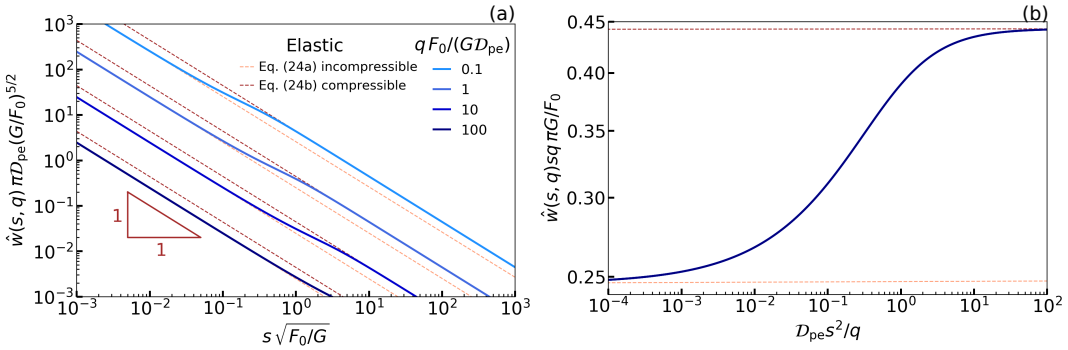

Figure 5.2: (a) Dimensionless, normalised surface deformation as a function of the dimensionless reciprocal radial coordinate (*n.b.* the reference to Eq. 24 should be replaced with one to Eq. 5.7). (b) Normalised surface deformation highlighting a diffusive crossover position between incompressible and compressible asymptotes. Reproduced from Ref. [65].

of the Reynolds lubrication law of Eq. 1.13 is used for the fluid in the gap, thus

$$\partial_t h = \frac{1}{12\eta r}\partial_r\left(rh^3\partial_r p\right) \ , \tag{5.8}$$

where the height is therefore given by

$$h(r,t) \approx D + h_0\cos(\omega t) + w(r,t) + \frac{r^2}{2R} \ . \tag{5.9}$$

Furthermore, we consider the oscillatory perturbation limit with $h_0 \ll D$ and in which the Leroy work considered a purely elastic layer [247, 248]. Following those works, we linearised the lubrication equation and used the results of the delta-distributed force calculation Eq. 5.5 to estimate the deformation resulting self-consistently from

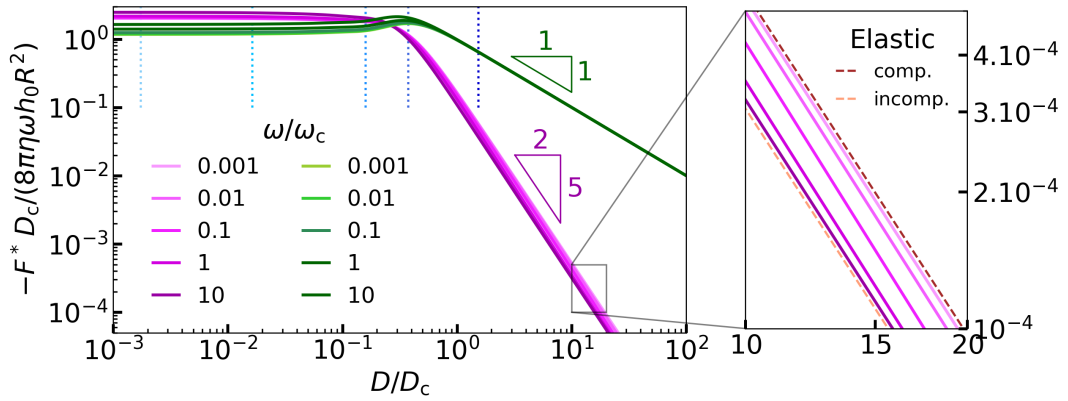

Figure 5.3: Real (purple) and Imaginary (green) components of the complex force for a lubricated sphere above a poroelastic half space. Different dimensionless frequencies are shown in the legend. Reproduced from Ref. [65].

the pressure, convoluting the latter with the Green's function, $\mathcal{G}(s,q) \propto w(s,q)$ for the point force, in order to obtain the full deformation field. With details left in Ref. [65], we note that the deformation and pressure can thus be determined numerically. Integrating the pressure, a complex force was obtained, notably giving rise to storage and loss components in analogy to oscillatory rheology. Notably, a critical distance as in Refs. [247, 248],

$$D_\mathrm{c} = 8R\left(\frac{\eta\omega}{2G}\right)^{2/3} , \tag{5.10}$$

determines a crossover between the real and imaginary components of the force. A critical frequency is furthermore defined as the inverse time for which solvent molecule diffuses a distance of the typical contact patch size of the indenter at the critical distance, $\sqrt{2RD_\mathrm{c}}$, thus

$$\begin{aligned}\omega_\mathrm{c} &= \frac{\mathcal{D}_\mathrm{pe}}{2RD_\mathrm{c}} , \\ &\approx \frac{G}{\eta}\left(\frac{(1-\nu)}{1-2\nu}\frac{k}{R^2}\right)^{3/5} ,\end{aligned} \tag{5.11}$$

with the missing numerical prefactor being $2^{-7/5}$ and where in the second equality we inserted the definition of $\mathcal{D}_\mathrm{pe}$ and self-consistently imposed ω_c from the definition of D_c.

In Figure 5.3 we show the principal result of the poroelastic squeeze flow scenario in the form of complex force distance curves. For the large D/D_c limit, the imaginary part displays the characteristic D^{-1} power law for the Reynolds' drainage force above a rigid substrate. The real part is however non-zero as there is some storage component arising from the elastic deformation of the poroelastic substrate; the distance scaling $F \sim D^{-5/2}$ is identical to the purely elastic case [247, 248]. The effect of porosity is subtle in this representation, with a near-collapse of the data, but for an effective frequency-dependent offset at large distances in the storage component of the force. This offset is dependent on the frequency with the critical one providing the crossover between small and large frequency. In these limits, the poro-elastic-hydrodynamic theory predicts a correspondence with compressible and incompressible, purely elastic cases which are shown as dotted lines.

Practically speaking, elucidating the subtle effect of porosity displayed in Figure 5.3 for the lubricated approaching sphere would make for a difficult and equally subtle measurement. As seen in the figure, fixing D/D_c in the theory, a variation by two orders of magnitude of the frequency would give rise to a modest factor of order unity change in the storage modulus, and less for the lossy one. Meanwhile, a fixed dimensionless distance would require a simultaneous variation of the experimental distance, as the scaled one is a function of the dimensional frequency. A rigorous test of the porosity effect in this context thus appears to be challenging. Nevertheless, and in a perhaps more optimistic view, many practical applications make use of such porous materials and an evaluation of their modulus may be crucial. Furthermore, the materials are generally delicate, due to their relatively low moduli. The experimental protocol suggested by the preceding theoretical calculations is non-contact, as pointed out also in several earlier works [247, 248]. It thus

appears that a hydrodynamic evaluation of elastic moduli is an ideal, non-destructive method for evaluating certain mechanical properties of poroelastic gels. In a more fundamental vein, we often want to investigate the influence of soft boundaries on different transport problems such as near-surface colloidal transport. As hydrogels are readily created by many groups [258], our study demonstrates that, in a first approximation, these versatile materials can be used as ideal elastic substrates for the purposes of elastohydrodynamic inquiry.

5.2 Transient relaxations in soft hydraulics

In Figure 4.3(b) we show evidence for an adsorbed polymer layer at the glass-water interface of a microfluidic chip. While not an elastohydrodynamic phenomenon, it was the means by which we entered the topic often referred to as soft hydraulics [239]. One of the motivations for studying adsorption of polymers in microfluidic chips was to create model, individual "pores" as encountered by TotalEnergies, our industrial partner during the thesis of Gabriel Guyard, during enhanced oil recovery. In these contexts [196], large, water soluble polymer molecules (molecular weights of some 10^7 g/mol) are used as viscosifying agents and pumped through porous rock beds to displace the entrapped oil. Polymer adsorption is a key consideration [198] in such situations as a considerable pressure loss occurs in the thinnest pores, which may be of order the chain size. Studying such adsorption is often done on a macroscopic scale with pressure-debit relations measured across rock samples before and after exposure to polymer solutions; such experiments allow to assess the average porosity as in Eq. 5.1. Our goal was to mimic such studies at the individual pore level with the molecular scale view offered by TIRFM. In order to measure a debit along with an appreciable reduction due to adsorption, and to simultaneously observe colloidal-particle dynamics in the near surface region using TIRFM [135], we were thus motivated to employ thin and wide microfluidic chips. As slender objects are amenable to deformation under modest loads, our investigations thus led us to the aforementioned soft hydraulics [236–240], the context of which is outlined in the first paragraphs of this chapter.

Serving as calibrations for the polymer-flooding experiments, and using commercial flow and pressure meters, we thus measured pressure-debit relations for water in microfluidic chips prepared via soft lithography [67], the experiments schematically indicated in Figure 5.4(a). The flow meter provided an ideal flow resistance, r_0 while the pressure meter contains a flexible membrane capable of a volume storage capacity c_0, indicated in the electrical analog of part (b). The chips placed in series with the previous elements had length and undeformed height $\{L, h_0\}$ of 8 cm and 5 μm and a series of widths $w = \{200, 500, 1000, 2000\}$ μm. In Figure 5.4(c) is shown a time series for the pressure, p_0, and debit, q_0, at the entrance of the microfluidic channel during a single step in the setting on the pressure controller, p_{in}. As this input pressure is changed suddenly, the debit and pressure between the flow meter and microfluidic chip also change, eventually reaching steady values, q_∞ and $p_{0,\infty}$, respectively.

In Figure 5.4(d) is shown the steady-state debit as a function of the steady-state pressure at the inlet of the microfluidic chip for each of the channel geometries we investigated. The dependencies are clearly nonlinear, which is in direct contrast with

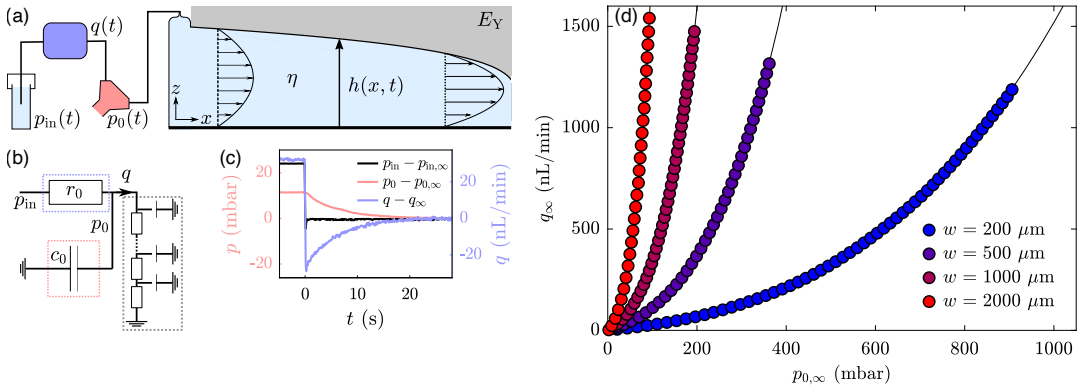

Figure 5.4: (a) Schematic of the soft hydraulic, microfluidic setup including a fluid reservoir, debit and pressure measurement at the input of the micrfluidic channel, the boundary shown in grey. (b) An electrical-circuit analog of the microfluidic setup. (c) Time series for pressure, p, and debit q as a function of time for a 200 μm wide glass-bottomed PDMS microchip. (d) Steady-state debit as a function of steady-state pressure for the indicated microfluidic chip widths, with $p_{\text{in},\infty} = 1303$ mbar, $p_{0,\infty} = 862$ mbar, $q_\infty = 1058$ nL/min. Reproduced from Ref. [66].

a constant, ideal resistance as expected for rigid flow domains [61, 62]. Of course, PDMS is a soft elastomer, and the chips used as noted above are rather slender with $h_0/w \leqslant 0.025$.

In order to explain the data in Figure 5.4(d), therefore, we suggested a linear dependence on the deformation of the channel boundary with the pressure, thus

$$h = h_0 + w\frac{p}{E_*} \ , \tag{5.12}$$

where E_* is proportional to the Young modulus and depends on the geometry of the upper elastic layer. For a thick slab, much thicker than the channel width, Wang and Christov [240] showed that the factor is roughly equal to $[0.54(1-\nu^2)]^{-1}$. This height-pressure relation governs the local elastic response of the upper boundary, while the fluid layer is well-described by the classic lubrication Equation 1.13. These two equations form a closed system whose dimensionless, steady state reads $0 = \partial_X\left((1+P)^3\partial_X P\right)$. Here, x is normalised by L and p is normalised by $p_* = Ew/h_0$ highlighting the importance of the slenderness of our channels. The bracketed expression of the steady state equation represents the dimensionless debit, which can easily be integrated with $p = p_0$ at $x = 0$ and $p = 0$ at the outlet to give the pressure profile, debit, and dimensionless pressure offset

$$P_\infty(X) = [(1-X)\Pi + 1]^{1/4} - 1 \ , \tag{5.13}$$

$$Q_\infty = \frac{1}{4}\Pi \ , \tag{5.14}$$

$$\Pi = (1+P_{0,\infty})^4 - 1 \ . \tag{5.15}$$

Here the dimensionless debit is $Q = r_c q/p_*$ and the undeformed hydraulic channel resistance is $r_c = 12\eta L/wh_0^3$ [62]. The height profile thus roughly scales as $h(x) - h_0 \sim$

$(L - X)^{1/4}$ and the debit is roughly $q \sim p^4$, *i.e.* the debit is strongly non-linear with the pressure as seen in the data. These observations are in good accord with the existing literature [236–238]. Besides these qualitative agreements, the lines in Figure 5.4(d) are fits to the model prediction of Eqs. 5.14 and 5.15, with fitting parameters p_* and r_c. Ultimately the fitting provides a measurement of the Young's modulus of the PDMS material, for which we found $E_Y = 1.07 \pm 0.03$ MPa in good agreement with the elastomer we use [259]. Such a result suggests a real practical benefit of these experiments as the measurement of the Young's modulus could be done in situ for any other experiment making use of the material, provided the experiment permits to have a microchannel printed somewhere on the specimen and the lab is equipped to prepare such microchannels.

As each data point of Figure 5.4(d) represents a triplet of curves as in part (c), we also dispose of the pressure-dependent transient relaxation of these microchannels. In Figure 5.5(a) therefore, is shown the relaxation data for the 200 μm-wide microchannel also displayed in Figure 5.4. In this semi-log representation, it is clear that the relaxation is dominated by an exponential decay, the transient time constants, τ_t, being shown in the inset of the (b) part of the figure; similar relaxation times are observed considering the data from $q(t)$. The fact that these timescales depend on the pressure represents a notable departure from the preceding literature. We can consider one of the first estimates for such a relaxation time in the work of Dendukuri [237], where dimensional analysis of the lubrication equation was used to estimate a channel relaxation timescale

$$\tau_c = \frac{12\eta w L^2}{h_0^3 E_*} \ , \tag{5.16}$$

which can also be defined from the channel resistance, r_c, and its volume storage capacity $c_c = wL\partial_p h$. This timescale does not depend on the pressure, however, and thus further analysis is necessary to explain the timescale data of Figure 5.5.

In order to understand these transient relaxation times, we considered the time de-

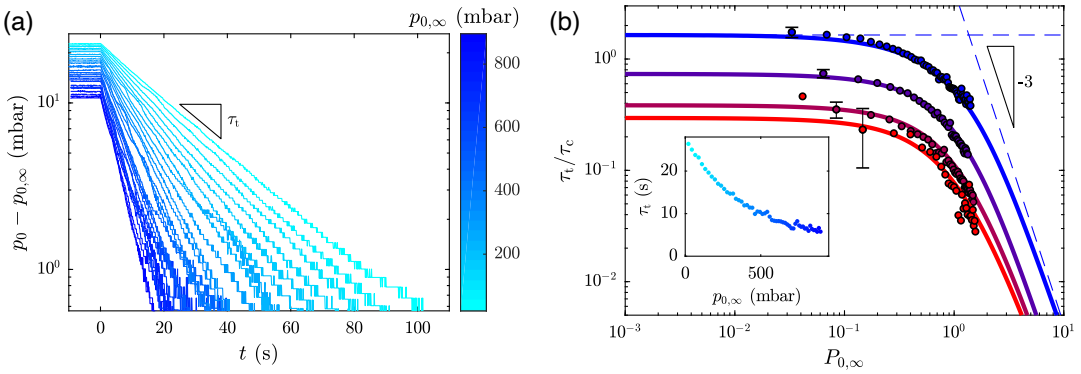

Figure 5.5: (a) For a chip with $w = 200$ μm, transient relaxation toward the steady-state pressure, $p_{0,\infty}$ at the indicated pressures in the color bar at right. (b) Normalised, transient relaxation times as a function of dimensionless pressure on log-log scales. The inset shows the fitted transient time from the raw data of part (a) with identical colour code. Reproduced from Ref. [66].

pendent lubrication equation after having introduced Eq. 5.12 to make a single equation for the spatiotemporal-dependence of the dimensionless pressure. Furthermore, we considered the time dependence as a perturbation on the steady-state pressure, with δP a function of position and time. We thus have for the pressure perturbation the linear and separable partial differential equation

$$\partial_{\tilde{T}}\delta P = \partial_{\tilde{X}}\left(\tilde{X}^{3/4}\partial_{\tilde{X}}\delta P\right) \ , \tag{5.17}$$

$$\tilde{X} = (1-X)\Pi + 1 \ , \tag{5.18}$$

$$\tilde{T} = \Pi^2 T \ , \tag{5.19}$$

where the dimensionless "tilde" variables implicate a rather strong pressure dependence through Eq 5.15. Separating variables and defining the eigenvalue series λ_k, the temporal solution of the equation is finally exponential, $\delta P_k \sim \exp(-\lambda_k \tilde{T})$, as observed in the experiments. Notably, the temporal solution contains a pressure-dependent timescale through, at a minimum, the presence of Π in the dimensional time. Additionally, of course, the eigenvalues depend on the pressure, as will be presently explained. We concern ourselves in the end with the smallest eigenvalue only, as for sufficiently long times, this term is the only one contributing to the observed, single-exponential relaxation.

Solving for the eigenvalues λ_k of the perturbation equation 5.17 requires the imposition of a debit-conserving boundary condition at the channel entrance, complimenting the relatively simple $p = 0$ condition at the exit. This condition includes notably three terms, including the resistive component of the debit measurement, a capacitive one due to the pressure measurement, and a "lubrication" term accounting for the channel entrance. Furthermore, we note without detail that the spatial solution of the perturbation equation is a position-weighted, superposition of two independent Bessel functions [260] that we call $\mathcal{C}_\nu$, ν being the order of the Bessel functions composing the superposition. The argument is proportional to the square root of the eigenvalue (*cf.* the dimensionality of the Eq. 5.17) and a power law of the dimensionless position. Imposing the boundary condition, we finally have an equation the gives the allowed eigenvalues:

$$\frac{1}{\mathcal{R}\tilde{X}_0^{3/8}}\left(\mathcal{T}\sqrt{\lambda}\Pi - \frac{1}{\sqrt{\lambda}\Pi}\right) = \frac{\mathcal{C}_{-\frac{1}{5}}\left(\frac{8}{5}\sqrt{\lambda}\tilde{X}_0^{5/8}\right)}{\mathcal{C}_{\frac{4}{5}}\left(\frac{8}{5}\sqrt{\lambda}\tilde{X}_0^{5/8}\right)} \ . \tag{5.20}$$

In this eigenvalue equation, the pressure dependence is contained in Π, and the reduced channel entrance position $\tilde{X}_0$ because of this latter's dependence on the former through, respectively, Eqs. 5.15 and 5.18. Furthermore, $\mathcal{R}$ and $\mathcal{T}$ are the channel entrance resistance, r_0/r_c and entrance timescale τ_0/τ_c with $\tau_0 = r_0 c_0$. In general, these latter entrance variables may be a function of the pressure, and in practice for our system schematised in Figure 5.4(a), the capacitance was pressure-dependent and calibrated, while the entrance resistance was constant. The first and second terms of Eq. 5.20 are thus the capacitive and resistive entrance components of the boundary condition, while the right-hand side represents the channel entrance, elastohydrodynamic lubrication flow.

Armed with Eq. 5.20 and the appropriate calibrations including those for the $\mathcal{R}$ and $\mathcal{T}$ terms, along with the steady-state analyses giving p_* and r_c, we could thus numerically solve for the transient decay times through

$$\frac{\tau_t}{\tau_c} = \frac{1}{\lambda \Pi^2} \ , \tag{5.21}$$

with λ taken as the smallest allowed value. The theoretical predictions, along with the experimental data for all chips studied are shown in Figure 5.5(b). The good agreement between the two demonstrates that soft-hydraulic relaxation times are indeed non-trivial functions of the pressure, with two asymptotic behaviours connected by a monotonic crossover.

First, a low-pressure one for which $p \ll p_*$ showing a constant time scale. Since the channel is hardly deformed in this pressure regime, there is no change in the channel resistance accompanying a change in the pressure and the relaxation time is simply proportional to the channel time τ_c accessible from dimensional analysis. Second, a large-pressure regime for which $p \gg p_*$ displays a power-law decay, $\tau_t \sim p^{-3}$. Since the pressure-debit relation is fourth order in the pressure, we can say roughly therefore that the channel resistance is third order in the pressure and with a constant channel capacitance, the p^{-3} time-scale decay is the expected one. While these asymptotic regimes are at least approached by the data, we note that the dimensionless offsets depend on the channel geometry. In fact, by considering the effect of the peripheral parameters $\mathcal{R}$ and $\mathcal{T}$, the prefactors on both of these asymptotic regimes could be derived analytically as shown in detail in Ref. [66]. The peripheries thus have a strong moderating effect on the channel relaxation times and should be considered in estimations of the channel dynamics.

Chapter 6

Conclusions and perspectives

Throughout this manuscript, we have presented a reasonably diverse set of experiments, and some complementing theory, centred on the near-surface transport of soft condensed matter. Otherwise, if it was not the soft matter that was flowing, boundaries composed of soft matter were shown in two instances to be capable of considerably influencing micro- and nano-scale flows. In the following paragraphs, we thus summarise our observations and draw several conclusions, and then present our plans for the immediate future and in the following years.

6.1 Summary and conclusions

At first, we focussed on the slip hydrodynamic boundary condition of polymer liquids. The main message in this context is that molecular-scale details —whether at the full-chain or monomer level— have the potential to modify such a boundary condition by large factors, from 10 to 100 according to our observations. Fixing the substrate and modifying the pretreatment of the substrate-facing liquid molecules, we found that a factor of nearly 10 in the effective boundary condition could be observed, attributed to chain packing or chain-end segregation effects. Concerning the substrate, it was shown that preparing a mixed-length monolayer of otherwise chemically-identical molecules can engender a factor 50 change in the slip boundary condition for short-chained polymer melts. These observations were attributed tentatively to substrate-molecular packing or a change in the electronic structure of the molecular portions facing the polymer melt. Finally, changing the surface-tension-driven equilibration mechanism, from dewetting to stepped-film leveling, we could observe a slip-length ratio as large as 100 for an identical substrate/entangled-polymer liquid pair. We interpreted this latter change as being due to transiently absorbed chains in the leveling case that did not occur in the dewetting case – in this latter the driving forces are too large for the chains to remain absorbed.

Besides making studies of how the interface can modify the boundary condition, we also investigated how the boundary condition can modify the flow domain. Using carefully prepared microdroplets, it was shown that the slip length can modify the retraction law in a microscale contact-line-motion problem. For small slip lengths, a classical, Cox-Voinov logarithmic slip length dependence is observed wherein the dissipation is concentrated near the contact line. At large slip lengths, the micro-

droplets essentially behave as a retracting, freely suspended droplet with no substrate friction – in this latter case all of the dissipation takes place throughout the droplet and there is a dependence on the equilibrium contact angle. This shift in the dissipation mode corresponds to a rather notable change in the typical intermediate free-surface shape. Large and small slip lengths, in comparison to the droplet size, both give rise to monotonic droplet shape profiles, while intermediate slip lengths may display non-monotonic interface profiles. Such an observation may be useful for a "visual" diagnosis of slip, as has been described for the case of dewetting films. Lastly, intermediate-asymptotics of thin-film morphology can also be used to diagnose the mode of relaxation, distinguishing between purely surface to full bulk flow. In the context of the glass transition anomaly for thin liquid films, these distinctions allowed us to reveal a transition between these two modes on passing through the bulk glass transition temperature. Our observations give credence to the hypothesis that free surface mobility contributes to the long-observed reductions in the glass transition temperature for thin polymer films.

We also employed evanescent-wave microscopy and particle tracking to study the boundary condition of polyelectrolyte and neutral-chain polymer solutions, with a focus on the semi-dilute regime of concentration. For the neutral-chain case, we noted that absorption of the chains on the glass-water interface could provoke the no-slip plane to move into the fluid domain; this shift corresponds with essentially the size of the molecule in solution. In contrast, chains having a similar charge to the solid-liquid interface are repelled from this surface and promote an apparent-slip boundary condition. This apparent slip is due to the reduced viscosity in the depletion zone, where water is more abundant than in the bulk. The observed apparent slip lengths could be rationalised by considering stress continuity through the depletion zone near the surface and into the bulk of the polymer solution. We thus used the semidilute scaling for the correlation length of polyelectrolytes with concentration, and the *in-situ*-measured near-surface rheology to generate a master plot of the apparent slip length as a function of the reduced viscosity of the polymer solution. Adding salt to the polymer solution had the effect of screening the back-bone charges and we observed again the neutral-chain case of adsorbed chains on the glass-water interface.

Using this same TIRFM technique, we turned our attention to the transport of near-surface colloidal particles. For this, we considered Taylor dispersion of *ca.* 100-nm particle ensembles within the evanescent zone. Pre-asymptotic Taylor dispersion, for times smaller than the one it takes a typical particle to explore the zone of observation, was found to depend sensitively on the initial distribution of particles. For initial distributions already spread across the velocity gradient, the initial dispersion is dominated by the shearing of this distribution and has linear time dependence. In contrast, for initially-peaked distributions or for times comparable to the one it takes to diffuse across the initial extent of the particle distribution, a quadratic time scaling is observed due to a continuous sampling of new velocities as particles diffuse across the velocity gradient. These observations are consistent with the unbounded Chatwin theory. At long times, a crossover into the long-time regime and a dispersion coefficient consistent with the Taylor prediction could be recovered if the height of the observation channel is chosen correctly. All of these temporal domains could also be described by a time-dependent moment theory applied to the advection-diffusion

equation.

In the pre-asymptotic Taylor dispersion study, the agreement of the experiments with theory depended on a careful observation protocol. However, such observations are not available in all nanoscale contexts. Therefore, we turned our attention to the effects of nanoscale, particle surface interactions on the long-time dispersion of the same particle ensembles described in the previous paragraph. In particular, we focussed on the electrostatic repulsion which could be controlled by tuning the salt concentration and thus the typical Debye length. Additionally, our observations are made in an open configuration for which particles can leave the observation zone, which we demonstrated is equivalent to an ideal absorption condition with concerned particles no longer contributing to the dispersion. While absorption in the polymer-slip case had the effect of reducing the slip length, we found that nanoscale dispersion —including absorption and electrostatic repulsion— could be reduced by an order of magnitude as compared to the non-interacting, tracer-particle case considered classically by Taylor. Such a reduction is due to the depletion zones built up from the two interactions on either side of the observation zone. The particle distribution controlling the dispersion was thus observed to be non-equilibrium and accessible theoretically using a novel implementation of the moment theory. In particular, a modified boundary condition gives rise to non-conserved particle number.

Lastly, we studied the effect of soft boundaries on flows in the lubrication regime, a situation which occurs particularly often in microscopic biological and micro- and nano-fluidic contexts. In a first instance we studied theoretically the effect of porosity on the classical drainage problem of Reynolds for a sphere squeezing liquid from a thin layer bounded below by a solid. First, we described the effect of a peaked force distribution on a semi-infinite, poroelastic solid. In particular, we assumed a permeable boundary for the solvent between the solid and the bath. We thus identified a short-time-incompressible and a long-time-compressible elastic response. These two asymptotic responses are connected via a diffusive spreading of the late-time response into the early-time one, emanating from the axis of rotational symmetry. Convoluting the response of the peaked force distribution to the Reynolds drainage scenario, we probed the effect of the elastic solid's porosity on this classical hydrodynamic problem. It turns out that the effect of solid porosity in this case is rather secondary to the elastic response observed in previous works. However, given that the porous materials at the focus of this theoretical study are so wide-spread in soft matter research and are furthermore conveniently fabricated, it is interesting to note that the moduli and Poisson ratio of these materials can be measured using the non-contact drainage technique. It appears that direct contact scenarios are more likely to elucidate the effects of porosity in these systems.

In a last study presented here, and complementing the previous elastohydrodynamic one, we considered the dilation of a microfluidic channel under the typical pressures applied during channel flow experiments under TIRFM. Having been motivated to use slender channels, a considerable non-linearity on the pressure-debit relation could be observed as a result of the channel deformation and resulting reduction in the hydraulic resistance. These effects having been described in the literature, our measurements served as a calibration on the following detailed study of the channels' transient relaxations. Indeed, after a sudden change in the pressure applied at the

inlet of the microfludic chip, a transient relaxation time —dependent on the pressure and varying by up to an order of magnitude— could be observed. Such transients are due to the finite drainage time of the stored liquid in the deformed microchannel. As the slenderness of the channels allows for a considerable deformation in comparison to the initial channel height, large differences in the channel resistance could be accessed, and thus large variations in the channel relaxation times. All of our observations could be rationalised in the context of a uni-dimensional lubrication theory coupled to a simple linear elasticity for the channel boundaries and including microchannel peripheries. These latter devices are common in microfluidic contexts and our analyses showed that they can have a considerable effect on the relaxation times, and thus must be considered in estimating microchannel dynamics.

Attempting to find a red line through all of these works, it could be said that tuning static structural phenomena, sometimes well-known since decades, may provoke drastic dynamical effects[1]. The order-or-magnitude reduction in Taylor dispersion at nanoscales for a few tens of nanometers variation of the effective flow channel; a similar few tens of nanometers change in the correlation length of polyelectolyte solutions giving two orders of magnitude change in the dynamical slip length, and a few angstroms change on the SAM substrates giving nearly two orders change on the solid-liquid friction coefficient. In the future, it seems therefore that the dynamical studies of soft matter, if we can harness the underlying mechanisms, could provide extremely sensitive methods to assess structural and statistical phenomenolgy. We shall elaborate on this aspect in the following perspectives.

6.2 Perspectives

The work that is planned in the lab for the next years is mainly inspired by the latter two chapters presented above, these being based on research carried out in the current home of the group. In the following pages, therefore, I will describe our projections concerning interfacial colloid transport and elastohydrodynamics. We suspect that the first projects in Section 6.2.1 described are somewhat longer term objectives, on the scale of two two four years, while those in Section 6.2.2 are ongoing experiments which show already some promising, if very recent, results. Those in the purely elastohydrodynamic perspective of Section 6.2.3 are, respectively, currently being worked out theoretically, while the latter should get moving within one year in the context of a collaboration with an industrial partner.

6.2.1 Near-surface particle tracking out of thermal equilibrium

In Chapter 4, we described our work on the rheology and solid-liquid slip boundary condition of complex fluids. Then we transitioned somewhat abruptly to the interfacial transport, coupling advection and diffusion, of colloidal particles in water, a Newtonian fluid. Implicitly, therefore, we adopted the idea that the particles in complex fluids were simply advective tracers, while they were the subject of complex interactions with the interfaces and diffusion.

[1] This idea is not fully original. Indeed, in a comment on superhydrophobicity [261], Bocquet and Lauga evoked similar opportunities in comparing structure and dynamics.

Diffusion and interactions are yet at the root of a huge number of fundamental structural and transport processes in many complex environments. A salient example is that of cellular and sub-cellular biology: these systems are mixtures containing complex macromolecules such as proteins, DNA and polysaccharides, and soft interfaces (cell walls, membranes) are never very far away. These systems are thus mainly composed of the soft matter building blocks near the soft boundaries we have studied so far. Lastly, a remarkable feature of these biological systems is that they are most often out of equilibrium.

The non-equilibrium features we have in mind are the following. In cases of flow, blood-vessel surfaces bound the fluid motion. This hydrodynamics implies viscous dissipation, and such flows may give rise to complex, non-conservative (*i.e.*, velocity-dependent) forces between particles and their surroundings [7]. Also, and essential for biology along with a huge number of industrial processes, a reservoir of chemical energy enables many functions. These include, for example, molecular synthesis, muscle contraction, ion transport, and information transfer. The work carried out in the next years will thus be aimed at investigating non-equilibrium diffusion —comprising temporal displacement and spatial distribution phenomena— under salient features described above: complex environments with hydrodynamic flow near interfaces, and with non-thermal energy reservoirs. We describe two specific projects that may be investigated in the form of questions.

How can non-conservative interactions modify the classical Gibbs-Boltzmann distribution central to soft matter statistics at equilibrium, and determining major structural and dynamical features of soft matter?

In the last few years, we have accumulated several pieces of preliminary data that motivated us to ask this question. The first is shown in Figure 6.1[Left]. There we show SIDs for 100-nm-diameter particles in ultrapure water. At low pressures ($\leqslant 30$ mbar), SIDs do not depend on the pressure applied across the microchannel. Above this pressure, significant and systematic deviations occur, demonstrating repulsion as particles are advected more strongly. Such deviations can be suppressed by adding NaCl to the driven fluid, suggesting an electrokinetic origin to the interaction [262–264]. While not shown here, we also observe dynamic signatures of hydrodynamic repulsion. Specifically, when particles are advected more strongly (x-direction), they leave the viewing area (z-direction) more quickly, roughly factor of 2 change in the residence time is observed.

As a compliment to the data in Figure 6.1[Left], we show in the [Right] part further preliminary data of particle SIDs wherein the suspending liquid was a shear-thinning, semi-dilute polyelectrolye solution [132]. For reference, the light gray curves show the pressure-independent SIDs of the 100-nm particles in water. There it is shown that, in contrast to the unsalted water solution, particles are driven toward the wall as a result of a dynamically-mediated interaction. For the moment, we do not know the rules that determine this phenomenology, but we speculate that this polymer-colloid migration scenario arises from an electro-hydrodynamical trade-off, say, between the objects in this complex mixture. Present are: negatively charged polymers, negatively charged particles, the associated counterions and a charged surface. We speculate further that the extent of the particle migration should depend

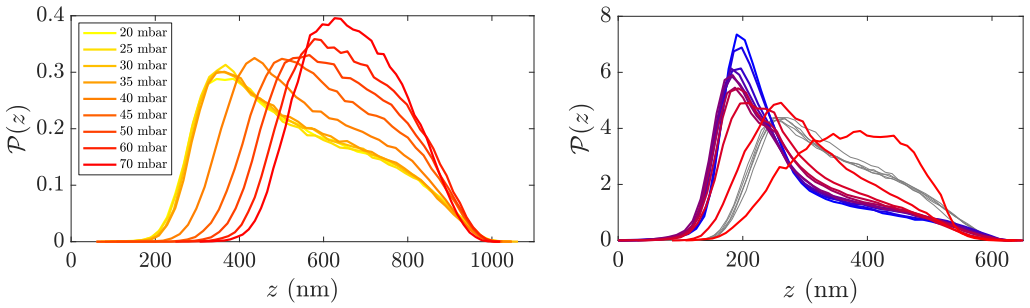

Figure 6.1: [Left] Near-wall SIDs as a function of apparent altitude for 100-nm, fluorescent nanoparticles in water. As the pressure is increased, particles are driven away from the wall. [Right] Near-wall SIDs as a function of apparent altitude for 100-nm, fluorescent nanoparticles in 1 mg/mL, anionic, 800 kg/mol hydrolyzed polyacrylamide. As the pressure is increased (from 15 mbar to 300 mbar, from red to blue), particles are driven toward the wall; grey curves show a corresponding calibration with pure water only, for pressures less than 40 mbar, *cf.* the [Left] part.

on the characteristic relaxation times of these objects in comparison to the inverse shear rates imposed on the suspension. To go further in the experimentation, and to address these hypotheses, we intend to make use of tri-color TIRFM, recently installed in the lab, and label with different fluorophores the particles and the polymer. Polyelectrolyte migration away from a wall under shear was suggested in the experiments in Refs. [201, 265] and can thus be directly tested. In any case, the result is experimentally robust[2], and opposite to the trend seen in the left part of the figure; there is thus clearly a rich non-equilibrium phenomenology at stake under this theme of non-equilibrium, velocity-dependent interactions modifying near-wall particle statistics.

As hydrodynamic lift cannot be treated as derived from a potential, the near-surface particle distributions as seen in Figures 6.1 will thus need new theoretical tools to be described. Practically, and in a time following the description of these types of systems, we would dispose of a dynamic self-assembly lever orthogonal to the typical soft-matter interactions such as those arising from the interface charges we described in Section 4.2.2.

To what extent can a tracer's diffusive motion be used to infer information about a chemical reaction, and particularly under the presence of a catalyst?

The production or degradation of chemical compounds is generally accompanied by an energy input, often thermal activation, and an energy output. The input is associated with energy barriers which, once overcome, give rise to the emission of heat for exothermic processes, this heat making up a part of the output. In order to reduce such barriers, catalysts may be used, for which an unconsumed agent is added to the reactive mixture.

To set the energy scales for such processes, we may consider typical covalent

[2]Indeed, a new collaboration with C. Barentin and M. Le Merrer show similar particle approaches for elevated pressures using polymer microgels.

bonds that have energies of order 100 kJ/mol. Such is the case, for example, in the decomposition of H_2O_2 into water and oxygen [266]. Naïvely, we can thus estimate that each such molecular decomposition corresponds to roughly $40\,kT$ of heat locally injected into, let us say, an aqueous environment. From the perspective of diffusion, with random thermal kicks normally distributed around kT, such a heat injection could in principle generate large fluctuations, 40 times larger than usual, on a nearby Brownian particle. Examining the fluctuation-dissipation relation of Eq. 1.10, we would thus expect an additional noise term to influence the fluctuations. Tuning the concentration of reactants and catalyst should allow to tune such an effect.

The hypothesis that catalysis should be observable in Brownian motion has indeed received a significant attention lately [267–273] and inspired a lively and sustained debate. Whatever mechanism could be responsible for enhanced stochastic motions, their impact is relevant to a large class of non-equilibrium systems. Whether a catalyst is propelled by liberated heat, or by the surface-tension gradient of the reactive by-products [274], to name just two possible mechanisms, the principal function of a catalyst is to "find" a reactant [275]. If its kinetics are enhanced by any mechanism, then it is pressing to both quantify such enhancement and to unravel the different possible mechanisms. As the debate of the previous paragraph stands relatively open, despite the interesting discussions in Ref. [276], a TIRFM and advection-diffusion coupling offers a new experimental protocol for unraveling such non-equilibrium diffusion situations.

The observation protocol to be developed in our lab is mainly inspired by the transport phenomena described in Sections 2.4.1 and the Taylor dispersion we investigated in Refs. [133, 134]. In first instances we will investigate the decomposition of H_2O_2 by iron oxide catalysts or in titration scenarios as was started by Mahammad Alyiev in a summer internship during 2023. The basic idea is that, using the scaling provided by Taylor, we have that $\mathcal{D}_x/D_0 \sim \mathrm{Pe}^2$, where we recall that $\mathrm{Pe} = \dot{\gamma}h^2/D_0$. If there is a small effect to be observed in the nominal diffusion coefficient D_0 due to reactivity or confinement we thus expect to see a systematic trend of this effect using the Taylor dispersion as we increase the shear rate which can be controlled carefully using microfluidics. As the normalised dispersion scales with the square of both this shear rate and the inverse square of the diffusion coefficient, Taylor dispersion will serve as an amplifier of any effect that may be present. Besides the overall effect on the dispersion and diffusion coefficients, we will also dispose of the time-dependent statistics represented by the displacement distributions in Figure 2.18. Details of such distributions should also provide clues for reactivity-modified fluctuations. Enabled to make these collective observations, we believe that our approach has the potential to make a decisive contribution to this important debate.

6.2.2 Combining Taylor dispersion with soft boundaries

At the end of the previous subsection, we noted that Taylor dispersion acts as an amplifier of diffusive effects with the possibility to tune the level of amplification by adjusting the near-wall shear rate. Given this tool, and given the last two chapters of this document along with our collaboration at the Université de Bordeaux (*i.e.* the EmetBrown team led by Thomas Salez), we will investigate in the following years the effect that soft boundaries may have on dispersive phenomena.

In a first instance, we are currently investigating the combination of the soft conduit project of Ref. [66], mainly in the steady state, with the near-wall particle tracking of Refs. [133, 134]. This natural combination of our recently developing expertise was kindly suggested by Aditya Jha (currently a postdoc at EMetBrown) who works out the theory. The experiments are following a rather simple idea which is that the Taylor dispersion is a function of the near-wall shear rate, but that in a channel deformed under elastohydrodynamic coupling, the shear rate is not a constant along the channel. Furthermore, given Eq. 5.13 and its linear proportionality to the height profile of a channel, the shear rate and thus dispersion should scale in a specific way as a function of the pressure and as a function of the position along the channel. Initial experiments performed by Masoodah Gunny (PhD) show a qualitatively correct behaviour. At a given imposed pressure, and for the position closer to the entrance, TIRFM velocimetry demonstrates that shear rates are lower than those at positions further along the channel. This is expected due to the conserved debit. Complementary dispersion data also shows that spreading is faster near the exit of the channel for a given pressure. These experiments will be pursued in the coming months, and show a flavour of coupling between soft boundaries and diffusive phenomena. In the next paragraphs, we describe a scenario in which a true coupling between a flexible boundary and Taylor dispersion may be observable.

Now we consider the soft lubrication context described in Caroline Kopecz-Muller's work of Ref. [65], and the near-surface diffusion modifications described in the introductory Section 1.1.3. For the near-wall diffusion, it was suggested in the thesis of Maxime Lavaud [277] that elastohydrodynamic lift could be provoked by diffusion. Given the instantaneous particle velocities on the order $\sqrt{kT/m}$ with m the particle mass, softness should thus be observed to impact a diffusive trajectory. Such exper-

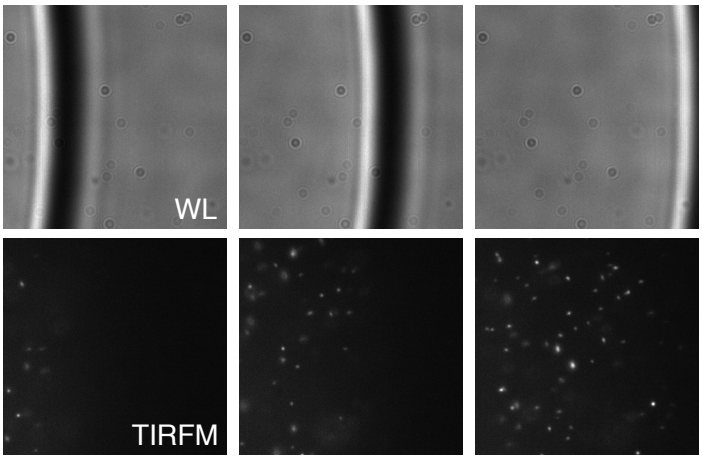

Figure 6.2: Confined microfluidic water-in-oil droplet transit (left-to-right) in a 30 μm tall, 200 μm wide channel and for images 25 μm across. [Top] White light (WL) illumination for a nearly-index-matched condition; the light/dark band indicates the droplet meniscus. [Bottom] A similar droplet, with TIRFM illumination showing fluorescent particles in the aqueous droplet. The time between images on a row is 130 ms.

iments and theory are an active area of current investigation by our collaborators in Bordeaux, and we propose a microfluidic experiment implicating Taylor dispersion that may also be able to probe such Brownian lift effects.

While not a soft elastomer, our approach in the thesis of Masoodah Gunny is to suspend our standard particles in the dispersed phase of a water-in-oil emulsion. The droplets are confined, with pancake shapes and the classical lubrication film separating the water and the glass. These films have variable thickness according to Bretherton-like scaling laws with the droplet velocity [278–281]. The selection of this height is one way of tuning an interface's effective mobility. Indeed, as seen in Eq. 2.1, where the effective film mobility could be considered to scale with h^3, a thicker film is thus more mobile and relaxes faster under the influence of surface tension as in stepped-film leveling experiments [95]. Thus, if the oil-water interface and its mobility has an influence on the diffusion, we should be able to see and tune the amplification of the effect through the shear rate inside the droplet. Preliminary tracking data suggests the velocity profiles and dispersion are measurable inside confined, advected droplets. For the moment, we simply show two image sequences in Figure 6.2 to demonstrate the proof of principle. On the top, white-light illumination of a droplet shows the meniscus transit indicated by a dark/bright band; on the bottom, a similar droplet illuminated under TIRFM progressively reveals the presence of nanoparticles. These experiments are ongoing.

6.2.3 Poroelasticity and soft hydraulics

Concerning the poroelastic materials described in Section 5.1, we noted that many researchers use poroelastic gels for applications and fluid-structure interaction investigations in microfluidics [282–284], notably using the photo-polymerisation method developed by the Doyle group [237], along with many other applications at the micro and nanoscale [258, 285] based on click chemistry. These materials, while widespread suffer from a lack of good mechanical characterisation, even while their poroelastic character has already been identified [286]. The challenge lies in the objects' typical small length scale (often a few micrometers or less), precluding traditional rheometric methods. Furthermore, the theoretical treatment, as described in the aforementioned section, may involve specialised mathematical treatments. Therefore, with Anke Lindner [282–284] we will develop parallel microfluidic and AFM-based methods for probing the poroelastic properties of such materials. The AFM methods shall be developed in my lab and follow preliminary mechanical characterisations using hydrogel materials that were developed by the Tran group [258], and inspired by previously-used microcontact mechanics methods [287]. Having also developed a custom piezo-stage that fits onto our AFM with C. Kopecz-Muller during her PhD, we expect to be capable of assessing the moduli using the oscillatory-Reynolds method of Refs. [247, 248] and Section 5.1.2, followed by direct contact experiments with the same probe for assessments of the porosity during contact loading and relaxation [287]. Such experiments will be applied to materials fabricated directly on substrates as in our collaboration with Y. Tran, or generated in microfluidic devices as in the Doyle method.

Finally, our treatment of the soft-hydraulics scenario of Section 5.2 and Ref. [66] lend themselves naturally to two parallel extensions. First, the timescale studied in

detail of the paper suggests a characteristic frequency for the microchannel. As, to give just one example, the beating heart is a periodic phenomena with soft conduits, it should be interesting to address our microfluidic problem in such an oscillatory setting. The extension of the theory provided in Section 5.2 is not so difficult, having been done in collaboration with Elie Raphaël, simply requiring many recourses to the "familiar" properties of the Bessel functions found in Ref. [260]. Our investigations have centred on the frequency-dependent penetration of the oscillatory perturbation into a microchannel, with scaling laws worked out for the small- and large-frequency limits and formidible analytic expressions connecting them. Oscillatory experiments were started by Gabriel Guyard at the end of his PhD and also followed up by Clara Notebaert during a short internship this year; more shall follow. Second, filling our microchannels with complex fluids rather than simply using water is a very exciting perspective. Fundamentally, such complex fluids will engender a new time-scale associated to the fluid, which may give rise to interesting coupling effects in the relaxation scenario of Figure 5.4(c) and may indeed provoke non-trivial boundary conditions; the playground is thus rich. In a more practical light, a new collaboration with an industrial partner interested in the application of complex liquids between soft contacts has been initiated. This partner manufactures rheologically-complex, personal-care products and is interested in such products' mechanical interaction with the substratum. We thus expect that each of the experiences of this perspective section shall be relevant and exciting avenues for our collaboration from now until the end of 2027.

Appendix A

Other works

In selecting the material to discuss in the main part of this memoire, privilege was accorded on the basis of two considerations: (*i*) completed —that is to say, published— projects were uniquely chosen; and equally importantly (*ii*) the subjects somehow fit a through line of the document. This latter consideration was particularly true for the works presented in Chapter 3, while the first consideration had very significant impact on the latter Chapter 5. In this Appendix, therefore, a brief overview of the missed works is given.

Perhaps the most exciting, and indeed most recent, work that we left off is related to the latter Chapter 5. Indeed, Caroline Kopecz-Muller (CKM) has been studying experimentally the poroelastohydrodynamics and contact mechanics of thin hydrogel films, in our collaboration with Y. Tran for the fabrication of these. This work implicates a large volume of mechanical probe testing, using AFM and surface forces apparatus; this latter SFA technique was taught to us by S. Donaldson and makes up the subject of Refs. [288, 289]. The films, ranging from 60 nm to a few microns in thickness swell under water and, complicating our analysis assuming perfectly flat films, destabilise into creasing patterns. Such patterns are at once beautiful and fascinating, and are the subject of a draft manuscript in progress. Using thin enough films, *i.e.* under 100 nm in the dry state, the surface patterns are avoided and these are the focus of mechanical testing using the aforementioned force probes. The data contains a small portion which could be described using an elastohydrodynamic theory imposing a substrate of finite thickness, worked out by CKM. After, the transition to contact mechanics of the poroelastic layer, already deformed due to the Reynolds drainage force, is currently being modelled as well. These works will make up the thesis of Ms. Kopecz-Muller to be defended in February 2024, and will be furthermore addressed by a PhD student, Zheng Liu, to start in fall 2023 along with a postdoc to begin the collaboration with Anke Lindner mentioned in the perspectives.

The collaborative adventure with Matthieu Labousse mentioned in the acknowledgements is a further exciting project implicating elasto-capillary self assembly under confined microfluidic flow. This project was initiated by us in 2021 and is currently driven by Samuel Hidalgo-Caballero (postdoc) and Grégoire Clement (2nd-year PhD). Completing this dream team, two one-year postdocs, Finn Box and Mathieu

Oléron, contributed initial efforts to getting the project off the ground. Since the project is the subject of a maturing yet delicate intellectual-property process, we unfortunately do not detail the work here. In parallel, we are filing for a patent and preparing to manuscripts that will involve the whole team, the manuscripts being led by GC and MO. This project was informed to some extent by the collaboration with M. Kerdraon, B. Dollet and M.-C. Jullien, concerning the interaction of confined microfluidic droplets [290] with the controlled deformation of narrow microfluidic channels via local heating.

A project that does not fit neatly within the scope of this document was undertaken in collaboration with F. Ogheard and T. Lopez-Leon, and was driven by Abir Wissam Boudaoud. During her thesis, perhaps the most applied work of my career, AB developed a metrologically traceable method for the measurement of debits reaching as little as 5 nanolitres per minute. Such debits are commonly used in drug delivery yet, until this thesis and the European project that served as its frame [291], were not traceable to the SI. AB's thesis led to a French national measurement standard, based on optical tracking of a meniscus through a capillary, reaching the lowest traceable flow rates to date, along with a traceable method of calibrating the capillary diameter [292].

Concerning thin polymer films and substrate friction, we identify the further works:

- McGraw *et al.* 2014, *Nanofluidics of thin polymer films: ...* [42]; a mini-review on thin-film polymer slip.
- Haefner *et al.* 2015, *Influence of slip on the Plateau-Rayleigh instability on a fibre* [293]; enhanced dynamics of a classical fluid instability due to slip.
- Fowler *et al.* 2016, *Controlling Marangoni-induced instabilities in spin-cast polymer films: How to prepare uniform films* [294]; reduced spin-coating temperature to eliminate instabilities and prepare pristine films.
- Sabsevari *et al.* 2016, *Short chains enhance slip of highly entangled polystyrenes during thin film dewetting* [295]; a study of the effect of polydispersity on slip in dewetting experiments.
- Lessel *et al.*, 2017, *Nucleated dewetting in supported ultra-thin liquid films with hydrodynamic slip* [296]; *in situ* AFM study of *ca.* 3 – 5 nm thick PS films dewetting from SAMs, showing nucleation for systems that could have been expected to dewet spinodally.
- McGraw *et al.*, 2017, *Contact dependence and velocity crossover in friction between microscopic solid/solid contacts* [297]; a microscopic study of solid-solid friction using tuning-fork AFM, demonstrating thermally-activated, velocity-dependent friction.
- Chebil *et al.*, 2018, *Influence of outer-layer finite-size effects on the dewetting dynamics of a thin polymer film embedded in an immiscible matrix* [298]; optical study of trilayer film dewetting, showing the effect of a distant no-slip condition of breakup dynamics.

Bibliography

[1] Eric Lauga, Michael Brenner, and Howard Stone. Microfluidics: The No-Slip Boundary Condition. In Cameron Tropea, Alexander L. Yarin, and John F. Foss, editors, *Springer Handbook of Experimental Fluid Mechanics*, pages 1219–1240. Springer Berlin Heidelberg, Berlin, Heidelberg, 2007.

[2] Lydéric Bocquet and Elisabeth Charlaix. Nanofluidics, from bulk to interfaces. *Chem. Soc. Rev.*, 39:1073–1095, 2010.

[3] P.G. de Gennes. *Soft Interfaces*. Cambridge University Press, 1997.

[4] Geoffrey Ingram Taylor. Dispersion of soluble matter in solvent flowing slowly through a tube. *Proceedings of the Royal Society of London. Series A. Mathematical and Physical Sciences*, 219(1137):186–203, 1953.

[5] Rutherford Aris. On the dispersion of a solute in a fluid flowing through a tube. *Proceedings of the Royal Society of London. Series A. Mathematical and Physical Sciences*, 235(1200):67–77, 1956.

[6] Howard Brenner and David A. Edwards. *Macrotransport Processes, edited by Butterworth*. Heinemann, 1993.

[7] Lionel Bureau, Gwennou Coupier, and Thomas Salez. Lift at low Reynolds number. working paper or preprint, March 2023.

[8] Ivan C Christov. Soft hydraulics: from Newtonian to complex fluid flows through compliant conduits. *Journal of Physics: Condensed Matter*, 34(6):063001, February 2022.

[9] Paul J. Flory. *Principles of Ppolymer Chemistry*. Cornell University Press, 1953.

[10] P.G. de Gennes. *Scaling Concepts in Polymer Physics*. Cornell University Press, 1979.

[11] M. Rubinstein and R.H. Colby. *Polymer Physics*. Oxford University Press, 2003.

[12] J. P. Cotton, D. Decker, H. Benoit, B. Farnoux, J. Higgins, G. Jannink, R. Ober, C. Picot, and J. des Cloizeaux. Conformation of polymer chain in the bulk. *Macromolecules*, 7(6):863–872, 1974.

[13] L. J. Fetters, D. J. Lohse, D. Richter, T. A. Witten, and A. Zirkel. Connection between polymer molecular weight, density, chain dimensions, and melt viscoelastic properties. *Macromolecules*, 27(17):4639–4647, 1994.

[14] N. Clisby. Accurate Estimate of the Critical Exponent ν for Self-Avoiding Walks via a Fast Implementation of the Pivot Algorithm. *Physical Review Letters*, 104:055702, February 2010.

[15] Andrey V. Dobrynin, Ralph H. Colby, and Michael Rubinstein. Scaling theory of polyelectrolyte solutions. *Macromolecules*, 28(6):1859–1871, 1995.

[16] Jacob Isrealachvili. *Intermolecular and Surface Forces*. Academic Press, 2011.

[17] Ralf Everaers, Sathish K Sukumaran, Gary S Grest, Carsten Svaneborg, Arvind Sivasubramanian, and Kurt Kremer. Rheology and microscopic topology of entangled polymeric liquids. *Science*, 303(5659):823–826, 2004.

[18] Martin Kröger. Shortest multiple disconnected path for the analysis of entanglements in two- and three-dimensional polymeric systems. *Computer Physics Communications*, 168(3):209–232, 2005.

[19] L.J. Fetters, D.J. Lohse, and W.W. Graessley. Chain dimensions and entanglement spacing in dense macromolecular systems. *J. Polym. Sci. Pol. Phys.*, 37:1023, 1999.

[20] R. G. Larson. *The structure and rheology of complex fluids*. Oxford University Press, 1999.

[21] R. H. Colby, D. C. Boris, W. E. Krause, and S. Dou. Shear thinning of unentangled flexible polymer liquids. *Rheologica Acta*, 46(5):569–575, May 2007.

[22] Youngsuk Heo and Ronald G. Larson. Universal scaling of linear and nonlinear rheological properties of semidilute and concentrated polymer solutions. *Macromolecules*, 41(22):8903–8915, 2008.

[23] Sharadwata Pan, Duc At Nguyen, B. Dünweg, P. Sunthar, T. Sridhar, and J. Ravi Prakash. Shear thinning in dilute and semidilute solutions of polystyrene and DNA. *Journal of Rheology*, 62(4):845–867, July 2018.

[24] S. Jouenne and B. Levache. Universal viscosifying behavior of acrylamide-based polymers used in enhanced oil recovery. *Journal of Rheology*, 64(5):1295–1313, 2020.

[25] Gert Strobl. *The Physics of Polymers*. Springer Berlin Heidelberg, Berlin, Heidelberg, 2007.

[26] J.D. Ferry. *Viscoelastic Properties of Polymers, 3rd ed.* John Wiley & Sons, Inc., 1980.

[27] Ludovic Berthier and Mark D. Ediger. Facets of glass physics. *Physics Today*, 69(1):40–46, January 2016.

[28] M. D. Ediger and J. A. Forrest. Dynamics near Free Surfaces and the Glass Transition in Thin Polymer Films: A View to the Future. *Macromolecules*, 47(2):471–478, January 2014.

[29] Simone Napolitano, Emmanouil Glynos, and Nicholas B Tito. Glass transition of polymers in bulk, confined geometries, and near interfaces. *Reports on Progress in Physics*, 80(3):036602, March 2017.

[30] Hans-Jürgen Butt, Karlheinz Graf, and Michael Kappl. *Physics and chemistry of interfaces*. Wiley-VCH Inc., 2003.

[31] P.-G. de Gennes, Françoise Brochard-Wyart, and David Quéré. *Capillarity and Wetting Phenomena: Drops, Bubbles, Pearls, Waves*. Springer, 2004.

[32] L.E. Stillwagon and R.G. Larson. Funtamentals of topographic substrate leveling. *Journal of Applied Physics*, 63:5251, 1988.

[33] L. E. Stillwagon and R. G. Larson. Leveling of thin films over uneven substrates during spin coating. *Physics of Fluids A: Fluid Dynamics*, 2(11):1937–1944, November 1990.

[34] Elke Buck, Kirstin Petersen, Markus Hund, Georg Krausch, and Diethelm Johannsmann. Decay kinetics of nanoscale corrugation gratings on polymer surface: Evidence for polymer flow below the glass temperature. *Macromolecules*, 37(23):8647–8652, November 2004. Publisher: American Chemical Society.

[35] T. Leveder, S. Landis, and L. Davoust. Reflow dynamics of thin patterned viscous films. *Applied Physics Letters*, 92(1):013107, 2008.

[36] Etienne Rognin, Stefan Landis, and Laurent Davoust. Viscosity measurements of thin polymer films from reflow of spatially modulated nanoimprinted patterns. *Physical Review E*, 84(4):041805, October 2011.

[37] K.B. Migler, H. Hervet, and L. Lèger. Slip transition of a polymer melt under shear stress. *Physical Review Letters*, 70:287, 1993.

[38] F. Brochard-Wyart, P.G. de Gennes, H. Hervet, and C. Redon. Wetting and slippage of polymer melts on semi-ideal surfaces. *Langmuir*, 10:1566, 1994.

[39] R. Fetzer, K. Jacobs, A. Münch, B. Wagner, and T.P. Witelski. New slip regimes and the shape of dewetting thin liquid films. *Physical Review Letters*, 95:127801, 2005.

[40] L. Léger, H. Hervet, and L. Bureau. Friction mechanisms at polymer-solid interfaces. *Comptes Rendus Chimie*, 9:80, 2006.

[41] O. Bäumchen, R. Fetzer, and K. Jacobs. Reduced interfacial entanglement density affects the boundary conditions of polymer flow. *Physical Review Letters*, 103:247801, 2009.

[42] Joshua D McGraw, Oliver Bäumchen, Mischa Klos, Sabrina Haefner, Matthias Lessel, Sebastian Backes, and Karin Jacobs. Nanofluidics of thin polymer films: Linking the slip boundary condition at solid–liquid interfaces to macroscopic pattern formation and microscopic interfacial properties. *Advances in colloid and interface science*, 210:13–20, 2014.

[43] Joshua D. McGraw, Tak Shing Chan, Simon Maurer, Thomas Salez, Michael Benzaquen, Elie Raphaël, Martin Brinkmann, and Karin Jacobs. Slip-mediated dewetting of polymer microdroplets. *Proceedings of the National Academy of Sciences*, 113(5):1168–1173, 2016.

[44] A. Chennevière, F. Cousin, F. Boué, E. Drockenmuller, K.R. Shull, L. Léger, and F. Restagno. Direct molecular evidence of the origin of slip of polymer melts on grafted brushes. *Macromolecules*, 49:2348, 2016.

[45] E. Secchi, S. Marbach, A. Niguès, D. Stein, A. Siria, and L. Bocquet. Massive radius-dependent flow slippage in single carbon nanotubes. *Nature*, 537:210, 2016.

[46] Zhenzhen Li, Loïc D'eramo, Choongyeop Lee, Fabrice Monti, Marc Yonger, Patrick Tabeling, Benjamin Chollet, Bruno Bresson, and Yvette Tran. Near-wall nanovelocimetry based on total internal reflection fluorescence with continuous tracking. *Journal of Fluid Mechanics*, 766:147–171, 2015.

[47] R.H. Burton, M.J. Folkes, K.A. Narh, and A. Keller. Spatial variation in viscosity in sheared polymer melts. *Journal of Materials Science*, 18:315, 1987.

[48] P.-G. de Gennes. écoulements viscométriques de polymères enchevêtrés. *C.R. Hebd. Seances Acad. Sci.: Ser. B*, 288:219, 1979.

[49] Albert Einstein. Über die von der molekularkinetischen theorie der wärme geforderte bewegung von in ruhenden flüssigkeiten suspendierten teilchen. *Annalen der Physik*, 322(8):549–560, 1905.

[50] Etienne Guyon, Jean-Pierre Hulin, Luc Petit, and Catalin D. Mitescu. *Physical Hydrodynamics*, volume 2nd. Oxford University Press, 2012.

[51] Howard Brenner. The slow motion of a sphere through a viscous fluid towards a plane surface. *Chemical engineering science*, 16(3-4):242–251, 1961.

[52] Osborne Reynolds. On the Theory of Lubrication and Its Application to Mr. Beauchamp Tower's Experiments, Including an Experimental Determination of the Viscosity of Olive Oil. *Philosophical Transactions of the Royal Society of London*, 177:157–234, 1886.

[53] Michael A. Bevan and Dennis C. Prieve. Hindered diffusion of colloidal particles very near to a wall: Revisited. *The Journal of Chemical Physics*, 113(3):1228–1236, July 2000.

[54] Luc P. Faucheux and Albert J. Libchaber. Confined brownian motion. *Physical Review E*, 49(6):5158, 1994.

[55] Eric R. Dufresne, Todd M. Squires, Michael P. Brenner, and David G. Grier. Hydrodynamic Coupling of Two Brownian Spheres to a Planar Surface. *Physical Review Letters*, 85(15):3317–3320, October 2000.

[56] Anthony Saugey, Laurent Joly, Christophe Ybert, Jean-Louis Barrat, and Lyderic Bocquet. Diffusion in pores and its dependence on boundary conditions. *Journal of Physics: Condensed Matter*, 17(49):S4075, 2005.

[57] Peter Huang and Kenneth S. Breuer. Direct measurement of anisotropic near-wall hindered diffusion using total internal reflection velocimetry. *Physical Review E*, 76(4):046307, 2007.

[58] Sang-Hyuk Lee, Yohai Roichman, Gi-Ra Yi, Shin-Hyun Kim, Seung-Man Yang, Alfons van Blaaderen, Peter van Oostrum, and David G. Grier. Characterizing and tracking single colloidal particles with video holographic microscopy. *Optics Express*, 15(26):18275, December 2007.

[59] Prerna Sharma, Shankar Ghosh, and S. Bhattacharya. A high-precision study of hindered diffusion near a wall. *Applied Physics Letters*, 97(10):104101, September 2010.

[60] Maxime Lavaud, Thomas Salez, Yann Louyer, and Yacine Amarouchene. Stochastic inference of surface-induced effects using brownian motion. *Phys. Rev. Research*, 3:L032011, Jul 2021.

[61] Patrick Tabeling. *Introduction to microfluidics*. Oxford University Press, 2005.

[62] Henrik Bruus. *Theoretical Microfluidics*. Oxford University Press, 2008.

[63] Alexander Oron, Stephen H Davis, and S George Bankoff. Long-scale evolution of thin liquid films. *Reviews of modern physics*, 69(3):931, 1997.

[64] Herbert E. Huppert. Flow and instability of a viscous current down a slope. *Nature*, 300(5891):427–429, December 1982.

[65] Caroline Kopecz-Muller, Vincent Bertin, Elie Raphaël, Joshua D. McGraw, and Thomas Salez. Mechanical response of a thick poroelastic gel in contactless colloidal-probe rheology. *Proceedings of the Royal Society A: Mathematical, Physical and Engineering Sciences*, 479(2271):20220832, March 2023. Publisher: Royal Society.

[66] Gabriel Guyard, Frédéric Restagno, and Joshua D. McGraw. Elastohydrodynamic relaxation of a soft and deformable microchannel. *hal-03719718*, 2022.

[67] Younan Xia and George M. Whitesides. Soft Lithography. *Angewandte Chemie International Edition*, 37(5):550–575, 1998.

[68] Jacob Sagiv. Organized monolayers by adsorption. 1. Formation and structure of oleophobic mixed monolayers on solid surfaces. *Journal of the American Chemical Society*, 102(1):92–98, January 1980. Publisher: American Chemical Society.

[69] Stephen R. Wasserman, George M. Whitesides, Ian M. Tidswell, Ben M. Ocko, Peter S. Pershan, and John D. Axe. The structure of self-assembled monolayers of alkylsiloxanes on silicon: a comparison of results from ellipsometry and low-angle x-ray reflectivity. *Journal of the American Chemical Society*, 111(15):5852–5861, July 1989. Publisher: American Chemical Society.

[70] P. Silberzan, L. Leger, D. Ausserre, and J. J. Benattar. Silanation of silica surfaces. A new method of constructing pure or mixed monolayers. *Langmuir*, 7(8):1647–1651, August 1991. Publisher: American Chemical Society.

[71] Frank Schreiber. Structure and growth of self-assembling monolayers. *Progress in Surface Science*, 65(5-8):151–257, November 2000.

[72] J. Christopher Love, Lara A. Estroff, Jennah K. Kriebel, Ralph G. Nuzzo, and George M. Whitesides. Self-Assembled Monolayers of Thiolates on Metals as a Form of Nanotechnology. *Chemical Reviews*, 105(4):1103–1170, April 2005. Publisher: American Chemical Society.

[73] Philipp Gutfreund, Oliver Bäumchen, Renate Fetzer, Dorothee van der Grinten, Marco Maccarini, Karin Jacobs, Hartmut Zabel, and Max Wolff. Solid surface structure affects liquid order at the polystyrene–self-assembled-monolayer interface. *Physical Review E*, 87(1):012306, January 2013. Publisher: American Physical Society.

[74] M. Lessel, O. Bäumchen, M. Klos, H. Hähl, R. Fetzer, M. Paulus, R. Seemann, and K. Jacobs. Self-assembled silane monolayers: an efficient step-by-step recipe for high-quality, low energy surfaces. *Surface and Interface Analysis*, 47(5):557–564, May 2015.

[75] Juan Manuel Castillo, Mischa Klos, Karin Jacobs, Martin Horsch, and Hans Hasse. Characterization of Alkylsilane Self-Assembled Monolayers by Molecular Simulation. *Langmuir*, 31(9):2630–2638, March 2015. Publisher: American Chemical Society.

[76] M. Tolan. *X-Ray Scattering from Soft-Matter Thin Films*. Springer, 1999.

[77] O. Bäumchen, R. Fetzer, M. Klos, M. Lessel, L. Marquant, H. Hähl, and K. Jacobs. Slippage and nanorheology of thin liquid polymer films. *Journal of Physics: Condensed Matter*, 24:325102, 2012.

[78] Joseph J. Jasper. The Surface Tension of Pure Liquid Compounds. *Journal of Physical and Chemical Reference Data*, 1(4):841–1010, October 1972.

[79] Alfred G. Emslie, Francis T. Bonner, and Leslie G. Peck. Flow of a Viscous Liquid on a Rotating Disk. *Journal of Applied Physics*, 29(5):858–862, May 1958.

[80] David B. Hall, Patrick Underhill, and John M. Torkelson. Spin coating of thin and ultrathin polymer films. *Polymer Engineering & Science*, 38(12):2039–2045, December 1998.

[81] Stefan Karpitschka, Constans M. Weber, and Hans Riegler. Spin casting of dilute solutions: Vertical composition profile during hydrodynamic-evaporative film thinning. *Chemical Engineering Science*, 129:243–248, June 2015.

[82] Lun Si, Michael V. Massa, Kari Dalnoki-Veress, Hugh R. Brown, and Richard A. L. Jones. Chain Entanglement in Thin Freestanding Polymer Films. *Physical Review Letters*, 94(12):127801, April 2005.

[83] H. Bodiguel and C. Fretigny. Reduced Viscosity in Thin Polymer Films. *Physical Review Letters*, 97:266105, 2006.

[84] O. Bäumchen, R. Fetzer, and K. Jacobs. Reduced Interfacial Entanglement Density Affects the Boundary Conditions of Polymer Flow. *Physical Review Letters*, 103(24):247801, December 2009.

[85] Keewook Paeng, Stephen F. Swallen, and M. D. Ediger. Direct Measurement of Molecular Motion in Freestanding Polystyrene Thin Films. *Journal of the American Chemical Society*, 133(22):8444–8447, June 2011.

[86] Cynthia Bukowski, Tianren Zhang, Robert A. Riggleman, and Alfred J. Crosby. Load-bearing entanglements in polymer glasses. *Science Advances*, 7(38):eabg9763, 2021.

[87] J. A. Forrest, K. Dalnoki-Veress, J. R. Stevens, and J. R. Dutcher. Effect of Free Surfaces on the Glass Transition Temperature of Thin Polymer Films. *Physical Review Letters*, 77(10):2002–2005, September 1996. Publisher: American Physical Society.

[88] A. Karim, G. P. Felcher, and T. P. Russell. Interdiffusion of Polymers at Short Times. *Macromolecules*, 27(23):6973–6979, November 1994.

[89] Christopher J. Ellison and John M. Torkelson. The distribution of glass-transition temperatures in nanoscopically confined glass formers. *Nature Materials*, 2(10):695–700, October 2003. Number: 10 Publisher: Nature Publishing Group.

[90] Jiangshui Huang, Megan Juszkiewicz, Wim H. de Jeu, Enrique Cerda, Todd Emrick, Narayanan Menon, and Thomas P. Russell. Capillary Wrinkling of Floating Thin Polymer Films. *Science*, 317(5838):650–653, August 2007.

[91] Joshua D. McGraw, Jianfeng Li, David L. Tran, An-Chang Shi, and Kari Dalnoki-Veress. Plateau-rayleigh instability in a torus: formation and breakup of a polymer ring. *Soft Matter*, 6(6):1258–1262, 2010.

[92] Omar Al-Khayat, Kieran Geraghty, Keyun Shou, Andrew Nelson, and Chiara Neto. Chain Collapse and Interfacial Slip of Polystyrene Films in Good/Nonsolvent Vapor Mixtures. *Macromolecules*, 49(4):1344–1352, February 2016.

[93] Omar Al-Khayat, Jun Ki Hong, Kieran Geraghty, and Chiara Neto. "The Good, the Bad, and the Slippery": A Tale of Three Solvents in Polymer Film Dewetting. *Macromolecules*, 49(17):6590–6598, September 2016.

[94] Sara L Cormier, Joshua D. McGraw, Thomas Salez, Elie Raphaël, and Kari Dalnoki-Veress. Beyond tanner's law: Crossover between spreading regimes of a viscous droplet on an identical film. *Physical review letters*, 109(15):154501, 2012.

[95] Joshua D. McGraw, Thomas Salez, Oliver Bäumchen, Elie Raphaël, and Kari Dalnoki-Veress. Self-similarity and energy dissipation in stepped polymer films. *Physical Review Letters*, 109(12):128303, 2012.

[96] Joshua D. McGraw, Nicholas M. Jago, and Kari Dalnoki-Veress. Capillary levelling as a probe of thin film polymer rheology. *Soft Matter*, 7(17):7832–7838, 2011.

[97] O S Heavens. Optical properties of thin films. *Reports on Progress in Physics*, 23(1):1–65, January 1960.

[98] G.I. Barenblatt. *Scaling*. Cambridge University Press, 2003.

[99] Thomas Salez, Joshua D. McGraw, Sara L. Cormier, Oliver Bäumchen, Kari Dalnoki-Veress, and Elie Raphaël. Numerical solutions of thin-film equations for polymer flows. *The European Physical Journal E*, 35(11):1–9, 2012.

[100] Joshua D. McGraw, Thomas Salez, Oliver Bäumchen, Elie Raphaël, and Kari Dalnoki-Veress. Capillary leveling of stepped films with inhomogeneous molecular mobility. *Soft Matter*, 9(34):8297–8305, 2013.

[101] Oliver Bäumchen, Michael Benzaquen, Thomas Salez, Joshua D. McGraw, Matilda Backholm, Paul Fowler, Elie Raphaël, and Kari Dalnoki-Veress. Relaxation and intermediate asymptotics of a rectangular trench in a viscous film. *Physical Review E*, 88(3):035001, 2013.

[102] Matilda Backholm, Michael Benzaquen, Thomas Salez, Elie Raphaël, and Kari Dalnoki-Veress. Capillary levelling of a cylindrical hole in a viscous film. *Soft Matter*, 10:2550–2558, 2014.

[103] Vincent Bertin, John Niven, Howard A. Stone, Thomas Salez, Elie Raphaël, and Kari Dalnoki-Veress. Symmetrization of Thin Freestanding Liquid Films via a Capillary-Driven Flow. *Physical Review Letters*, 124(18):184502, May 2020. Publisher: American Physical Society.

[104] Thomas Salez, Joshua D. McGraw, Oliver Bäumchen, Kari Dalnoki-Veress, and Elie Raphaël. Capillary-driven flow induced by a stepped perturbation atop a viscous film. *Physics of Fluids*, 24(10):102111, 2012.

[105] F. Brochard-Wyart and J. Daillant. Drying of solids wetted by thin liquid films. *Canadian Journal of Physics*, 68:1084, 1990.

[106] G. Reiter. Dewetting of thin polymer films. *Physical Review Letters*, 68:75, 1992.

[107] G. Debrégas, P. Martin, and F. Brochard-Wyart. Viscous bursting of suspended films. *Physical Review Letters*, 75:3886, 1995.

[108] G. Reiter and R. Khanna. Kinetics of autophobic dewetting of polymer films. *Langmuir*, 16:6351, 2000.

[109] R. Seemann, S. Herminghaus, and K. Jacobs. Shape of a liquid front upon dewetting. *Physical Review Letters*, 87:196101, 2001.

[110] R. Seemann, S. Herminhaus, and K. Jacobs. Dewetting patterns and molecular forces: A reconciliation. *Physical Review Letters*, 86:5534, 2001.

[111] G. Reiter, M. Hamieh, P. Damman, S. Sclavons, S. Gabriele, T. Vilmin, and E. Raphaël. Residual stresses in thin polymer films cause rupture and dominate early stages of dewetting. *Nature Materials*, 4:754, 2005.

[112] R. Seemann, S. Herminghaus, C. Neto, S. Schlagowski, D. Podzimek, R. Konrad, H. Mantz, and K. Jacobs. Dynamics and structure formation in thin polymer melt films. *Journal of Physics: Condensed Matter*, 17:S267, 2005.

[113] G. Reiter. *Soft Matter Characterization*, chapter 25: Visualizing Properties of Polymers at Interfaces. Springer-Verlag, 2008.

[114] G. Reiter, S. Al Akhrass, M. Hamier, P. Damman, S. Gabriele, T. Vilmin, and E. Raphaël. Dewetting as an investigative tool for studying properties of thin polymer films. *The Eurpoean Physical Journal: Special Topics*, 166:165, 2009.

[115] C. Redon, F. Brochard-Wyart, and F. Rondelez. Dynamics of dewetting. *Physical Review Letters*, 66:715, 1991.

[116] K. Jacobs, R. Seemann, G. Schatz, and S. Herminghaus. Growth of holes in liquid films with partial slippage. *Langmuir*, 14:4961, 1998.

[117] P.G. de Gennes. Wetting: Statics and Dynamics. *Reviews of Modern Physics*, 57:827, 1985.

[118] R. Fetzer and K. Jacobs. Slippage of newtonian liquids: Influence on the dynamics of dewetting thin films. *Langmuir*, 23:11617, 2007.

[119] S. Mostafa Sabzevari, Joshua D. McGraw, and Paula Wood-Adams. Short chains enhance slip of highly entangled polystyrenes during thin film dewetting. *RSC Adv.*, 6:91163–91170, 2016.

[120] A. Münch, B. Wagner, and T.P. Witelski. Lubrication models with small to large slip lengths. *Journal of Engineering Mathematics*, 53:359, 2005.

[121] R. Fetzer, A. Münch, B. Wagner, M. Rauscher, and K. Jacobs. Quantifying hydrodynamic slip: A comprehensive analysis of dewetting profiles. *Langmuir*, 23:10559, 2007.

[122] O. Bäumchen, R. Fetzer, A. Münch, B. Wagner, and K. Jacobs. Comprehensive analysis of dewetting profiles to quantify hydrodynamic slip. In *IUTAM Symposium on Advances in Micro- and Nanofluidic*, page 51. Springer, 2009.

[123] Daniel Axelrod, Nancy L Thompson, and Thomas P Burghardt. Total internal reflection fluorescent microscopy. *Journal of microscopy*, 129(1):19–28, 1983.

[124] Daniel Axelrod. Total internal reflection fluorescence microscopy. *Methods in cell biology*, 30:245–270, 1989.

[125] Brian D Reed, Michael J Meyer, Valentin Abramzon, Omer Ad, Pat Adcock, Faisal R Ahmad, Gün Alppay, James A Ball, James Beach, Dominique Belhachemi, Anthony Bellofiore, Michael Bellos, Juan Felipe Beltrán, Andrew Betts, Mohammad Wadud Bhuiya, Kristin Blacklock, Robert Boer, David Boisvert, Norman D Brault, Aaron Buxbaum, Steve Caprio, Changhoon Choi, Thomas D Christian, Robert Clancy, Joseph Clark, Thomas Connolly, Kathren Fink Croce, Richard Cullen, Mel Davey, Jack Davidson, Mohamed M Elshenawy, Michael Ferrigno, Daniel Frier, Saketh Gudipati, Stephanie Hamill, Zhaoyu He, Sharath Hosali, Haidong Huang, Le Huang, Ali Kabiri, Gennadiy Kriger, Brittany Lathrop, An Li, Peter Lim, Stephen Liu, Feixiang Luo, Caixia Lv, Xiaoxiao Ma, Evan McCormack, Michele Millham, Roger Nani, Manjula Pandey, John Parillo, Gayatri Patel, Douglas H Pike, Kyle Preston, Adeline Pichard-Kostuch, Kyle Rearick, Todd Rearick, Marco Ribezzi-Crivellari, Gerard Schmid, Jonathan Schultz, Xinghua Shi, Badri Singh, Nikita Srivastava, Shannon F Stewman, T R Thurston, Philip Trioli, Jennifer Tullman, Xin Wang, Yen-Chih Wang, Eric A G Webster, Zhizhuo Zhang, Jorge Zuniga, Smita S Patel, Andrew D Griffiths, Antoine M van Oijen, Michael McKenna, Matthew D Dyer, and Jonathan M Rothberg. Real-time dynamic single-molecule protein sequencing on an integrated semiconductor device. *Science*, 378:186–192, 2022.

[126] Dennis C. Prieve. Measurement of colloidal forces with TIRM. *Advances in Colloid and Interface Science*, 82(1-3):93–125, 1999.

[127] Peter Huang, Jeffrey S. Guasto, and Kenneth S. Breuer. Direct measurement of slip velocities using three-dimensional total internal reflection velocimetry. *Journal of Fluid Mechanics*, 566:447–464, 2006.

[128] Peter Huang and Kenneth S. Breuer. Direct measurement of anisotropic near-wall hindered diffusion using total internal reflection velocimetry. *Physical Review E*, 76(4):046307, 2007.

[129] M. Yoda and Yutaka Kazoe. Dynamics of suspended colloidal particles near a wall: Implications for interfacial particle velocimetry. *Physics of Fluids*, 23(11):111301, 2011.

[130] Paul R Selvin, Tyler Lougheed, M Tonks Hoffman, Hyokeun Park, Hamza Balci, Benjamin H Blehm, and Erdal Toprak. *Single-Molecule Techniques: A Laboratory Manual*, chapter 3: In vitro and in vivo FIONA and other acronyms for watching molecular motors walk, pages 37–71. Cold Spring Harbor Laboratory Press, 2008.

[131] Kenneth N. Fish. Total internal reflection fluorescence (TIRF) microscopy. *Current Protocols in Cytometry*, 50(1):12–18, 2009.

[132] Gabriel Guyard, Alexandre Vilquin, Nicolas Sanson, Stéphane Jouenne, Frederic Restagno, and Joshua D. McGraw. Near-surface rheology and hydrodynamic boundary condition of semi-dilute polymer solutions. *Soft Matter*, 17(14):3765–3774, 2021.

[133] Alexandre Vilquin, Vincent Bertin, Pierre Soulard, Gabriel Guyard, Elie Raphaël, Frederic Restagno, Thomas Salez, and Joshua D. McGraw. Time dependence of advection-diffusion coupling for nanoparticle ensembles. *Physical Review Fluids*, 6(6):064201, 2021.

[134] Alexandre Vilquin, Vincent Bertin, Elie Raphaël, David S. Dean, Thomas Salez, and Joshua D. McGraw. Nanoparticle taylor dispersion near charged surfaces with an open boundary. *Physical Review Letters*, 130:038201, 2023.

[135] Gabriel Guyard. *Near-surface transport of polymer solutions and time-dependent soft microfluidics*. PhD thesis, Université Paris-Saclay, December 2022.

[136] Lukas Novotny and Bert Hecht. *Principles of nano-optics*. Cambridge University Press, Cambridge ; New York, 2006.

[137] C. I. Bouzigues, P. Tabeling, and L. Bocquet. Nanofluidics in the Debye layer at hydrophilic and hydrophobic surfaces. *Physical Review Letters*, 101(11):114503, 2008.

[138] K. D. Kihm, A. Banerjee, C. K. Choi, and T. Takagi. Near-wall hindered Brownian diffusion of nanoparticles examined by three-dimensional ratiometric total internal reflection fluorescence microscopy (3-D R-TIRFM). *Experiments in Fluids*, 37(6):811–824, December 2004.

[139] Xu Zheng, Fei Shi, and Zhanhua Silber-Li. Study on the statistical intensity distribution (SID) of fluorescent nanoparticles in TIRFM measurement. *Microfluidics and Nanofluidics*, 22(11):127, 2018.

[140] R. Sadr, H. Li, and M. Yoda. Impact of hindered Brownian diffusion on the accuracy of particle-image velocimetry using evanescent-wave illumination. *Experiments in Fluids*, 38:90–98, 2005.

[141] Mark Ilton, Thomas Salez, Paul D. Fowler, Marco Rivetti, Mohammed Aly, Michael Benzaquen, Joshua D. McGraw, Elie Raphaël, Kari Dalnoki-Veress, and Oliver Bäumchen. Adsorption-induced slip inhibition for polymer melts on ideal substrates. *Nature communications*, 9(1):1–7, 2018.

[142] Joshua D. McGraw, Mischa Klos, Antoine Bridet, Hendrik Hähl, Michael Paulus, Juan Manuel Castillo, Martin Horsch, and Karin Jacobs. Influence of bidisperse self-assembled monolayer structure on the slip boundary condition of thin polymer films. *The Journal of Chemical Physics*, 146(20):203326, 2017.

[143] S. Mostafa Sabzevari, Joshua D. McGraw, Karin Jacobs, and Paula Wood-Adams. Sacrificial mica substrates influence the slip boundary condition of dewetting polymer films. *Polymer*, 78:202–207, 2015.

[144] A. Münch, B. A. Wagner, and T. P. Witelski. Lubrication Models with Small to Large Slip Lengths. *Journal of Engineering Mathematics*, 53(3-4):359–383, December 2005.

[145] David R. Barbero and Ullrich Steiner. Nonequilibrium Polymer Rheology in Spin-Cast Films. *Physical Review Letters*, 102(24):248303, June 2009.

[146] Adam Raegen, Mithun Chowdhury, Christophe Calers, Alexander Schmatulla, Ullrich Steiner, and Günter Reiter. Aging of Thin Polymer Films Cast from a Near-Theta Solvent. *Physical Review Letters*, 105(22):227801, November 2010.

[147] Joshua D. McGraw, Paul D. Fowler, Melissa L. Ferrari, and Kari Dalnoki-Veress. Relaxation of non-equilibrium entanglement networks in thin polymer films. *The European Physical Journal E*, 36(1):1–8, 2013.

[148] F Brochard-Wyart, C Gay, and Pierre-Gilles de Gennes. Slippage of Polymer Melts on Grafted Surfaces. *Macromolecules*, 29(1):377–382, 1996.

[149] L. Léger, H. Hervet, G. Massey, and E. Durliat. Wall slip in polymer melts. *J. Phys.: Condens. Matter*, 9(37):7719, 1997.

[150] Liliane Léger, Elie Raphaël, and Hubert Hervet. Surface-Anchored Polymer Chains: Their Role in Adhesion and Friction. In S. Granick, K. Binder, P.-G. de Gennes, E. P. Giannelis, G. S. Grest, H. Hervet, R. Krishnamoorti, L. Léger, E. Manias, E. Raphaël, and S.-Q. Wang, editors, *Polymers in Confined Environments*, Advances in Polymer Science, pages 185–225. Springer, Berlin, Heidelberg, 1999.

[151] Marceau Hénot, Eric Drockenmuller, Liliane Léger, and Frédéric Restagno. Sensing adsorption kinetics through slip velocity measurements of polymer melts. *The European Physical Journal E*, 41(7):83, July 2018.

[152] Marceau Hénot, Marion Grzelka, Jian Zhang, Sandrine Mariot, Iurii Antoniuk, Eric Drockenmuller, Liliane Léger, and Frédéric Restagno. Temperature-Controlled Slip of Polymer Melts on Ideal Substrates. *Physical Review Letters*, 121(17):177802, October 2018.

[153] Benjamin Cross, Chloé Barraud, Cyril Picard, Liliane Léger, Frédéric Restagno, and Élisabeth Charlaix. Wall slip of complex fluids: Interfacial friction versus slip length. *Physical Review Fluids*, 3(6):062001, June 2018. Publisher: American Physical Society.

[154] Chloé Barraud, Benjamin Cross, Cyril Picard, Fréderic Restagno, Lilianne Léger, and Elisabeth Charlaix. Large slippage and depletion layer at the polyelectrolyte/solid interface. *Soft Matter*, 15(31):6308–6317, 2019.

[155] Oliver Bäumchen, Ludovic Marquant, Ralf Blossey, Andreas Münch, Barbara Wagner, and Karin Jacobs. Influence of Slip on the Rayleigh-Plateau Rim Instability in Dewetting Viscous Films. *Physical Review Letters*, 113(1):014501, July 2014.

[156] Dirk Peschka, Sabrina Haefner, Ludovic Marquant, Karin Jacobs, Andreas Münch, and Barbara Wagner. Signatures of slip in dewetting polymer films. *Proceedings of the National Academy of Sciences*, 116(19):9275–9284, May 2019. Publisher: Proceedings of the National Academy of Sciences.

[157] Yu Chai, Thomas Salez, Joshua D McGraw, Michael Benzaquen, Kari Dalnoki-Veress, Elie Raphaël, and James A Forrest. A direct quantitative measure of surface mobility in a glassy polymer. *Science*, 343(6174):994–999, 2014.

[158] J. L Keddie, R. A. L Jones, and R. A Cory. Size-Dependent Depression of the Glass Transition Temperature in Polymer Films. *Europhysics Letters (EPL)*, 27(1):59–64, July 1994.

[159] William W. Mullins. Flattening of a Nearly Plane Solid Surface due to Capillarity. *Journal of Applied Physics*, 30(1):77–83, January 1959.

[160] James A. Forrest and Johan Mattsson. Reductions of the glass transition temperature in thin polymer films: Probing the length scale of cooperative dynamics. *Physical Review E*, 61(1):R53–R56, January 2000.

[161] O. Bäumchen, J. D. McGraw, J. A. Forrest, and K. Dalnoki-Veress. Reduced Glass Transition Temperatures in Thin Polymer Films: Surface Effect or Artifact? *Physical Review Letters*, 109(5):055701, August 2012.

[162] Tak Shing Chan, Joshua D. McGraw, Thomas Salez, Ralf Seemann, and Martin Brinkmann. Morphological evolution of microscopic dewetting droplets with slip. *Journal of Fluid Mechanics*, 828:271–288, 2017.

[163] L.H. Tanner. The spreading of silicone oil drops on horizontal surfaces. *Journal of Physics D: Applied Physics*, 12:1473, 1979.

[164] O. V. Voinov. Hydrodynamics of wetting. *Fluid Dynamics*, 11(5):714–721, 1977.

[165] R. G. Cox. The dynamics of the spreading of liquids on a solid surface. Part 1. Viscous flow. *Journal of Fluid Mechanics*, 168:169–194, July 1986. Publisher: Cambridge University Press.

[166] Tak Shing Chan, Catherine Kamal, Jacco H. Snoeijer, James E. Sprittles, and Jens Eggers. Cox–Voinov theory with slip. *Journal of Fluid Mechanics*, 900:A8, October 2020. Publisher: Cambridge University Press.

[167] C. Huh and L.E. Scriven. Hydrodynamic model of steady movement of a solid/liquid/fluid contact line. *Journal of Colloid and Interface Science*, 35:85, 1971.

[168] F. Heslot, A.M. Cazabat, and N. Fraysse. Diffusion-controlled wetting films. *Journal of Physics: Condensed Matter*, 1:5793, 1989.

[169] A. Hoang and H. P. Kavehpour. Dynamics of nanoscale precursor film near a moving contact line of spreading drops. *Physical Review Letters*, 106:254501, 2011.

[170] Claire Schune, Marc Yonger, Bruno Bresson, Christian Fretigny, Laurent Guy, Thomas Chaussée, François Lequeux, Hélène Montes, and Emilie Verneuil. Combining Ellipsometry and AFM To Probe Subnanometric Precursor Film Dynamics of Polystyrene Melts. *Langmuir*, 35(24):7727–7734, June 2019.

[171] Claire Schune, Marc Yonger, Mohamed Hanafi, Jürgen Thiel, Laurent Guy, Thomas Chaussée, François Lequeux, Hélène Montes, and Emilie Verneuil. Rouse 2d diffusion of polymer chains in low density precursor films of polybutadiene melts. *ACS Macro Letters*, 9(6):843–848, 2020. PMID: 35648516.

[172] E.B. Dussan V. and S.H. Davis. On the motion of a fluid-fluid interface along a solid surface. *Journal of Fluid Mechanics*, 65:71, 1974.

[173] H. B. van Lengerich and P. H. Steen. Energy dissipation and the contact-line region of a spreading bridge. *Journal of Fluid Mechanics*, 703:111, 2012.

[174] D.N. Sibley, A. Nold, N. Savva, and S. Kalliadasis. A comparison of slip, disjoining pressure, and interface formation models for contact line motion through asymptotic analysis of thin two-dimensional droplet spreading. *Journal of Engineering Mathematics*, DOI: 10.1007/s10665-014-9702-9, 2014.

[175] C. Pozrikidis. *A practical guide to boundary element methods with the software library BEMLIB*. Chapman & Hall/CRC, Boca Raton, 2002.

[176] Joshua D. Mcgraw, Mischa Klos, Antoine Bridet, Hendrik Hähl, Michael Paulus, Juan Manuel Castillo, Martin Horsch, and Karin Jacobs. Influence of bidisperse self-assembled monolayer structure on the slip boundary condition of thin polymer films. *The Journal of Chemical Physics*, 146(20):203326, 2017.

[177] M. Lestelius, I. Engquist, P. Tengvall, M.K. Chaudhury, and B. Liedberg. Order/disorder gradients of n-alkanethiols on gold. *Colloids and Surfaces B: Biointerfaces*, 15:57, 1999.

[178] Mischa Klos. *Exploring the Boundary Condition of Polymeric Liquids*. PhD thesis, Universität des Saarlandes, 2016.

[179] A. Schallamach. A theory of dynamic rubber friction. *Wear*, 6:375, 1963.

[180] A Silberberg. Distribution of conformations and chain ends near the surface of a melt of linear flexible macromolecules. *Journal of Colloid and Interface Science*, 90(1):86–91, November 1982.

[181] Hugh R. Brown and Thomas P. Russell. Entanglements at Polymer Surfaces and Interfaces. *Macromolecules*, 29(2):798–800, January 1996.

[182] Ting Ge, Flint Pierce, Dvora Perahia, Gary S. Grest, and Mark O. Robbins. Molecular Dynamics Simulations of Polymer Welding: Strength from Interfacial Entanglements. *Physical Review Letters*, 110(9):098301, February 2013.

[183] M. W. Matsen and P. Mahmoudi. Segregation of chain ends to the surface of a polymer melt. *The European Physical Journal E*, 37(8):78, August 2014.

[184] Arvind Hariharan, Sanat K. Kumar, Miriam H. Rafailovich, Jonathan Sokolov, X. Zheng, Daihung Duong, Steven A. Schwarz, and Thomas P. Russell. The effect of finite film thickness on the surface segregation in symmetric binary polymer mixtures. *The Journal of Chemical Physics*, 99(1):656–663, July 1993.

[185] Arvind Hariharan, Sanat K. Kumar, and Thomas P. Russell. Free surfaces of polymer blends. II. Effects of molecular weight and applications to asymmetric polymer blends. *The Journal of Chemical Physics*, 99(5):4041–4050, September 1993.

[186] Arvind Hariharan, Sanat K. Kumar, and Thomas P. Russell. Surface segregation in binary polymer mixtures: a lattice model. *Macromolecules*, 24(17):4909–4917, August 1991.

[187] Kostas Ch. Daoulas, Vagelis A. Harmandaris, and Vlasis G. Mavrantzas. Detailed Atomistic Simulation of a Polymer Melt/Solid Interface: Structure, Density, and Conformation of a Thin Film of Polyethylene Melt Adsorbed on Graphite. *Macromolecules*, 38(13):5780–5795, June 2005.

[188] D Hudzinskyy and A V Lyulin. Confinement and shear effects for atactic polystyrene film structure and mechanics. *Modelling and Simulation in Materials Science and Engineering*, 19(7):074007, October 2011.

[189] Marceau Hénot, Eric Drockenmuller, Liliane Léger, and Frédéric Restagno. Friction of Polymers: from PDMS Melts to PDMS Elastomers. *ACS Macro Letters*, 7(1):112–115, January 2018. Publisher: American Chemical Society.

[190] Marceau Hénot, Alexis Chennevière, Eric Drockenmuller, Liliane Léger, and Frédéric Restagno. Comparison of the slip of a pdms melt on weakly adsorbing surfaces measured by a new photobleaching-based technique. *Macromolecules*, 50(14):5592–5598, 2017.

[191] Marion Grzelka, Iurii Antoniuk, Eric Drockenmuller, Alexis Chennevière, Liliane Léger, and Fr'ed'eric Restagno. Viscoelasticity-induced onset of slip at the wall for polymer fluids. *ACS Macro Letters*, 9(7):924–928, 2020.

[192] Vijay Mhetar and L. A. Archer. Slip in Entangled Polymer Melts. 1. General Features. *Macromolecules*, 31(24):8607–8616, December 1998.

[193] Savvas G. Hatzikiriakos. Slip mechanisms in complex fluid flows. *Soft Matter*, 11(40):7851–7856, 2015.

[194] Savvas G. Hatzikiriakos. Wall slip of molten polymers. *Progress in Polymer Science*, 37(4):624 – 643, 2012. Topical Issue on Polymer Physics.

[195] Michael D. Graham. Fluid Dynamics of Dissolved Polymer Molecules in Confined Geometries. *Annu. Rev. Fluid Mech.*, 43(1):273–298, January 2011.

[196] G. Chauveteau. Fundamental Criteria in Polymer Flow Through Porous Media. In J. E. Glass, editor, *Water-Soluble Polymers: Beauty with Performance*, volume 213 of *Advances in Chemistry*. American Chemical Society, Washington, DC, May 1986.

[197] Howard A. Barnes. A review of the slip (wall depletion) of polymer solutions, emulsions and particle suspensions in viscometers: its cause, character, and cure. *Journal of Non-Newtonian Fluid Mechanics*, 56(3):221–251, March 1995.

[198] H. Bessaies-Bey, J. Fusier, S. Harrisson, M. Destarac, S. Jouenne, N. Passade-Boupat, F. Lequeux, J.-B. d'Espinose de Lacaillerie, and N. Sanson. Impact of polyacrylamide adsorption on flow through porous siliceous materials: State of the art, discussion and industrial concern. *Journal of Colloid and Interface Science*, 531:693–704, December 2018.

[199] G. J. Fleer, L. K. Koopal, and J. Lyklema. Polymer adsorption and its effect on the stability of hydrophobic colloids: I. Characterization of polyvinyl alcohol adsorption on silver iodide. *Kolloid-Z.u.Z.Polymere*, 250(7):689–702, July 1972.

[200] J. F. Joanny, L. Leibler, and P. G. De Gennes. Effects of polymer solutions on colloid stability. *Journal of Polymer Science: Polymer Physics Edition*, 17(6):1073–1084, 1979. _eprint: https://onlinelibrary.wiley.com/doi/pdf/10.1002/pol.1979.180170615.

[201] Seong Jun Park, Anisha Shakya, and John T. King. Depletion layer dynamics of polyelectrolyte solutions under Poiseuille flow. *Proc Natl Acad Sci USA*, 116(33):16256–16261, August 2019.

[202] Philip Pincus. Colloid stabilization with grafted polyelectrolytes. *Macromolecules*, 24(10):2912–2919, 1991.

[203] Harry J. Ploehn, William B. Russel, and Carol K. Hall. Self-consistent field model of polymer adsorption: generalized formulation and ground-state solution. *Macromolecules*, 21(4):1075–1085, July 1988.

[204] M Santore. Dynamics in adsorbed homopolymer layers: Understanding complexity from simple starting points. *Current Opinion in Colloid & Interface Science*, 10(3-4):176–183, October 2005.

[205] L. T. Lee, O. Guiselin, A. Lapp, B. Farnoux, and J. Penfold. Direct measurements of polymer depletion layers by neutron reflectivity. *Phys. Rev. Lett.*, 67:2838–2841, Nov 1991.

[206] PC Chatwin. The initial development of longitudinal dispersion in straight tubes. *Journal of Fluid Mechanics*, 80(1):33–48, 1977.

[207] NG Barton. On the method of moments for solute dispersion. *Journal of Fluid Mechanics*, 126:205–218, 1983.

[208] Søren Vedel and Henrik Bruus. Transient taylor–aris dispersion for time-dependent flows in straight channels. *Journal of fluid mechanics*, 691:95–122, 2012.

[209] Søren Vedel, Emil Hovad, and Henrik Bruus. Time-dependent taylor–aris dispersion of an initial point concentration. *Journal of fluid mechanics*, 752:107–122, 2014.

[210] Hiroshi Orihara and Yoshinori Takikawa. Brownian motion in shear flow: Direct observation of anomalous diffusion. *Physical Review E*, 84(6):061120, 2011.

[211] Einar Orn Fridjonsson, Joseph D. Seymour, and Sarah L. Codd. Anomalous preasymptotic colloid transport by hydrodynamic dispersion in microfluidic capillary flow. *Physical Review E*, 90(1):010301(R), 2014.

[212] Yoshinori Takikawa, Takahiro Nunokawa, Yuji Sasaki, Makoto Iwata, and Hiroshi Orihara. Three-dimensional observation of brownian particles under steady shear flow by stereo microscopy. *Physical Review E*, 100(2):022102, 2019.

[213] LO Pedro et al. Diffusion coefficients of aqueous phenols determined by the taylor dispersion technique. evidence for solute adsorption on the walls of teflon tubing. *Journal of the Chemical Society, Faraday Transactions*, 89(1):113–118, 1993.

[214] Michael S. Bello, Roberta Rezzonico, and Pier Giorgio Righetti. Use of taylor-aris dispersion for measurement of a solute diffusion coefficient in thin capillaries. *Science*, 266(5186):773–776, 1994.

[215] Hervé Cottet, Jean-Philippe Biron, Luca Cipelletti, Rachid Matmour, and Michel Martin. Determination of individual diffusion coefficients in evolving binary mixtures by taylor dispersion analysis: application to the monitoring of polymer reaction. *Analytical chemistry*, 82(5):1793–1802, 2010.

[216] Andrea Hawe, Wendy L Hulse, Wim Jiskoot, and Robert T Forbes. Taylor dispersion analysis compared to dynamic light scattering for the size analysis of therapeutic peptides and proteins and their aggregates. *Pharmaceutical research*, 28(9):2302–2310, 2011.

[217] Meagan R Moser and Christopher A Baker. Taylor dispersion analysis in fused silica capillaries: a tutorial review. *Analytical Methods*, 13(21):2357–2373, 2021.

[218] G Madras, BL Hamilton, and Michael A Matthews. Influence of adsorption on the measurement of diffusion coefficients by taylor dispersion. *International journal of thermophysics*, 17(2):373–389, 1996.

[219] Rudro R Biswas and Pabitra N Sen. Taylor dispersion with absorbing boundaries: A stochastic approach. *Physical Review Letters*, 98(16):164501, 2007.

[220] Sophie Marbach, David S Dean, and Lydéric Bocquet. Transport and dispersion across wiggling nanopores. *Nature Physics*, 14(11):1108–1113, 2018.

[221] Sophie Marbach and Karen Alim. Active control of dispersion within a channel with flow and pulsating walls. *Physical Review Fluids*, 4(11):114202, 2019.

[222] Arthur Alexandre, Thomas Guérin, and David S Dean. Generalized taylor dispersion for translationally invariant microfluidic systems. *Physics of Fluids*, 33(8):082004, 2021.

[223] A. Alexandre, M. Mangeat, T. Guérin, and D. S. Dean. How stickiness can speed up diffusion in confined systems. *Phys. Rev. Lett.*, 128:210601, May 2022.

[224] Manuchehr Aminian, Francesca Bernardi, Roberto Camassa, Daniel M. Harris, and Richard M. McLaughlin. How boundaries shape chemical delivery in microfluidics. *Science*, 354(6317):1252–1256, 2016.

[225] Amandine Cuenca and Hugues Bodiguel. Fluorescence photobleaching to evaluate flow velocity and hydrodynamic dispersion in nanoslits. *Lab Chip*, 12:1672–1679, 2012.

[226] Howard Brenner and Lawrence J Gaydos. The constrained brownian movement of spherical particles in cylindrical pores of comparable radius: Models of the diffusive and convective transport of solute molecules in membranes and porous media. *Journal of Colloid and Interface Science*, 58(2):312–356, 1977.

[227] J. Camacho. Purely global model for taylor dispersion. *Physical Review E*, 48(1):310, 1993.

[228] Paul B Bailey, William N Everitt, and Anton Zettl. The sleign2 sturm-liouville code. *ACM Trans. Math. Software*, 27(2):143–192, 2001.

[229] Léa Chazot-Franguiadakis, Joelle Eid, Marius Socol, Bastien Molcrette, Philippe Guégan, Marylène Mougel, Anna Salvetti, and Fabien Montel. Optical quantification by nanopores of viruses, extracellular vesicles, and nanoparticles. *Nano Letters*, 22(9):3651–3658, 2022. PMID: 35475610.

[230] Sabrina Jahn, Jasmine Seror, and Jacob Klein. Lubrication of articular cartilage. *Annual review of biomedical engineering*, 18:235–258, 2016.

[231] Ivan Cher. A new look at lubrication of the ocular surface: fluid mechanics behind the blinking eyelids. *The ocular surface*, 6(2):79–86, 2008.

[232] M.B. Jones, G.R. Fulford, C.P. Please, D.L.S. McElwain, and M. J. Collins. Elastohydrodynamics of the eyelid wiper. *Bulletin of Mathematical Biology*, 70:323–343, 2008.

[233] Heather S Davies, Delphine Débarre, Nouha El Amri, Claude Verdier, Ralf P Richter, and Lionel Bureau. Elastohydrodynamic lift at a soft wall. *Physical review letters*, 120(19):198001, 2018.

[234] Matthias Heil and Andrew L Hazel. Fluid-structure interaction in internal physiological flows. *Annual review of fluid mechanics*, 43:141–162, 2011.

[235] Matthew Hirschhorn, Vakhtang Tchantchaleishvili, Randy Stevens, Joseph Rossano, and Amy Throckmorton. Fluid–structure interaction modeling in cardiovascular medicine–a systematic review 2017–2019. *Medical engineering & physics*, 78:1–13, 2020.

[236] Thomas Gervais, Jamil El-Ali, Axel Günther, and Klavs F Jensen. Flow-induced deformation of shallow microfluidic channels. *Lab on a Chip*, 6(4):500–507, 2006.

[237] Dhananjay Dendukuri, Shelley S. Gu, Daniel C. Pregibon, T. Alan Hatton, and Patrick S. Doyle. Stop-flow lithography in a microfluidic device. *Lab Chip*, 7:818–828, 2007.

[238] Ivan C Christov, Vincent Cognet, Tanmay C Shidhore, and Howard A Stone. Flow rate–pressure drop relation for deformable shallow microfluidic channels. *Journal of Fluid Mechanics*, 841:267–286, 2018.

[239] Ivan C Christov. Soft hydraulics: from newtonian to complex fluid flows through compliant conduits. *Journal of Physics: Condensed Matter*, 34:063001, 2021.

[240] Xiaojia Wang and Ivan C. Christov. Theory of the flow-induced deformation of shallow compliant microchannels with thick walls. *Proceedings of the Royal Society A: Mathematical, Physical and Engineering Sciences*, 475(2231):20190513, 2019.

[241] E Virot, V Spandan, L Niu, Willem Marinus Van Rees, and L Mahadevan. Elastohydrodynamic scaling law for heart rates. *Physical Review Letters*, 125(5):058102, 2020.

[242] Dongeun Huh, Benjamin D Matthews, Akiko Mammoto, Martín Montoya-Zavala, Hong Yuan Hsin, and Donald E Ingber. Reconstituting organ-level lung functions on a chip. *Science*, 328(5986):1662–1668, 2010.

[243] Philip N Duncan, Transon V Nguyen, and Elliot E Hui. Pneumatic oscillator circuits for timing and control of integrated microfluidics. *Proceedings of the National Academy of Sciences*, 110(45):18104–18109, 2013.

[244] Douglas P Holmes, Behrouz Tavakol, Guillaume Froehlicher, and Howard A Stone. Control and manipulation of microfluidic flow via elastic deformations. *Soft Matter*, 9(29):7049–7053, 2013.

[245] Johan U Lind, Travis A Busbee, Alexander D Valentine, Francesco S Pasqualini, Hongyan Yuan, Moran Yadid, Sung-Jin Park, Arda Kotikian, Alexander P Nesmith, Patrick H Campbell, et al. Instrumented cardiac microphysiological devices via multimaterial three-dimensional printing. *Nature materials*, 16(3):303–308, 2017.

[246] Felix J Meigel, Peter Cha, Michael P Brenner, and Karen Alim. Robust increase in supply by vessel dilation in globally coupled microvasculature. *Physical Review Letters*, 123(22):228103, 2019.

[247] Samuel Leroy and Elisabeth Charlaix. Hydrodynamic interactions for the measurement of thin film elastic properties. *Journal of Fluid Mechanics*, 674:389–407, 2011.

[248] Samuel Leroy, Audrey Steinberger, Cécile Cottin-Bizonne, Frédéric Restagno, Liliane Léger, and Elisabeth Charlaix. Hydrodynamic interaction between a spherical particle and an elastic surface: a gentle probe for soft thin films. *Physical review letters*, 108(26):264501, 2012.

[249] Yumo Wang, Charles Dhong, and Joelle Frechette. Out-of-contact elastohydrodynamic deformation due to lubrication forces. *Physical review letters*, 115(24):248302, 2015.

[250] Yumo Wang, Georgia A Pilkington, Charles Dhong, and Joelle Frechette. Elastic deformation during dynamic force measurements in viscous fluids. *Current opinion in colloid & interface science*, 27:43–49, 2017.

[251] Yumo Wang, Matthew R Tan, and Joelle Frechette. Elastic deformation of soft coatings due to lubrication forces. *Soft Matter*, 13(38):6718–6729, 2017.

[252] Yumo Wang and Joelle Frechette. Morphology of soft and rough contact via fluid drainage. *Soft Matter*, 14(37):7605–7614, 2018.

[253] Aurélie Hourlier-Fargette, Arnaud Antkowiak, Antoine Chateauminois, and Sébastien Neukirch. Role of uncrosslinked chains in droplets dynamics on silicone elastomers. *Soft Matter*, 13(19):3484–3491, May 2017. Publisher: The Royal Society of Chemistry.

[254] Robert W. Style, Yonglu Che, Su Ji Park, Byung Mook Weon, Jung Ho Je, Callen Hyland, Guy K. German, Michael P. Power, Larry A. Wilen, John S. Wettlaufer, and Eric R. Dufresne. Patterning droplets with durotaxis. *Proceedings of the National Academy of Sciences*, 110(31):12541–12544, July 2013.

[255] Menghua Zhao, Julien Dervaux, Tetsuharu Narita, François Lequeux, Laurent Limat, and Matthieu Roché. Geometrical control of dissipation during the spreading of liquids on soft solids. *Proceedings of the National Academy of Sciences*, 115(8):1748–1753, February 2018. Publisher: Proceedings of the National Academy of Sciences.

[256] Robert W. Style, Rostislav Boltyanskiy, Yonglu Che, J. S. Wettlaufer, Larry A. Wilen, and Eric R. Dufresne. Universal Deformation of Soft Substrates Near a Contact Line and the Direct Measurement of Solid Surface Stresses. *Physical Review Letters*, 110(6):066103, February 2013.

[257] Menghua Zhao, François Lequeux, Tetsuharu Narita, Matthieu Roché, Laurent Limat, and Julien Dervaux. Growth and relaxation of a ridge on a soft poroelastic substrate. *Soft Matter*, 14(1):61–72, 2018.

[258] Mengxing Li, Bruno Bresson, F Cousin, Christian Fretigny, and Yvette Tran. Submicrometric films of surface-attached polymer network with temperature-responsive properties. *Langmuir*, 31(42):11516–11524, 2015.

[259] Athanasia I. Panou, Kyriaki G. Papadokostaki, Petroula A. Tarantili, and Merope Sanopoulou. Effect of hydrophilic inclusions on PDMS crosslinking reaction and its interrelation with mechanical and water sorption properties of cured films. *European Polymer Journal*, 49:1803–1810, 2013.

[260] *NIST Digital Library of Mathematical Functions*. http://dlmf.nist.gov/, Release 1.1.5 of 2022-03-15. F. W. J. Olver, A. B. Olde Daalhuis, D. W. Lozier, B. I. Schneider, R. F. Boisvert, C. W. Clark, B. R. Miller, B. V. Saunders, H. S. Cohl, and M. A. McClain, eds.

[261] Lydéric Bocquet and Eric Lauga. A smooth future? *Nature Materials*, 10(5):334–337, May 2011.

[262] Dennis C. Prieve and Stacy G. Bike. Electrokinetic Repulsion Between Two Charged Bodies Undergoing Sliding Motion. *Chemical Engineering Communications*, 55(1-6):149–164, May 1987.

[263] X. Wu, P. Warszynski, and T.G.M. van de Ven. Electrokinetic Lift: Observations and Comparisons with Theories. *Journal of Colloid and Interface Science*, 180(1):61–69, June 1996.

[264] Marcela Rodríguez Matus, Zaicheng Zhang, Zouhir Benrahla, Arghya Majee, Abdelhamid Maali, and Alois Würger. Electroviscous drag on squeezing motion in sphere-plane geometry. *Physical Review E*, 105(6):064606, June 2022. Publisher: American Physical Society.

[265] Amandine Cuenca and Hugues Bodiguel. Submicron Flow of Polymer Solutions: Slippage Reduction due to Confinement. *Physical Review Letters*, 110(10):108304, March 2013.

[266] Charles J. Marzzacco. The Enthalpy of Decomposition of Hydrogen Peroxide. *Journal of Chemical Education*, 76:1517, 1999.

[267] Clement Riedel, Ronen Gabizon, Christian A. M. Wilson, Kambiz Hamadani, Konstantinos Tsekouras, Susan Marqusee, Steve Pressé, and Carlos Bustamante. The heat released during catalytic turnover enhances the diffusion of an enzyme. *Nature*, 517(7533):227–230, January 2015.

[268] Jaime Agudo-Canalejo, Pierre Illien, and Ramin Golestanian. Phoresis and Enhanced Diffusion Compete in Enzyme Chemotaxis. *Nano Letters*, 18(4):2711–2717, April 2018. Publisher: American Chemical Society.

[269] Ah-Young Jee, Kuo Chen, Tsvi Tlusty, Jiang Zhao, and Steve Granick. Enhanced Diffusion and Oligomeric Enzyme Dissociation. *Journal of the American Chemical Society*, 141(51):20062–20068, December 2019.

[270] Zhijie Chen, Alan Shaw, Hugh Wilson, Maxime Woringer, Xavier Darzacq, Susan Marqusee, Quan Wang, and Carlos Bustamante. Single-molecule diffusometry reveals no catalysis-induced diffusion enhancement of alkaline phosphatase as proposed by FCS experiments. *Proceedings of the National Academy of Sciences*, 117(35):21328–21335, September 2020.

[271] Huan Wang, Myeonggon Park, Ruoyu Dong, Junyoung Kim, Yoon-Kyoung Cho, Tsvi Tlusty, and Steve Granick. Boosted molecular mobility during common chemical reactions. *Science*, 369(6503):537–541, July 2020.

[272] Lucy L. Fillbrook, Jan-Philipp Günther, Günter Majer, Daniel J. O'Leary, William S. Price, Hal Van Ryswyk, Peer Fischer, and Jonathon E. Beves. Following Molecular Mobility during Chemical Reactions: No Evidence for Active Propulsion. *Journal of the American Chemical Society*, 143(49):20884–20890, December 2021.

[273] Nasrollah Rezaei-Ghaleh, Jaime Agudo-Canalejo, Christian Griesinger, and Ramin Golestanian. Molecular Diffusivity of Click Reaction Components: The Diffusion Enhancement Question. *Journal of the American Chemical Society*, 144(3):1380–1388, January 2022.

[274] Ramin Golestanian. Enhanced Diffusion of Enzymes that Catalyze Exothermic Reactions. *Physical Review Letters*, 115(10):108102, September 2015.

[275] Thomas Guérin, Maxim Dolgushev, Olivier Bénichou, and Raphaël Voituriez. Universal kinetics of imperfect reactions in confinement. *Communications Chemistry*, 4(1):1–7, November 2021. Number: 1 Publisher: Nature Publishing Group.

[276] Lyndon Emsley. Editorial Summary of the Comment and Responses on "Following Molecular Mobility during Chemical Reactions: No Evidence for Active Propulsion" and "Molecular Diffusivity of Click Reaction Components: The Diffusion Enhancement Question". *Journal of the American Chemical Society*, 144(30):13429–13430, August 2022. Publisher: American Chemical Society.

[277] Maxime Lavaud. *Confined brownian motion.* PhD thesis, Université de Bordeaux, 2021.

[278] F. Bretherton. The motion of long bubbles in tubes. *Journal of Fluid Mechanics*, 10:166, 1961.

[279] S.R. Hodges, O.E. Jenson, and J.M. Rallison. The motion of a viscous drop through a cylindrical tube. *Journal of Fluid Mechanics*, 501:279, 2004.

[280] I. Cantat. Liquid meniscus friction on a wet plate : Bubbles , lamellae , and foams. *Physics of Fluids*, 25:031303, 2014.

[281] A. Huerre, O. Theodoly, A.M. M. Leshansky, M.-P. Valignat, I. Cantat, and M.-C. Jullien. Droplets in microchannels: Dynamical properties of the lubrication film. *Physical Review Letters*, 115:064501, 2015.

[282] Helene Berthet, Olivia Du Roure, and Anke Lindner. Microfluidic Fabrication Solutions for Tailor-Designed Fiber Suspensions. *Applied Sciences*, 6(12):385, November 2016.

[283] Jean Cappello, Mathias Bechert, Camille Duprat, Olivia du Roure, François Gallaire, and Anke Lindner. Transport of flexible fibers in confined microchannels. *Physical Review Fluids*, 4(3):034202, March 2019.

[284] Camille Duprat, Hélène Berthet, Jason S. Wexler, Olivia du Roure, and Anke Lindner. Microfluidic in situ mechanical testing of photopolymerized gels. *Lab on a Chip*, 15(1):244–252, 2015.

[285] Loïc d'Eramo, Benjamin Chollet, Marie Leman, Ekkachai Martwong, Mengxing Li, Hubert Geisler, Jules Dupire, Margaux Kerdraon, Clémence Vergne, Fabrice Monti, et al. Microfluidic actuators based on temperature-responsive hydrogels. *Microsystems & Nanoengineering*, 4(1):1–7, 2018.

[286] Jean Cappello, Vincent d'Herbemont, Anke Lindner, and Olivia du Roure. Microfluidic In-Situ Measurement of Poisson's Ratio of Hydrogels. *Micromachines*, 11(3):318, March 2020.

[287] J. Delavoipière, Y. Tran, E. Verneuil, and A. Chateauminois. Poroelastic indentation of mechanically confined hydrogel layers. *Soft Matter*, 12(38):8049–8058, 2016.

[288] Hilton B de Aguiar, Joshua D McGraw, and Stephen H Donaldson Jr. Interface-sensitive raman microspectroscopy of water via confinement with a multimodal miniature surface forces apparatus. *Langmuir*, 35(48):15543–15551, 2019.

[289] Kai Kristiansen, Stephen H Donaldson Jr, Zachariah J Berkson, Jeffrey Scott, Rongxin Su, Xavier Banquy, Dong Woog Lee, Hilton B De Aguiar, Joshua D McGraw, George D Degen, et al. Multimodal miniature surface forces apparatus (μsfa) for interfacial science measurements. *Langmuir*, 35(48):15500–15514, 2019.

[290] Margaux Kerdraon, Joshua D. Mcgraw, Benjamin Dollet, and Marie-Caroline Jullien. Self-similar relaxation of confined microfluidic droplets. *Physical review letters*, 123(2):024501, 2019.

[291] Elsa Batista, Maria do Céu Ferreira, Andreia Furtado, and João Alves e Sousa. New empir project – metrology for drug delivery, the role of ipq. In *2019 IEEE International Symposium on Medical Measurements and Applications (MeMeA)*, pages 1–5, 2019.

[292] AW Boudaoud, JD McGraw, T Lopez-Leon, and F Ogheard. Traceability of the primary nano-flow measurement system: Measuring the local inner diameter of a glass capillary. *Measurement*, page 113141, 2023.

[293] Sabrina Haefner, Michael Benzaquen, Oliver Bäumchen, Thomas Salez, Robert Peters, Joshua D McGraw, Karin Jacobs, Elie Raphaël, and Kari Dalnoki-Veress. Influence of slip on the plateau–rayleigh instability on a fibre. *Nature communications*, 6(1):7409, 2015.

[294] Paul D Fowler, Céline Ruscher, Joshua D McGraw, James A Forrest, and Kari Dalnoki-Veress. Controlling marangoni-induced instabilities in spin-cast polymer films: How to prepare uniform films. *The European Physical Journal E*, 39:1–8, 2016.

[295] S Mostafa Sabzevari, Joshua D McGraw, and Paula Wood-Adams. Short chains enhance slip of highly entangled polystyrenes during thin film dewetting. *RSC advances*, 6(94):91163–91170, 2016.

[296] Matthias Lessel, Joshua D McGraw, Oliver Bäumchen, and Karin Jacobs. Nucleated dewetting in supported ultra-thin liquid films with hydrodynamic slip. *Soft Matter*, 13(27):4756–4760, 2017.

[297] Joshua D McGraw, Antoine Niguès, Alexis Chennevière, and Alessandro Siria. Contact dependence and velocity crossover in friction between microscopic solid/solid contacts. *Nano letters*, 17(10):6335–6339, 2017.

[298] Mohamed Souheib Chebil, Joshua D Mcgraw, Thomas Salez, Cyrille Sollogoub, and Guillaume Miquelard-Garnier. Influence of outer-layer finite-size effects on the dewetting dynamics of a thin polymer film embedded in an immiscible matrix. *Soft matter*, 14(30):6256–6263, 2018.

RÉSUMÉ

La matière molle est omniprésente dans la nature et dans la vie quotidienne, et elle est couramment amenée à s'écouler dans des espaces confinés. Dans ce contexte, ce manuscrit traite du transport et de l'écoulement de polymères et de particules colloïdales au voisinage de bords et d'interfaces. Dans une première partie, nous décrivons l'écoulement à surface libre de films minces de polymères. La tension superficielle est la force motrice dominante des écoulements, cette dernière étant notamment médiée par les phénomènes interfaciaux et la viscosité. L'adsorption des chaînes de polymères, l'organisation des chaînes près de la surface et les modifications du substrat à l'échelle de la taille du monomère ont un impact majeur sur la condition limite hydrodynamique de glissement. Inversement, cette dernière condition joue un rôle prédominant dans la morphologie de la surface libre pendant l'écoulement. Il est en effet démontré que la morphologie de la surface permet d'établir si les écoulements se passent uniquement à la surface libre, en dessous de la transition vitreuse, où si les écoulements pénètre la profondeur du film complet, au dessus de la susdite transition. Ensuite, en suivant des particules colloïdales évoluant à moins d'un micron d'une interface solide-liquide, nous étudions le glissement des solutions de polymères semi-diluées par microscopie à ondes évanescentes. Cette technique permet également d'étudier le transport de particules près de la surface. Nous étudions en particulier la dispersion de Taylor, c'est-à-dire l'augmentation de l'étalement des particules —par rapport au mouvement brownien pur— grace au couplage entre advection et diffusion. Cet effet est étudié dans les régimes à temps court et près des parois. Nous montrons tout d'abord que les lois d'étalement initiales dépendent fortement de la distribution initiale des particules, avec un croisement entre la dispersion temporelle linéaire et quadratique. Deuxièmement, nous montrons que les appauvrissements induits par l'interface peuvent entraîner une réduction d'un ordre de grandeur des taux d'étalement attendus en milieux confinés. Dans une dernière partie, nous considérons les interactions fluide-structure dans deux contextes de matière molle. Tout d'abord, le problème classique de drainage de Reynolds est étudié théoriquement dans le cas où le solide est poroélastique avec une interface perméable. Nous démontrons un croisement diffusif entre les comportements purement incompressibles et compressibles. Deuxièmement, les écoulements hydrauliques près de parois mous sont traités dans le régime transitoire, en combinant théorie et expérience pour montrer que la relaxation des canaux microfluidiques peut varier de plusieurs ordres de grandeur en raison du gonflement des canaux. Les travaux que nous avons rassemblés mettent en évidence la sensibilité au niveau moléculaire de l'écoulement près de la surface et la manière dont sa faible rigidité peut avoir un impact sur l'hydrodynamique dans le domaine de la micro- et nano-fluidique.

MOTS CLÉS

Glissement de polymères, dispersion de Taylor, elastohydrodynamique

ABSTRACT

Soft condensed matter is ubiquitous in nature and daily life, and is commonly made to flow in confined spaces. In this context, the present manuscript deals with the transport and flow of polymer molecules and colloidal particles near, and making up, a diverse set of boundaries and interfaces. In a first part, we describe the free-interface flow of thin polymer films. Surface tension thus dominates the driving force for flows, this latter in particular mediated by interfacial phenomena and viscosity. Polymer-chain adsorption, near-surface chain organisation, and monomer-scale substrate modifications are shown to produce order-of-magnitude effects in the slip hydrodynamic boundary condition. Conversely, this latter condition is shown to play a dominant role in the free-surface morphology during flow. The surface morphology is indeed shown to permit a diagnosis between free-surface, sub-glass-transition flow, and bulk, full-film liquid flows. Then, tracking colloidal particles in the first micron near a solid-liquid surface, we address the slippage of semi-dilute polymer solutions using evanescent-wave microscopy. Such a technique also permits investigation of near-surface particle transport. We particularly study Taylor dispersion, that is the enhancement —compared to pure Brownian motion— of particle spreading due to advection-diffusion coupling, in pre-asymptotic temporal regimes and near interfaces. We show first that initial spreading laws are highly dependent on the initial distribution of particles, with a crossover between linear and quadratic temporal dispersion. Second, we show that surface-induced depletions may affect an order-of-magnitude reduction in the expected spreading rates in confinement. In a last part, we consider fluid-structure interactions in two soft-matter contexts. First, the classical Reynolds drainage problem is considered theoretically for the case in which the solid is poroelastic and with a permeable interface. We demonstrate a diffusive crossover between purely incompressible and compressible responses. Second, soft-hydraulic flows are treated in the transient regime, combining theory and experiment to show that microfluidic channel relaxation can vary by orders of magnitude as a result of soft-boundary-mediated channel inflation. Our collected works highlight the molecular-level sensitivity of near-surface flow, and how softness can impact hydrodynamics in the micro- and nano-fluidic domain.

KEYWORDS

Polymer slip, Taylor dispersion, elastohydrodynamics